Resonators for hybrid superconductor-atom spin systems

Dissertation
der Mathematisch-Naturwissenschaftlichen Fakultät
der Eberhard Karls Universität Tübingen
zur Erlangung des Grades eines
Doktors der Naturwissenschaften
(Dr. rer. nat.)

vorgelegt von
Benedikt Martin Ferdinand
aus Reutlingen

Tübingen
2018

Gedruckt mit Genehmigung der Mathematisch-Naturwissenschaftlichen Fakultät der Eberhard Karls Universität Tübingen.

Tag der mündlichen Qualifikation:	19.02.2018
Dekan:	Prof. Dr. Wolfgang Rosenstiel
1. Berichterstatter:	Prof. Dr. Reinhold Kleiner
2. Berichterstatter:	Prof. Dr. Dieter Kölle

Kurzfassung

Koplanare Mikrowellen-Resonatoren aus supraleitenden Dünnfilmen stellen einen zentralen Baustein der Quanten-Elektrodynamik mit integrierten Schaltkreisen dar (engl. *circuit quantum electrodynamics*, kurz cQED), in der die fundamentale Wechselwirkung von Mikrowellen-Photonen mit künstlichen Atomen aus supraleitenden Bauelementen untersucht wird. Aufgrund der guten Kontrolle, der selektiven Ansteuerung und der Skalierbarkeit supraleitender Quanten-Bits, kurz Qubits, sind diese stark gekoppelten Systeme, bestehend aus supraleitenden Mikrowellen-Resonatoren und supraleitenden Qubits, aussichtsreiche Kandidaten für die Realisierung einer Quanten-Technologie, die geeignet ist, Quanten-Information unter Benutzung höchst effizienter Algorithmen zu verarbeiten und damit ihre klassischen Gegenstücke zu übertreffen. Aufgrund der geringen Kohärenzzeiten supraleitender Qubits von etwa $100\,\mu$s ist jedoch die Rechenzeit eines solchen Quantencomputers beschränkt. Um diese Einschränkungen zu überwinden, wurde eine Vielzahl hybrider Quantensysteme vorgeschlagen, die die Vorteile verschiedener Quantensysteme vereinen.

Die vorliegende Arbeit beschäftigt sich mit verschiedenen Aspekten zur Realisierung eines hybriden Quanten-Systems bestehend aus integrierten supraleitenden Schaltkreisen und langlebigen ultrakalten ^{87}Rb Atomwolken in den magnetischen Grundzuständen. Einerseits haben diese kalten Atomwolken in der Nähe eines supraleitenden Resonators Kohärenzzeiten auf der Sekundenskala und fungieren folglich im Rahmen der hybriden Architektur als *Quanten-Speicher*. Andererseits ermöglicht die starke Kopplung zwischen supraleitenden Qubits und koplanaren Resonatoren schnelle Rechenprozesse, weshalb supraleitende Qubits als *Quanten-Prozessoren* dienen.

Aufgrund des starren Energie-Spektrums von kalten Grundzustands-Atomen in einer Magnetfalle ist ein in der Resonanzfrequenz durchstimmbarer Resonator von enormem Vorteil hinsichtlich des Erzeugens resonanter Wechselwirkung. Deshalb werden im Rahmen der Arbeit mehrere Konzepte entwickelt und diskutiert, die eine solche Durchstimmbarkeit erlauben.

Dabei wird zunächst auf zwei Konzepte eingegangen, die für Experimente bei einer Temperatur von etwa 4 K geeignet sind. Das erste Konzept nutzt das nicht-lineare Dielektrikum Strontium-Titanat ($SrTiO_3$) als Teil eines induktiv gekoppelten Halbwellen-Resonators mit diskretem nicht-linearen Kondensator aus. Im Rahmen der Arbeit wurde ein theoretisches Modell entwickelt, das die Bestimmung der komplexwertigen dielektrischen Funktion von $SrTiO_3$ erlaubt, wodurch ein gezielter Einsatz des nicht-linearen Dielektrikums in zukünftigen Proben ermöglicht wird. Die Frequenz konnte dabei, abhängig vom Proben-Design, um $10 - 50$ MHz verstimmt werden, während die Güte-Faktoren mit mehreren 1000 stets relativ groß waren. Der zweite Mechanismus zum Durchstimmen der Resonanzfrequenz war das Ausnutzen der stark temperaturabhängigen kinetischen Induktivität des Supraleiters Niob (kritische Temperatur $T_c = 9.2$ K) für Temperaturen $T > 4$ K. Dabei konnte die Resonanzfrequenz um 100 MHz verändert werden. Aufgrund der einfacheren experimentellen Realisierung wurde das zweite Konzept ausgenutzt, um sowohl die resonante, als auch die nicht-resonante Wechselwirkung zwischen ultrakalten ^{87}Rb Grundzustands-Atomen mit dem Strahlungsfeld eines Resonators zu untersuchen.

Für Experimente bei mK-Temperaturen wurde ein *Zwei-Chip* Ansatz verfolgt, der das Stapeln zweier Substrate mit supraleitenden Dünnfilmen vorsieht. Der untere Chip enthält dabei einen koplanaren Wellenleiter für Mikrowellen, während der obere Chip einen Mikrowellen-Resonator aus einem Interdigitalkondensator und einer Induktivitäts-Schleife enthält. Ein theoretisches Modell wurde zusammen mit Simulationen der relevanten Schaltkreis-Parameter verwendet, um das Verhalten eines Resonators beim Verschieben des Resonator-Chips gegenüber dem unteren Wellenleiter-Chip vorherzusagen. Der Vergleich mit experimentellen Ergebnissen ist exzellent und zeigt eine Durchstimmbarkeit von etwa 25 MHz. In Abgrenzung zu anderen Konzepten der Durchstimmbarkeit führt das Verwenden dieses Konzepts **nicht** zu einer Reduktion des Güte-Faktors.

Im letzten Teil der Arbeit wird die Entwicklung eines Probenhalters vorgestellt, der die Realisierung eines hybriden Quantensystems bei mK-

Temperaturen ermöglichen soll. Dieser enthält unter anderem integrierte *Bias-T-Chips*, die aus Supraleitern bestehen und mit deren Hilfe sowohl Mikrowellen, als auch Gleichströme in die Probe eingespeist werden können, ohne eine signifikante Menge an Wärme zu generieren.

Contents

1 Introduction

One hot topic of current research activities is the development of a quantum technology capable of processing, transmitting and in particular storing quantum information [1, 2]. Such quantum computing devices are proposed to outperform their classical counterparts for applications like factorizing large numbers, using the famous Shor algorithm [3], or, following ideas of Feynman [4], to simulate the quantum world more efficiently than classical computers. Moreover, similar concepts allow secure communication using quantum cryptography [3], other technologies enable to advance metrology to the limits of the Heisenberg uncertainty relation [5].

The processing units of such a quantum computing device are quantum binary digits (qubits), which can be understood as quantum mechanical two-level systems. Perhaps the most obvious physical systems for such a qubit are natural atoms like neutral atoms or trapped ions, due to their rich variety of quantum mechanical states related to their numerous internal degrees of freedom. Furthermore, nowadays coherent control over other *atom-like* spin-systems embedded in solids is possible. Amongst a multitude of experimental realizations, nitrogen-vacancy (NV) color centers in diamond are the most prominent representative of such a spin-system [6].

In addition to these qubits which nature in principle forms by itself, there are other solid-state based qubits, namely electron spins in semiconductor quantum dots [7] and superconducting qubits [8]. These qubits, often referred to as artificial atoms, can be engineered and tailored to specific requirements through custom structures using micropatterned thin film circuits. However, in contrast to natural atoms which in particular have optical transitions, these solid state devices operate in the microwave domain. Consequently, such components only show their quantum nature for low thermal energies $k_\mathrm{B}T \ll \hbar\omega_\mathrm{a}$, where k_B and $\hbar$ respectively are Boltzmanns and

Plancks constants, T is the temperature and ω_a is the atomic transition frequency. Thus, these quantum devices are subject of low-temperature physics at temperatures of about 50 mK.

For the realization of a quantum computer, DiVincenzo composed a set of requirements which have to be fulfilled simultaneously [9]. The most crucial aspect regarding these criteria (and the present thesis) may seem somewhat paradoxical at first: While under the programmer's control using measurements, the quantum computer has to act as a *closed box*, meaning that the decoherence in the quantum system has to be much slower than the time required for universal quantum gate operations [1]. However, groundbreaking experiments have demonstrated that quantum states can be measured non-destructively [10, 11], awarded with the noble prize in physics in 2012. In particular, single atoms were used to count the number of photons in a superconducting three-dimensional microwave cavity.

Since then, similar coupled systems have also been realized for architectures which are based on purely superconducting coplanar devices, and both strong coupling [12] and ultra-strong coupling [13] between the subsystems has been demonstrated. The concept named circuit quantum electrodynamics (cQED) [14] provides several superconducting qubits coupled to one main building block of the architecture, namely a superconducting coplanar waveguide (CPW) resonator. Quantum information is exchanged between distant individual qubits via these resonators acting as a *quantum bus*. The number of qubits coupled to a resonator has subsequently increased, enabling the demonstration of two-qubit gates [15] and even more complex algorithms [16]. However, despite the realization of error correction in such strongly coupled systems [17, 18], these purely superconducting quantum circuits still suffer from short coherence times. In particular, non of the above mentioned realizations of qubits fulfills all DiVincenzo criteria.

As possible solutions hybrid quantum systems which combine the advantages of different quantum systems have been proposed to overcome these limitations [19–22]. Experimental realizations of hybrid quantum systems have been reported for ensembles of electron spins in diamond [23–27], erbium [28] or phosphorus donors [29].

This thesis deals with the experimental realization of a hybrid quantum system consisting of a cloud of ultracold ^{87}Rb atoms coupled to an engineered micropatterned superconducting film circuitry containing coplanar microwave resonators [19, 21, 30, 31]. On the one hand, these natural atoms are known to exhibit long coherence times on the order of several

seconds [32]. On the other hand, due to the strong coupling between superconducting qubits and coplanar resonators, the superconducting microwave circuitry enables fast processing of quantum information. Accordingly, the hybrid system aims to use superconducting qubits as *quantum processors* and the cold atom cloud as a *quantum memory*. The ultimate goal of such a hybrid quantum system is the generation of entanglement between a superconducting qubit and the internal states of the cold atom cloud and the application of novel quantum gates [33–36]. Quantum information is exchanged between the fast-processing superconducting qubits and the long-living internal quantum states of the atoms using a superconducting coplanar resonator.

The coupled system is furthermore proposed to realize an on-chip micromaser [37]. Moreover, due to the rich spectrum of transitions of cold atoms in both the microwave and the optical domain, the hybrid device can serve as a microwave-to-optical transducer, enabling to connect distant quantum computers via flying qubits realized as entangled photons.

In Tübingen, numerous experiments have been carried out in order to set the foundations for building such a hybrid quantum system. First experiments were performed at a temperature of about 4 K, demonstrating that the impact of the Meissner effect on the magnetic trap for atoms close to a superconducting microstructure can be understood theoretically [38] and also be realized in a 4 K-system [39]. Moreover, flux quantization above a closed superconducting ring was studied using a Bose-Einstein condensate [40], serving as a prove-of-principle experiment for the realization of a quantum random access memory [41–43]. Furthermore, long coherence times on the order of several seconds were observed experimentally close to an off-resonant superconducting coplanar waveguide microwave resonator [44]. Lately, as one part of this thesis (concerning the superconducting resonator), the resonant and off-resonant coupling of a resonator in the classical regime ($k_\mathrm{B}T \gg \hbar\omega_\mathrm{a}$) was investigated [45]. In order to achieve a transformation of know-how to a real quantum system operating at mK-temperatures, in addition to the 4 K-setup a mK-setup was built up in several works [46, 47].

The above experiments were carried out in the framework of a close collaboration with the Nano Atomoptics group of Prof. Dr. József Fortágh. Our group, and in particular the work of this thesis, targets to design, fabricate and characterize superconducting coplanar devices optimized for the application in hybrid quantum systems. The cold atom clouds are trapped close to a resonator structure using a magnetic microtrap [48], composed of

the magnetic field generated by a current carrying wire and a homogeneous magnetic bias field. For the out-of-plane component of a homogeneous magnetic field on the mT-range, Abrikosov vortices can enter the superconducting structures and affect the performance of the coplanar device. Such effects were considered and analyzed in a previous work [49], aiming to analyze the vortex related loss mechanisms [50] and develop concepts to reduce such losses [51, 52]. In particular it was found that coupling the resonators inductively instead of capacitively reduces vortex induced losses by one order of magnitude [52] and enables to create a persistent current trap [53].

However, despite the reduction of vortex induced losses and related shifts of the resonance frequency, it is inevitable to have a frequency tunable resonator. This is due to the energy spectrum, which in particular for ^{87}Rb ground state atoms in a magnetic trap is fixed. Furthermore, fabricating the same resonator various times leads to a variance of the resonance frequency of up to 20 MHz. Thus, in order to fine-tune the resonance frequency to the atomic transition frequency, which is $\omega_a \approx 2\pi \cdot 6.834\,\mathrm{GHz}$ for ^{87}Rb ground state atoms, such a tunable resonator necessarily must have a tunability of about $10 - 50\,\mathrm{MHz}$.

This thesis is based on the previous works mentioned above. Along the path towards the goal of building a hybrid quantum system consisting of superconducting microstructures and cold atoms, however, further challenges have to be tackled. Some of those aspects are discussed in the following, mainly focusing on the development and the implication of concepts for tunable resonators:

First, Sec. 2 deals with the basics of transmission line theory, superconductivity and a brief description of nonlinear dielectrics.

In Sec. 3, two concepts are introduced allowing one to change the resonance frequency *in situ* for experiments carried out at $\approx 4\,\mathrm{K}$. First, both the development and experimental realization of a concept of tuning the resonance frequency based on a nonlinear lumped capacitor as a part of a coplanar waveguide transmission line resonator is discussed, allowing one to change the resonance frequency by up to 50 MHz, while still providing relatively large quality factors. Second, using the temperature to induce shifts of the resonance frequency is characterized. These resonators were furthermore used to investigate the coupling to cold atom clouds [45].

As a tuning-concept applicable for experiments taking place at mK-temperatures, a stacked two-chip device consisting of one chip containing a microwave transmission line for excitation and readout, and one further chip

with a lumped element resonator patterned on top was developed and investigated both in theory and experiment. The results are described in Sec. 4, demonstrating that moving the resonator with respect to the transmission line can be used to change the resonance frequency by 25 MHz. Moreover, the trapping of atoms in the microwave magnetic field generated by the lumped element resonator is discussed. The section ends with a theoretical consideration of the extension of such a stacked device in order to couple to Rydberg states instead of magnetic ground states.

In order to enable the realization of a hybrid quantum system in a real experiment at mK-temperatures, a new sample holder was developed. The sample holder contains a *bias-T-chip* which is purely based on superconductors, allowing one to apply both large direct currents and microwave currents to the sample. The sample holder is presented in Sec. 5 with all its components.

Finally, the results of the thesis are summarized in Sec. 6, where also a short outlook of an integrated chip architecture allowing one to realize the envisioned hybrid quantum system is given.

2 | Basics

2.1. Microwave Theory

2.1.1. Properties of resonant LCR circuits

Microwave resonators, such as the ones fabricated during the thesis, can basically be divided into two types of resonators: transmission line (TL) resonators and lumped-element (LE) resonators. Whilst the latter simply are LCR circuits, consisting of an inductor L, a capacitor C and a resistor R, the TL resonators are made of waveguides which are terminated at two sides, thereby defining the boundary conditions for a long-living standing wave. However, close to resonance, also the TL resonators behave as an LCR circuit, as shown later (Sec. 2.1.3). Thus, before going into the details of TLs and the underlying description, the basic properties of resonant LCR circuits are reviewed.

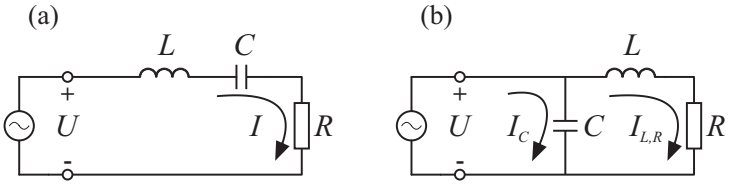

Figure 2.1.: Schematic of a serial LCR resonant circuit (a) and a resonant circuit, where the capacitor C shunts the serial combination of the inductor L and the resistor R, (b). Additionally shown are the current paths I in (a) and I_C and $I_{L,R}$ in (b).

Of particular importance for the resonators presented throughout this thesis are two LCR circuits depicted in Fig. 2.1(a) and (b). The first of these is a serial LCR circuit with an impedance

$$Z_{LCR} = R + i\omega L + \frac{1}{i\omega C} \ , \tag{2.1}$$

where ω is the frequency applied to the circuit. Resonance occurs when the reactive components cancel each other, i.e. when $\Im(Z_{LCR}) = 0$, where $\Im$ denotes the imaginary part of a complex number. Accordingly, the resonance frequency is given by

$$\omega_0 = \frac{1}{\sqrt{LC}} \ . \tag{2.2}$$

Using the above expression, one finds as an approximation of the input impedance around resonance ($\omega = \omega_\mathrm{r} + \Delta\omega$)

$$Z_{LCR} \approx R + 2iL\Delta\omega \ . \tag{2.3}$$

The quality factor Q of such a resonant circuit, which is a measure of the time-scale on which the energy stored in the circuit decays, is defined as [54]

$$Q = \omega \frac{\text{average energy stored}}{\text{energy loss/second}} = \omega \frac{W_\mathrm{e} + W_\mathrm{m}}{P_\mathrm{loss}} \ , \tag{2.4}$$

where

$$W_\mathrm{e} = \frac{1}{4}C|U_C|^2 \overset{(2.1),(2.2)}{=} \frac{1}{4}\frac{|I|^2}{\omega^2 C} \ , \ W_\mathrm{m} = \frac{1}{4}L|I|^2 \ \text{ and } \ P_\mathrm{loss} = \frac{1}{2}R|I|^2 \tag{2.5}$$

are the average electric and magnetic energy stored in the capacitor C and the inductor L, as well as the power dissipated by the resistor R. In general, the quality factor in Eq. (2.4) is defined for arbitrary frequencies ω. In the following, however, only the on-resonance quality factor is considered, and thus, for the sake of brevity, "on-resonance" is omitted. Using Eqs. (2.1) and (2.5), the quality factor Q can be calculated as

$$Q = \frac{\omega_0 L}{R} = \frac{1}{\omega_0 C R} \ . \tag{2.6}$$

The frequency dependence of P_{loss} can be found using $|U_0| = |Z_{LCR}| \cdot |I_0|$ as

$$\begin{aligned} P_{\text{loss}} = \frac{1}{2}R|I_0|^2 = \frac{1}{2}R\frac{|U_0|^2}{R^2 + (\omega L - \frac{1}{\omega C})^2} &\overset{\omega\approx\omega_0}{\approx} \frac{1}{2}R\frac{|U_0|^2}{R^2 + (\Delta\omega)^2\frac{4}{\omega_0^4 C^2}} \\ &\propto \frac{\omega_0^2/Q^2}{\omega_0^2/Q^2 + 4(\Delta\omega)^2} \ , \end{aligned} \tag{2.7}$$

where the last expression, which is normalized to the energy dissipated on resonance, represents a Lorentzian lineshape with the "full width at half max" (FWHM) $\omega_{\text{FWHM}} = \omega_0/Q$. Thus, both the resonance frequency ω_0 and the quality factor Q can be obtained by fitting a Lorentzian to the spectrum of the power dissipated by the resistor R with the quality factor

$$Q = \frac{\omega_0}{\omega_{\text{FWHM}}} \ . \tag{2.8}$$

The other important LCR circuit shown in Fig. 2.1(b) is somewhat unusual, since its components are neither connected completely in series, nor in parallel. However, the serial combination of an inductor L and a resistor R shunted by a capacitor C will later be part of a more complex circuit (see Sec. 4)[1]. Thus, its properties have to be well known. The impedance Z_{LCR} of the LCR circuit shown in Fig. 2.1(b) is given by

$$Z_{LCR} = \left(\frac{1}{i\omega L + R} + i\omega C\right)^{-1} = \frac{i\omega L + R}{1 - \omega^2 LC + i\omega CR} \ . \tag{2.9}$$

Again, equating the imaginary part to zero reveals the resonance frequency as

$$\omega_0^2 = \frac{1}{LC} - \frac{R^2}{L^2} \approx \frac{1}{LC} \quad \rightarrow \quad \omega_0 \approx \frac{1}{\sqrt{LC}} \ . \tag{2.10}$$

The approximation in Eq. (2.10) holds with high fidelity for the resonators investigated in this thesis, since $R^2/L^2 \approx 10^{-7} \cdot 1/LC$ for $R = 10^{-2}$. For this resonant circuit, the average electric and magnetic energy, as well as the loss per oscillation obey

$$\begin{aligned} W_{\text{e}} = \frac{1}{4}C|U_c|^2 = \frac{1}{4}C(\omega^2 L^2 + R^2)|I_{L,R}|^2 \ , \\ W_{\text{m}} = \frac{1}{4}L|I_{L,R}|^2 \ \text{ and } \ P_{\text{loss}} = \frac{1}{2}R|I_{L,R}|^2 \ . \end{aligned} \tag{2.11}$$

[1] The circuit will be used to account for losses of a LE resonator made of Niobium (critical temperature $T_{\text{c}} = 9.2\,\text{K}$) at a temperature of 4.2 K, at which resistive losses in the inductor are dominant.

The quality factor can thus be calculated as

$$Q = \frac{\omega_0 L}{R} \approx \frac{1}{\omega_0 C R} \ . \tag{2.12}$$

Note, that the first equation in this expression applies exactly, and is the same as the first one in Eq. (2.6). Furthermore, also for this resonant circuit, one can obtain a Lorentzian lineshape as the frequency dependence of the power dissipated by the resistor R.

2.1.2. Transmission line theory - wave propagation on a coplanar waveguide

Coplanar waveguide geometry

The devices fabricated during the thesis used coplanar waveguides (CPW) as TL for microwave modes. The geometry of such a CPW is depicted in Fig. 2.2(a). It consists of a center conductor with a width S and two ground planes with a width X and a gap W between neighboring conductors. These conductors with a metalization thickness t are patterned on a substrate with thickness h and complex dielectric function $\varepsilon = \varepsilon_{\mathrm{re}} - i\varepsilon_{\mathrm{im}}$. The electric and magnetic field profiles of a transverse electromagnetic (TEM) mode, propagating in positive z-direction, are demonstrated in Fig. 2.2(b), (c), respectively, in cross-sectional view, making the common use of these waveguides plausible: in the metalization plane the field lines are densely packed in the gaps between center conductor and ground planes, indicating huge field strengths. Thus, both the electric and the magnetic energy are concentrated in close vicinity to these gaps, making these waveguides a useful tool for experiments where strongly localized microwave fields are required.

Distributed-element equivalent circuit

A CPW is usually described by means of TL theory. In contrast to lumped elements, a TL is a distributed-element network, where currents and voltages can vary over its length. Thus, the TL is divided into segments with a length of Δz which are shorter than the wavelength $\lambda \gg \Delta z$ [54]. Accordingly, the voltages across and the currents along these segments can be assumed as constant, enabling a local treatment of the TL in terms of circuit elements. The corresponding circuit is shown in Fig. 2.2(d), which, in analogy to any waveguide, can be seen as a ladder of coupled (LC-) oscillators. For a given

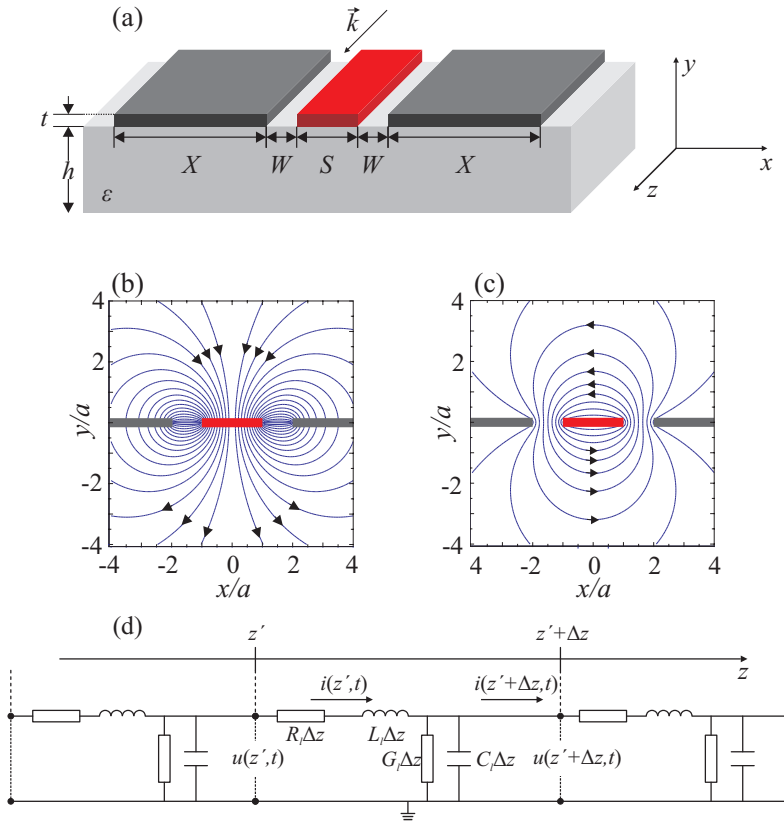

Figure 2.2.: CPW geometry and equivalent circuit. (a) CPW geometry, consisting of a center conductor (red) with a width S and two ground planes (dark grey) with a width X. The gap between neighboring conductors is W. Each conductor has a thickness t and is deposited on the substrate (bright grey) with a thickness h and a dielectric function ε. $\vec{k}$ represents the wavevector of a microwave mode propagating in positive z-direction. (b), (c) electric and magnetic field lines of a TEM wave in the cross-section of the CPW, respectively, where $a = S/2$. (d), circuit model of the CPW.

voltage (current), the stored electric (magnetic) energy of the corresponding field described above is represented by the capacitance C_l (inductance L_l) per unit length, whereas R_l and G_l account for resistive and dielectric losses,

respectively. Solving the Kirchhoff equations and regarding the limit $\Delta z \to 0$ for a time-dependence $u(z',t)$,$i(z',t) \propto e^{i\omega t}$ of the microwave propagating in positive z-direction yields

$$\frac{d^2U(z')}{d^2z'^2} - \gamma^2 U(z') = 0 \quad , \quad \frac{d^2I(z')}{d^2z'^2} - \gamma^2 I(z') = 0\,, \tag{2.13}$$

where $U(z')$ and $I(z')$ are the spatial mode functions of the microwave and $\gamma = \sqrt{(R_l + i\omega L_l)(G_l + i\omega C_l)}$ is the complex valued propagation constant. For a wave propagating in positive z-direction, the solution can be found to obey

$$U(z') = U_0 e^{-\gamma z'} \quad , \quad I(z') = I_0 e^{-\gamma z'}\,, \tag{2.14}$$

with the amplitudes U_0, I_0. For $R_l \ll i\omega L_l$, $G_l \ll i\omega C_l$, the real and imaginary part of $\gamma = \alpha + i\beta$ can therefore be approximately separated as [54]

$$\alpha \approx \frac{1}{2}\left(\frac{R_l}{Z_0} + G_l Z_0\right) \quad , \quad \beta \approx \omega\sqrt{L_l C_l} = \frac{\omega}{v_{\mathrm{ph}}}\,, \tag{2.15}$$

where $Z_0 = \sqrt{L_l/C_l}$ is the characteristic impedance of the TL, and v_{ph} is the phase velocity of the wave.

Transmission line parameters of a CPW

Solving the Laplace equation for the CPW geometry, assuming infinitely wide ground planes $X \to \infty$ and zero metalization thickness $t = 0$, one finds [55–57]

$$C_l = 4\varepsilon_0\varepsilon_{\mathrm{eff}}\frac{\mathrm{K}(k_0)}{\mathrm{K}(k_0')} \quad , \quad L_l = \frac{\mu_0}{4}\frac{\mathrm{K}(k_0')}{\mathrm{K}(k_0)} \quad , \quad Z_0 = \sqrt{\frac{L_l}{C_l}} = \frac{30\pi}{\sqrt{\varepsilon_{\mathrm{eff}}}}\frac{\mathrm{K}(k_0')}{\mathrm{K}(k_0)}\,, \tag{2.16}$$

for the capacitance C_l and inductance L_l per unit length, and the characteristic impedance Z_0 of the TL, with the effective real part of the dielectric constant

$$\varepsilon_{\mathrm{eff}} = 1 + \frac{\varepsilon_{\mathrm{re}} - 1}{2}\frac{\mathrm{K}(k_1)}{\mathrm{K}(k_1')}\frac{\mathrm{K}(k_0')}{\mathrm{K}(k_0)}\,. \tag{2.17}$$

Here, $\mathrm{K}(k)$ is the complete elliptic integral of the first kind, and

$$k_0 = \frac{S}{S + 2W} \quad , \quad k_1 = \frac{\sinh(\frac{\pi S}{4h})}{\sinh(\frac{\pi(S+2W)}{4h})}\,. \tag{2.18}$$

The arguments denoted by "′" obey $k' = \sqrt{1-k^2}$. Closed expressions for finite ground plane widths X and finite metalization thickness t can be found empirically, leading to slight modifications of the expressions given in Eqs. (2.16, [57]).

Terminated transmission lines

For an infinitely long TL, current and voltage are always in-phase, which is reflected in a constant impedance equal to the characteristic impedance Z_0 of the TL. Regarding the true case of a TL with finite length, which is terminated in a load impedance Z_L, the size of Z_L defines the ratio between voltage and current at the load, and therewith the phase between them. More precisely, considering such a terminated TL (see Fig. 2.3(a)) for a superposition of waves propagating in positive and negative z-direction,

$$U(z) = U_0^+ e^{-\gamma z} + U_0^- e^{\gamma z} \quad , \quad I(z) = \frac{U_0^+}{Z_0} e^{-\gamma z} - \frac{U_0^-}{Z_0} e^{\gamma z} \; , \tag{2.19}$$

and demanding

$$Z_L = \frac{U(0)}{I(0)} = Z_0 \frac{U_0^+ + U_0^-}{U_0^+ - U_0^-} \tag{2.20}$$

for the impedance at the load ($z = 0$), one finds

$$\Gamma = \frac{U_0^-}{U_0^+} = \frac{Z_L - Z_0}{Z_L + Z_0} \tag{2.21}$$

for the *voltage reflection coefficient* Γ, which, depending on the size of Z_L, describes the ratio of reflected and incident voltage amplitude. Using Eq. (2.21), the current and voltage on the line can be written as

$$U(z) = U_0^+ (e^{-\gamma z} + \Gamma e^{\gamma z}) \quad , \quad I(z) = \frac{U_0^+}{Z_0} (e^{-\gamma z} - \Gamma e^{\gamma z}) \; . \tag{2.22}$$

Therewith, the input impedance $Z_{\mathrm{in}}(l)$, defined as the impedance seen looking towards the load Z_L at a distance $l = -z$ from the load, can be calculated as [54]

$$Z_{\mathrm{in}}(l) = \frac{U(-l)}{I(-l)} = Z_0 \frac{U_0^+ (e^{\gamma l} + \Gamma e^{-\gamma l})}{U_0^+ (e^{\gamma l} - \Gamma e^{\gamma l})} \overset{(2.21)}{=} Z_0 \frac{Z_L + Z_0 \tanh \gamma l}{Z_0 + Z_L \tanh \gamma l} \; . \tag{2.23}$$

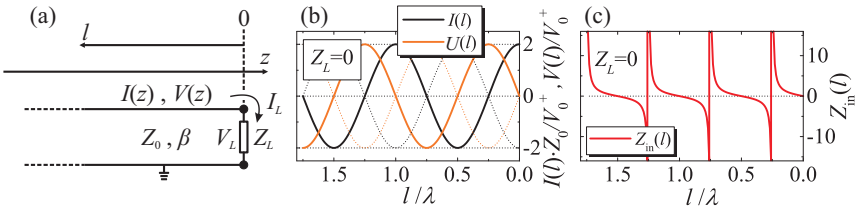

Figure 2.3.: Wave reflection at a load terminating a TL. Panel (a) shows a TL terminated in a load impedance Z_L. For the calculation of the input impedance Z_{in}, the distance from the load is defined as $l = -z$. Panels (b) and (c) depict current $I(l)$ and voltage $U(l)$ (black and orange solid/dotted line) as well as the input impedance $Z_{\text{in}}(l)$ (red) for the special case of a shorted TL with $Z_L = 0$, assuming vanishing TL losses, $\alpha = 0$.

For the special case of an (almost) lossless TL ($\alpha \approx 0$) which is terminated with a short, i.e. $Z_L = 0$, the incident wave is fully reflected, $\Gamma = -1$, and accordingly a standing wave pattern is formed (see Fig. 2.3(b)). Due to the vanishing impedance at the load Z_L, no voltage can drop, leading to a voltage node at $l = 0$. Contrary, current can flow without resistance, and thus one finds an anti-node at the load. Accordingly, along the standing wave current anti-nodes always coincide with voltage nodes and vice versa. Based on the full reflection of the incident wave, both the current and the voltage anti-nodes have twice the amplitude of the incident waves. For this special case, the input impedance Z_{in} of Eq. (2.23) simplifies to

$$Z'_{\text{in}}(l) = Z_0 \tanh \gamma l = Z_0 \frac{\tanh \alpha l + i \tan \beta l}{1 + i \tanh \alpha l \tan \beta l} \ , \tag{2.24}$$

which is plotted in Fig. 2.3(c) (for $\alpha = 0$). The curve clearly demonstrates that by adding a terminating load, e.g. a short, the input impedance can, in contrast to an infinitely long TL, strongly depend on the position l with respect to the load Z_L. One further important issue shown by this curve, is that whenever $l/\lambda = n/2$, for n being an integer, the input impedance is equal to zero ($Z'_{\text{in}} = 0$). This fact incorporates a resonance condition when adding a second short, which is illustrated in the following section.

2.1.3. Inductively coupled half-wavelength CPW resonator

If, at a distance l_{res} to the first short, a second short is added, the aforementioned standing waves can not built up between the two shorts for each

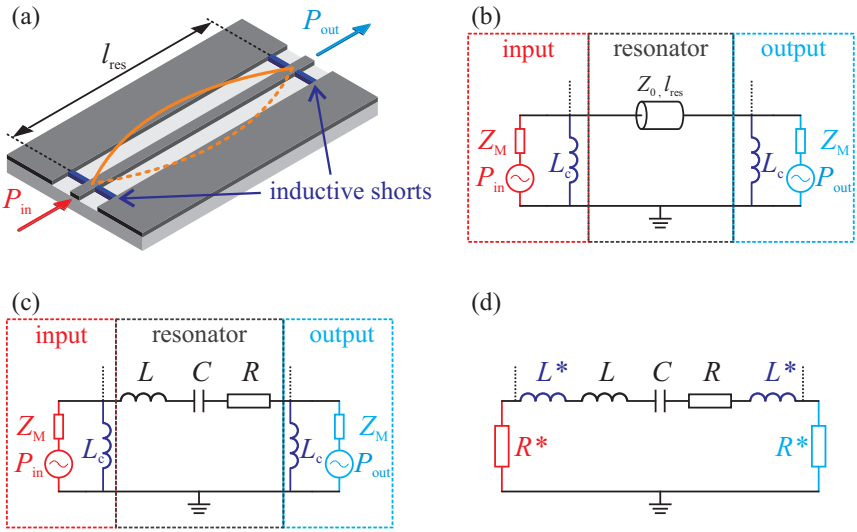

Figure 2.4.: Inductively coupled half-wavelength resonator. (a) Schematic of the CPW resonator, consisting of a CPW with two inductive shorts to ground (purple), which couple the microwave radiation (P_{in}, P_{out}) to the input and output ports. Additionally shown is the resonant voltage (orange) amplitude of the ground mode. (b) TL representation of the coupled resonator, (c) equivalent LCR circuit representation of the resonator, and (d), Thévenin's equivalent of the input-output-circuit, employed for the fully serial lumped element circuit of the TL resonator.

wavelength λ and frequency ω, respectively. Such a device is schematically shown for a CPW in Fig. 2.4(a). The three conductors of the CPW are connected at two sides with inductive shorts, which cause the microwave radiation to be reflected back and forth. Thus, a resonator is formed, in which standing waves can only survive if the multiple reflected waves interfere constructively.

The equivalent TL representation of the half-wavelength resonator is depicted in Fig. 2.4(b). It consists of a TL with a characteristic impedance of Z_0 and two inductive shorts L_c with a separation of l_{res}, defining the length of the resonator. The coupling inductance L_c at each end of the resonator can be calculated as the parallel combination of the two individual shorts to either of the two ground planes. The readout circuit behind both ends of the

resonator, i.e. a network analyzer, is included as a microwave source in series with a load impedance Z_{M}, which, in parallel with the inductive shorts L_{c}, represents the input-output-circuit.

However, first of all, in order to systematically analyze the circuit in detail, both the input-output-circuit and the TL losses are abandoned, and afterwards step by step readopted into the model.

Neglecting the finite value of the inductive shorts L_{c} for the moment, and assuming perfect shorts instead, as well as a lossless TL ($\alpha = 0$), the impedance at these shorts is forced to be zero (cf. Sec. 2.1.2). Referring to the previous section, the input impedance at one short looking towards the other one is given by Eq. (2.24), which for $\alpha = 0$ simplifies to $Z'_{\mathrm{in}} = iZ_0 \tan(\beta l)$. Demanding the disappearance of the input impedance ($Z'_{\mathrm{in}} \overset{!}{=} 0$) at the location of the second short, i.e. $l = l_{\mathrm{res}}$, the resonance condition for long-living standing waves can be obtained as

$$\beta l_{\mathrm{res}} = n\pi \;\equiv\; n\frac{\lambda}{2} = l_{\mathrm{res}} \rightarrow\; \omega_n = \frac{n\pi}{\sqrt{L_l C_l}\, l_{\mathrm{res}}} \;, \tag{2.25}$$

where $\beta = 2\pi/\lambda = \omega\sqrt{L_l C_l}$ is the imaginary part of the complex wave vector $\gamma = \alpha + i\beta$, n is the mode number, $\omega_n = n \cdot \omega_0$ are the resonance frequencies of the device as a multiple of the ground mode resonance frequency ω_0.[2]

Being aware of the resonance condition, Eq. (2.24) can be approximated for frequencies $\omega = \omega_n + \Delta\omega$ close to the resonance frequency ω_n, whilst including a small amount of loss again ($\alpha \neq 0$), yielding [53, 54]

$$Z'_{\mathrm{in}} \approx Z_0(\alpha l_{\mathrm{res}} + i\pi\frac{\Delta\omega}{\omega_0}) \;. \tag{2.26}$$

Note, that for each n the denominator of $\Im(Z'_{\mathrm{in}})$ is ω_0. This is because around resonance, the dependence on n cancels in the resonance condition Eq. (2.25) due to $\beta \propto \omega_n \propto n$. Eq. (2.26) is of the form $R + 2iL\Delta\omega$ (cf. Eq. (2.3)), which is the input impedance of a serial LCR circuit close to its resonance ($\omega_{LCR} = 1/\sqrt{LC_n}$). Thus, substituting

$$R = Z_0 \alpha l_{\mathrm{res}} \;,\; L = \frac{Z_0\pi}{2\omega_0} \;,\; C_n = \frac{1}{\omega_n^2 L} \;, \tag{2.27}$$

[2] Note, that also for $\alpha > 0$ one finds the same resonance condition by demanding the imaginary part of Z'_{in} in Eq. (2.24) to vanish at $l = l_{\mathrm{res}}$. The residual resistive voltage drop is due to the damping of the reflected wave, which thus has smaller amplitude than the incident one.

into Z'_{in} in Eq. (2.26) enables a mapping onto a serial LCR circuit [53, 54].

This is utilized in the following, where the coupling to the input-output-circuitry is readopted. Therefore, the resonator part is from now on described as the equivalent LCR circuit (see Fig. 2.4(c)). Further insight into the influence of the inductive coupling via L_{c} and the resistive loading with Z_{M} on the resonator properties can be gained regarding Thévenin's equivalent circuit of the input-output-circuitry. Using Thévenin's theorem [58, 59][3], the parallel circuit of Z_{M} and L_{c} can be transformed into a serial circuit with the transformed parameters [53] (see Fig. 2.4(d))

$$L^* = \frac{L_{\mathrm{c}} Z_{\mathrm{M}}^2}{Z_{\mathrm{M}}^2 + \omega^2 L_{\mathrm{c}}^2} \approx L_{\mathrm{c}} \ , \ R^* = \frac{\omega^2 L_{\mathrm{c}}^2 Z_{\mathrm{M}}}{Z_{\mathrm{M}}^2 + \omega^2 L_{\mathrm{c}}^2} \approx \frac{\omega^2 L_{\mathrm{c}}^2}{Z_{\mathrm{M}}} \ , \tag{2.28}$$

where the approximate expressions are valid for small coupling inductances $\omega L_{\mathrm{c}} \ll Z_{\mathrm{M}}$. With this transformation, the total inductance and resistance of the fully serial circuit can be written as $L_{\mathrm{tot}} = L + L^*$ and $R_{\mathrm{tot}} = R + R^*$, respectively. The shifted resonance frequency due to the inductive loading is given by $\omega'_n = 1/\sqrt{L_{\mathrm{tot}} C_n}$. The quality factor of the serial circuit, which due to the inductive and resistive loading is called *loaded* quality factor Q_{L}, obeys $Q_{\mathrm{L}} = \omega'_n L_{\mathrm{tot}} / R_{\mathrm{tot}}$. In general, a splitting into internal losses produced by the resonator $(1/Q_{\mathrm{i}})$ and losses due to the coupling to the input-output-circuit $(1/Q_{\mathrm{e}})$ is not possible. However, for small coupling inductances satisfying $\omega L_{\mathrm{c}} \ll Z_0$ and $L_{\mathrm{c}} \ll L_n$, the resonance frequency and total inductance are given by $\omega'_n \approx \omega_n$ and $L_{\mathrm{tot}} \approx L$, respectively. Then, the overall loss can be separated as

$$\frac{1}{Q_{\mathrm{L}}} = \frac{R_{\mathrm{tot}}}{\omega_n L} \approx \frac{R}{\omega_n L} + \frac{2R^*}{\omega_n L} = \frac{1}{Q_{\mathrm{i}}} + \frac{1}{Q_{\mathrm{e}}} \ . \tag{2.29}$$

Within this approximation for weak coupling to the input-output-circuit, the external quality factor is given by

$$Q_{\mathrm{e}} = \frac{Z_{\mathrm{M}} L}{2\omega_n L_{\mathrm{c}}^2} \ . \tag{2.30}$$

[3] Thévenin's theorem states that each combination of current and voltage sources and impedances can be transformed into a serial circuit with transformed parameters.

2.1.4. Scattering matrix and transmission $ABCD$ matrix

A sophisticated representation of two-port devices, which connects the reflected and transmitted voltage waves to the incident ones is given by the scattering matrix $\hat{S}$ (see Fig. 2.5(a)), which is defined as [54]

$$\begin{pmatrix} U_1^- \\ U_2^- \end{pmatrix} = \begin{pmatrix} S_{11} & S_{12} \\ S_{21} & S_{22} \end{pmatrix} \begin{pmatrix} U_1^+ \\ U_2^+ \end{pmatrix} = \hat{S} \begin{pmatrix} U_1^+ \\ U_2^+ \end{pmatrix} \ , \tag{2.31}$$

where U_n^+ is the amplitude of the voltage wave incident on port n, and the amplitude of the voltage wave reflected from port n is denoted by U_n^-. Each element of the matrix is complex valued, reflected in an amplitude and a phase, and can be determined as [54]

$$S_{ij} = \left. \frac{U_i^-}{U_j^+} \right|_{U_k^+ = 0, k \neq j} \ . \tag{2.32}$$

Thus, e.g. S_{21} can be obtained by driving port 1 with an incident voltage U_1^+ and measuring the transmitted voltage U_2^- at port 2, while keeping the incident voltages at ports other than port 1 at zero. Measuring the scattering matrix $\hat{S}$ was in fact the standard approach for the microwave characterization of any device during this thesis. Moreover, the scattering matrix $\hat{S}$ enables a very elegant description of the transmitted and reflected power. Assuming for example a wave generated at port 1 of a network analyzer (Z_M) with an incident power of $P_{\mathrm{in},1} = 1/2 \cdot |U_1^+|^2/Z_\mathrm{M}$, the power reflected to port 1 and the power transmitted to port 2, while assuming both ports to have a measurement impedance of Z_M, are given by

$$P_{\mathrm{refl},1} \overset{U_1^- = S_{11} U_1^+}{=} \frac{1}{2} \frac{|S_{11} U_1^+|^2}{Z_\mathrm{M}} = |S_{11}|^2 P_{\mathrm{in},1} \ , \ P_{\mathrm{trans},2} = |S_{21}|^2 P_{\mathrm{in},1} \ . \tag{2.33}$$

In general, the scattering matrix $\hat{S}$ allows the description of a circuit network of an arbitrary number of ports. In many cases, however, such circuits have two ports.

For two-port networks, there is an alternative formalism, which interconnects the currents and voltages on either side of the network. The so-called transmission $ABCD$ matrix (Fig. 2.5(b)) is defined via [54]

$$\begin{pmatrix} U_1 \\ I_1 \end{pmatrix} = \begin{pmatrix} A & B \\ C & D \end{pmatrix} \begin{pmatrix} U_2 \\ I_2 \end{pmatrix} = \hat{T} \cdot \begin{pmatrix} U_2 \\ I_2 \end{pmatrix} \ , \tag{2.34}$$

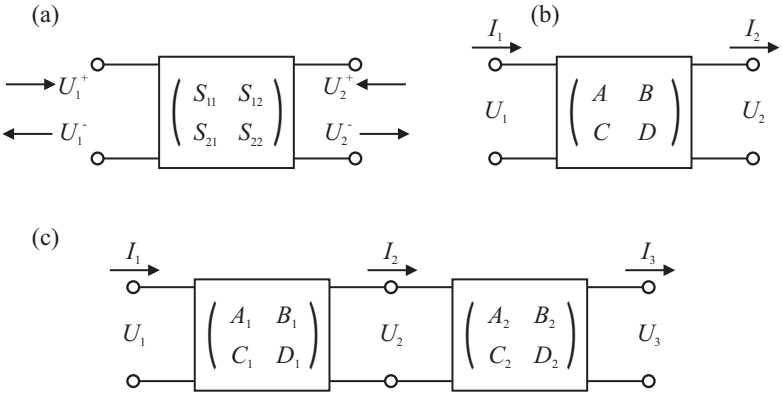

Figure 2.5.: Schematic illustration of (a), the scattering matrix $\hat{S}$, which connects reflected and transmitted voltage waves to the incident ones, and (b), the transmission $ABCD$ matrix, linking the currents and voltages of one port to those of the other port, and (c), a cascade of two-port networks, which can be efficiently described by multiplication of $ABCD$ matrices.

where $\hat{T}$ is the $ABCD$ matrix with the elements [54]

$$A = \left.\frac{U_1}{U_2}\right|_{I_2=0}, \; B = \left.\frac{U_1}{I_2}\right|_{U_2=0}, \; C = \left.\frac{I_1}{U_2}\right|_{I_2=0}, \; D = \left.\frac{I_1}{I_2}\right|_{U_2=0} . \tag{2.35}$$

The usefulness of this formalism becomes clear regarding cascaded two-port networks (Fig. 2.5(c)). Within this formalism, the total $ABCD$ matrix $\hat{T}_{\text{tot}}$ of the serial connection can be calculated by simply multiplying the $ABCD$ matrix of each individual network as

$$\begin{pmatrix} U_1 \\ I_1 \end{pmatrix} \overset{\text{Eq. (2.34)}}{=} \hat{T}_1 \cdot \begin{pmatrix} U_2 \\ I_2 \end{pmatrix} \overset{\text{Eq. (2.34)}}{=} \underbrace{\hat{T}_1 \cdot \hat{T}_2 \cdot \ldots \cdot \hat{T}_n}_{\hat{T}_{\text{tot}}} \begin{pmatrix} U_n \\ I_n \end{pmatrix} . \tag{2.36}$$

Of particular importance for the resonators presented in Sec. 2.1.3 are the $ABCD$ matrices of an impedance Z in series with one of the lines, and an impedance Z shunting the two lines of the TL (Fig. 2.6(a), (b)). They can be calculated to obey

$$\hat{T}_{Z,\text{series}} = \begin{pmatrix} 1 & Z \\ 0 & 1 \end{pmatrix} \quad , \quad \hat{T}_{Z,\text{shunt}} = \begin{pmatrix} 1 & 0 \\ 1/Z & 1 \end{pmatrix} . \tag{2.37}$$

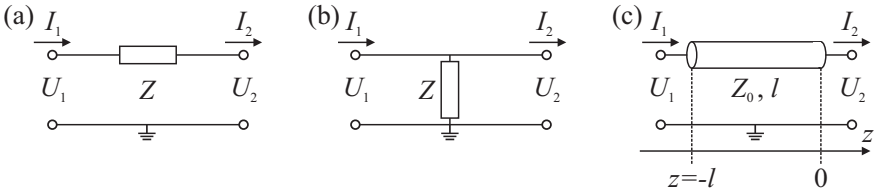

Figure 2.6.: Circuit model of an impedance Z in series with one of the lines of the TL, (a), and an impedance Z shunting the two lines of the TL, (b). Panel (c) depicts the circuit of a TL with characteristic impedance Z_0 and length l.

For the $ABCD$ matrix of a TL of length l, it is advisable to relate the parameters of the $\hat{S}$ matrix to the ones of the $ABCD$ matrix at both ends of the TL (see Fig. 2.6(c)). Setting $z = 0$ on the right end yields (cf. Eq. (2.19))

$$U_2 = U_2^+ + U_2^- \quad , \quad I_2 = -\frac{-U_2^+}{Z_0} + \frac{U_2^-}{Z_0} \ , \tag{2.38}$$

for the right hand side. Solving for $U_2^\pm$ separately can be used to write the current and voltage on the left end $z = -l$, as a function of the ones on the right end as

$$\begin{aligned} U_1 &= U_1^+ + U_1^- = U_2^- e^{\gamma l} + U_2^+ e^{-\gamma l} = U_2 \cosh \gamma l + I_2 Z_0 \sinh \gamma l \ , \\ I_1 &= \frac{U_1^+}{Z_0} - \frac{U_1^-}{Z_0} = \frac{U_2^-}{Z_0} e^{\gamma l} - \frac{U_2^+}{Z_0} e^{-\gamma l} = \frac{U_2}{Z_0} \sinh \gamma l + \cosh \gamma l \ . \end{aligned} \tag{2.39}$$

Comparing with the definition of the $ABCD$ matrix results in

$$\hat{T}_{\mathrm{TL}} = \begin{pmatrix} \cosh \gamma l & Z_0 \sinh \gamma l \\ \frac{1}{Z_0} \sinh \gamma l & \cosh \gamma l \end{pmatrix} \tag{2.40}$$

for the $ABCD$ matrix of a TL with a characteristic impedance Z_0 and length l.

Briefly summarizing, on the one hand we have the elements of the scattering $\hat{S}$ matrix, which represent a ***measure*** of both the reflected and transmitted amplitudes of the voltage waves as well as the related powers. On the other hand, we have the transmission $ABCD$ matrix allowing to interconnect the currents and voltages at either side of the two-port network such that more complex circuits consisting of cascaded two-port networks can be

described in a building-block fashion. Thereby, the connection is established by using the *characteristic properties* of these building-blocks, i.e. the impedances Z (see Eqs. (2.37), (2.40)), wherefore the $ABCD$ matrix represents ***circuit parameters***. Accordingly, combining both formalisms offers the possibility of relating circuit parameters to measurement results.

Therefore, the voltage $U_1 = U_1^+ + U_1^-$ and current $I_1 = U_1^+/Z_\mathrm{M} - U_1^-/Z_\mathrm{M}$ at port 1 of a measurement apparatus can be used to solve $U_1^\pm$ separately. Using the definition of the $ABCD$ matrix in Eq. (2.36), U_1 and I_1 can be expressed in terms of the $ABCD$ matrix elements and the voltage and current at port 2 (U_2, I_2). As an example, the forward scattering parameter S_{21}, measured at an impedance Z_M, can be obtained as (cf. Eq. (2.32))

$$S_{21} = \left.\frac{U_2^-}{U_1^+}\right|_{U_2^+=0} = \frac{2}{A + B/Z_\mathrm{M} + CZ_\mathrm{M} + D} \,. \tag{2.41}$$

In general, the impedances connected to the $ABCD$ matrix elements depend on frequency ω. Thus, $S_{21}(\omega)$ also is a function of frequency and can be used to calculate the expected outcome of spectroscopic measurements, or to validate approximations of circuit models.

As a final part of this section, the above-mentioned building-block system is used to demonstrate the suitability of approximating an inductively coupled half-wavelength resonator as a serial LCR circuit. Therefore, the $ABCD$ matrix multiplication for the cascaded circuits presented in Figs. 2.4(b) and (c) are calculated. Using Eq. (2.41) leads to the spectra shown in Fig. 2.7. Close to the resonances, the calculated transmission of the TL representation and the equivalent LCR circuit agree well. Accordingly, close to resonance best fits assuming a Lorentzian lineshape can be performed in order to extract the quality factor and the resonance frequency of a CPW TL resonator.

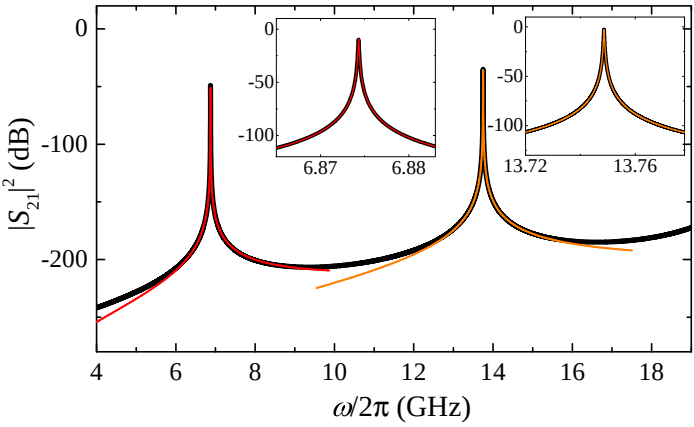

Figure 2.7.: Comparison of the TL representation and the equivalent LCR circuit. Shown are the amplitudes of the calculated forward scattering parameter $|S_{21}(\omega)|$ as a function of the frequency ω using the $ABCD$ matrices and Eq. 2.41. Insets show zooms close to the resonances.

2.2. Basics of superconductivity

In this section a brief introduction of the behavior of superconductors in magnetic fields is given. In particular, the high frequency response of superconductors in magnetic fields is discussed. Since there have been a lot of such investigations in our group in the past [49, 60], the presentation of the following section is held close to these works.

2.2.1. Type-I and Type-II superconductors

Superconductivity was discovered by H. K. Onnes in 1911, while he performed the first experiments with liquefied Helium and studied the temperature dependence of mercury [61]. He found, that below the nowadays called critical temperature T_c of the superconductor, the electrical resistance drops below a measurable value. The disappearance of the electrical resistivity is only one identifying feature of superconductors. Another hallmark, which discriminates superconductors from perfect conductors, was discovered by W. Meissner and R. Ochsenfeld [62]. They found, that the superconductor behaves as an ideal diamagnet, which means that any magnetic field is expelled from the interior of the material due to screening currents at the surface of the superconductor, even if the magnetic field is applied before undergoing the transition at T_c. Both the disappearance of the resistance and the so-called Meissner effect can be explained consistently by virtue of the London equations [63]. While each superconductor can be found in such a Meissner-phase for moderate magnetic fields, most of them show an additional phase, called Shubnikov-phase, for higher magnetic fields, in which flux can enter the material in form of quantized magnetic vortices, called Abrikosov vortices [64–66]. Sketches of the phase diagrams for a type-I and a type-II superconductor depending on the magnetic field B and the temperature T are shown in Fig. 2.8(a) and (b), respectively. With increasing magnetic field, a type-I superconductor is in the Meissner-phase and behaves as an ideal diamagnet until the critical value of B_c is reached. At that point, the superconducting state breaks down and the material becomes normal conducting. The temperature dependence of the critical field B_c was found empirically to behave as $B_c \propto (1 - T/T_c)^2$. A type-II superconductor, however, has two critical fields, B_{c1} and B_{c2}. For magnetic fields smaller than B_{c1}, the type-II superconductor is in the Meissner-phase, as a type-I su-

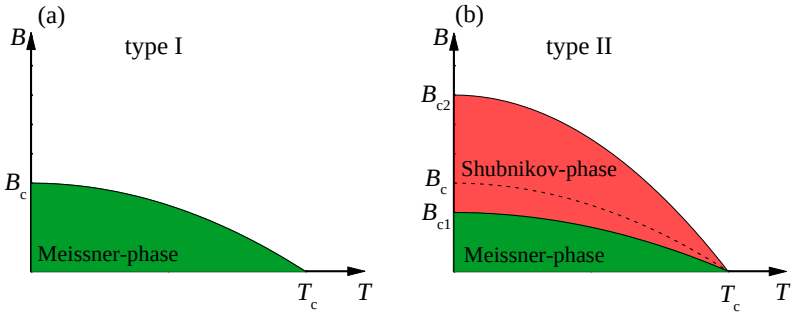

Figure 2.8.: Sketches of the phase diagram of a type-I (a) and a type-II superconductor (b) as a function of the magnetic field B and the temperature T. The critical magnetic fields are denoted by B_c for the type-I, and $B_{\mathrm{c}1}$ and $B_{\mathrm{c}2}$ for the type-II superconductor. T_c is the critical temperature.

perconductor. At the first critical field, however, the material enters the Shubnikov-phase. The superconducting state breaks down at $B_{\mathrm{c}2}$.

A description of the presence of the Shubnikov-phase in type-II superconductors was given by A. A. Abrikosov [66] using the phenomenological Ginzburg-Landau-theory (GL-theory) [67]. Ginzburg and Landau introduced the complex pseudowavefunction Ψ as the order parameter describing the superconducting electrons, as the density of these electrons is given by $n_\mathrm{s} = |\Psi|^2$. By using a variational principle they found two coupled differential equations as a function of the magnetic vector potential, where one of which was for the order parameter Ψ, and the other for the current density $\vec{j}$. Closely related to these equations is the emergence of two characteristic length scales, the Ginzburg-Landau coherence length ξ_GL describing the length scale on which variations of the order parameter do not result in significant energy increase, and the Ginzburg-Landau penetration depth λ_GL, which characterizes how far a magnetic field penetrates the material. Abrikosov noticed, that if $\xi \ll \lambda$, penetration of magnetic flux in form of vortices is more favorable for the material. These vortices consist of a normal conducting region, surrounded by superconducting currents. Due to the unambiguity of the macroscopic wavefunction Ψ, the minimum amount of flux which can be carried by such a vortex is given by the magnetic flux quantum $\Phi_0 = h/2e$. The magnetic field profile B, the circulating supercurrent j and the order parameter $|\Psi|^2$, which is a measure of the Cooper

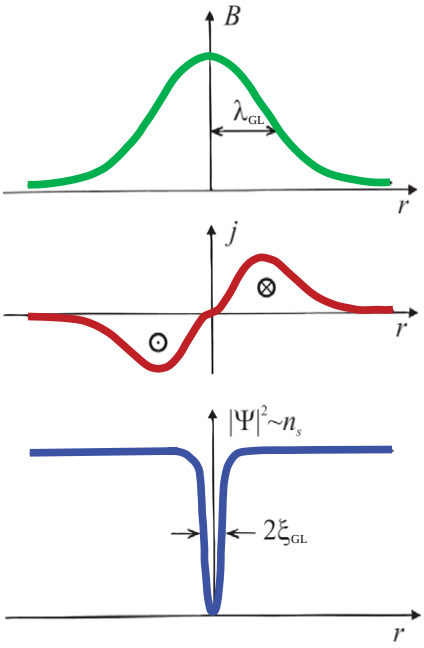

Figure 2.9.: Schematic of the radial dependence of the magnetic field B, current density j and Cooper pair density $|\Psi|^2$ of an Abrikosov vortex (adopted from [49]). For details see text.

pair density, of such an Abrikosov vortex are shown in Fig. 2.9. Around the location of the normal conducting core of the vortex, the superconducting order parameter is suppressed within a radius of $\approx 2\xi_{\mathrm{GL}}$. The magnetic field decays from the center of the core on the length scale of the penetration depth λ_{GL}. These Abrikosov vortices, if they move under the influence of a microwave current, are known to cause dissipation in microwave resonators [50] such as the ones fabricated during this thesis. All of these resonators were made of the type-II superconductor Niobium ($T_{\mathrm{c}} = 9.2\,\mathrm{K}$).

In the following sections, the basic properties of superconductors in the Meissner-phase are briefly discussed. First, the Meissner-phase is described using the London equations. These equations represent the foundation on which the numerical software package 3D-MLSI is based [68]. By using

3D-MLSI, the magnetic field profile of a trap for ultracold atoms will later be studied. Furthermore, the shift of the kinetic inductance due to the circulating Meissner-currents, which causes frequency changes, is discussed. Second, the concept of kinetic inductance is briefly introduced, however, detailed analytical expressions are given in the respective sections.

The London equations

The first theoretical approach for the description of superconducting materials was given by the brothers Fritz and Heinz London in 1935 [63]. They supposed an *acceleration equation* of motion without any friction,

$$\frac{\partial \vec{j}}{\partial t} = \frac{n_s q^2}{m} \vec{E}, \tag{2.42}$$

where q is the charge, and m the mass of the charge carrier. This is the first London equation, which states that, due to the absence of the competition between scattering and acceleration in normal conductors, not the current density itself but its time derivative is proportional to the electric field $\vec{E}$. Taking the curl of Eq. (2.42), one gets

$$\nabla \times \frac{\partial \vec{j}}{\partial t} = -\frac{n_s q^2}{m} \frac{\partial \vec{B}}{\partial t} \ , \tag{2.43}$$

where B is the magnetic field. Using the maxwell equations $\nabla \vec{E} = -\partial \vec{B}/\partial t$ and $\nabla \times \vec{B} = \mu_0 \vec{j}$, yields

$$\Delta \frac{\partial \vec{B}}{\partial t} = \frac{1}{\lambda_\mathrm{L}^2} \frac{\partial \vec{B}}{\partial t}, \tag{2.44}$$

where $\lambda_\mathrm{L} = \sqrt{m/\mu_0 n_s q^2}$ denotes the London penetration depth. Equation (2.44) is a general expression for a perfect conductor, which reveals that the flux remains constant in the interior of the conductor [69]. In contrast, superconductors are known to expel the flux itself, and not only its time derivative. Thus, they supposed that Eq. (2.43) must also be valid for the stationary case, leading to

$$\nabla \times \vec{j} = -\frac{n_s q^2}{m} \vec{B} \ \text{ and } \ \Delta \vec{B} = \frac{1}{\lambda_\mathrm{L}^2} \vec{B}, \tag{2.45}$$

where the first part is the second London equation, and the second part describes the field expulsion, and thus, the Meissner effect.

Kinetic inductance

The concept of kinetic inductance is very old and related to the idea that electrical charge carriers possess inertia. For a correct description of the total inductance L, consequently, the kinetic part L_k must be added to the geometric part L_g,

$$L = L_\mathrm{g} + L_\mathrm{k}. \tag{2.46}$$

While the fraction of the kinetic part of the overall inductance is rather small for normal conductors, for superconductors it can play an important role. This can be understood intuitively by comparing the resistance R and the kinetic reactance ωL_k of a normal conducting wire at a frequency ω,

$$R = \left[\frac{m_e}{n_e e^2} \cdot \frac{l}{A}\right] \frac{1}{\tau} \qquad \omega L_\mathrm{k} = \left[\frac{m_e}{n_e e^2} \cdot \frac{l}{A}\right] \omega, \tag{2.47}$$

where m_e, e and n_e are mass, charge and number density of the current carriers, and l and A are length and cross-sectional area of the wire, τ is the electron collision time [70]. In contrast to normal conductors, for superconductors which apply to $\tau \to \infty$, ωL_k can dominate R.[4]

This effect is nowadays used for applications such as kinetic inductance detectors [71, 72]. For the resonators investigated during this thesis, however, the influence of the kinetic inductance mainly plays an important role for resonators studied as a function of temperature or magnetic field. Calculating the total kinetic energy of Cooper pairs, one finds expressions like

$$L_\mathrm{k} = \mu_0 \lambda_\mathrm{L}^2 g_\mathrm{g1} \ , \tag{2.48}$$

for a superconducting film thickness $t \ll 2\lambda_\mathrm{L}$, and

$$L_\mathrm{k} = \mu_0 \lambda_\mathrm{L}^2 g_\mathrm{g2} \ , \tag{2.49}$$

for $t \gg 2\lambda_\mathrm{L}$, where $g_\mathrm{g1,2}$ are factors depending on the geometry. λ_L denotes the London penetration depth, indicating that the kinetic inductance depends on the temperature and the magnetic field. Exact analytical expressions for g_g are given in the respective sections below.

[4] In fact, for cross-sectional dimensions $\gg \lambda_\mathrm{L}$, the fraction of kinetic inductance turns out to be $\approx 1\%$. However, for superconducting nanowires the kinetic inductance can dominate the geometrical one.

2.3. Perovskite oxides as nonlinear dielectrics

In this section, a brief introduction to the physics of the perovskite oxide $SrTiO_3$ is given. The basic physics of this perovskite is closely related to the physics of ferroelectric $BaTiO_3$, since both Ba^{2+}-ions and Sr^{2+}-ions are of the second main group of the periodic table of elements. Thus, at first, the similarities of these materials are discussed, whereas afterwards distinctions between them are pointed out. The main difference between these materials is the occurrence of a phase called *quantum paraelectric phase*, which can be found for $SrTiO_3$ at low temperatures, and in contrast to ferroelectricity can be understood regarding the temperature dependence of the dielectric properties. However, since the thin films fabricated during the thesis were hardly epitaxial, this section does not strive for a quantitative description and instead an intuitive picture is given.

The ferroelectric perovskite oxides are known to undergo a structural phase transition at a temperature $T = T_{\mathrm{Cu}}$ (called *Curie* temperature) from cubic to tetragonal, in many cases accompanied by the emergence of a spontaneous polarization P. Therefore, before going into the details of microscopic mechanisms causing the phase transition, a macroscopic description on the basis of Landau's theory of phase transitions is given.

2.3.1. Macroscopic description

The unit cell of a perovskite is shown in Fig. 2.10(a) for a temperature $T > T_{\mathrm{Cu}}$. The ionic crystal structure can be described by the formula ABO_3, where the A^{2+}-site atoms span a cubic sublattice with a transition metal B^{4+}, e.g. Ti^{4+}, in the body center, surrounded by face centered oxygen ions which form an octahedron. For $BaTiO_3$, the above mentioned phase transition occurs at $T_{\mathrm{Cu}} = 393\,\mathrm{K}$, where the oxygen octahedron and the transition metal are offset in opposite direction along the elongated c-axis, breaking the inversion symmetry and creating a spontaneous polarization P (cf. 2.10(b)). Contrary, for $SrTiO_3$, a similar transition emerges at $T \approx 105 - 110\,\mathrm{K}$, which, however, is *not* resulting in a spontaneous polarization. At that point, the crystal undergoes a second-order phase transition from cubic to tetragonal, at which the crystal is continuously deformed such that the a- and b-axes are compressed, satisfying $a = b$, and the c-axis is elongated. In addition, the oxygen octahedron is distorted around the elongated c-axis [73–76].

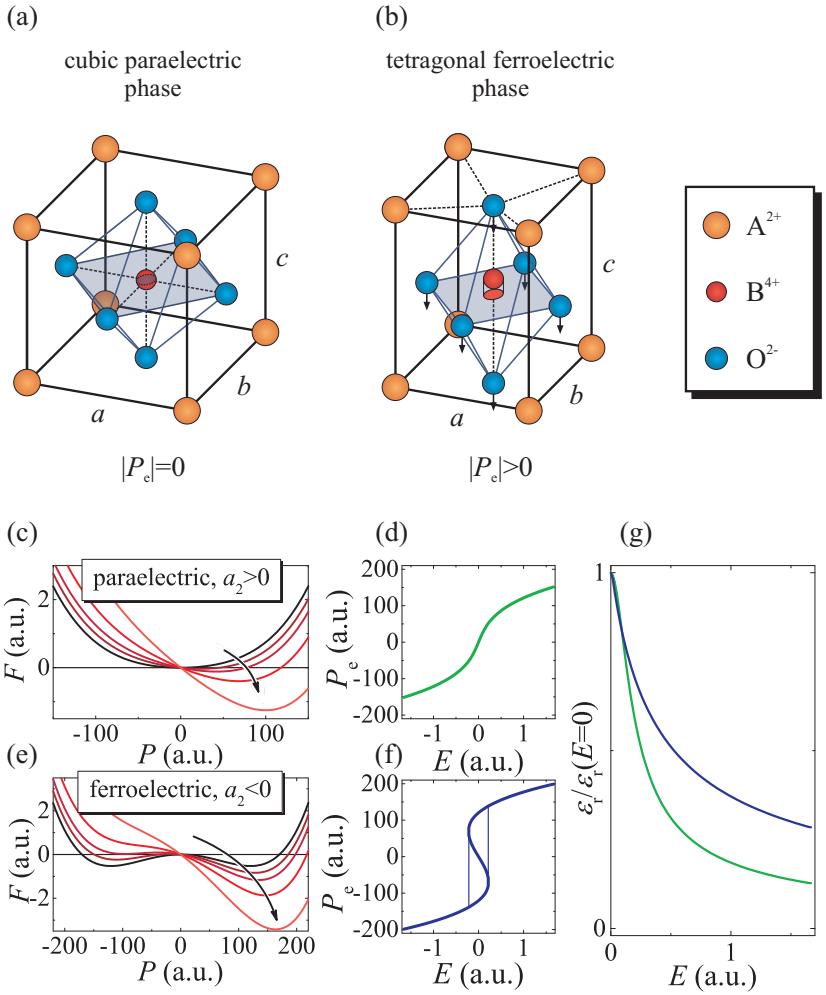

Figure 2.10.: Unit cell and phase transition of perovskite oxides. Crystal structure in the cubic paraelectric phase, (a), and in the tetragonal ferroelectric phase, (b). (c), (d) and (e),(f) respectively show the free energy F and the equilibrium polarization P_e in both the paraelectric and ferroelectric state. (g) dielectric constant normalized to its value at zero field for both states.

Thus, neighboring unit cells rotate in opposite directions due to the sharing of one oxygen atom, making this transition to be named anti-ferrodistortive. This phase transition can be described by using the angle of rotation as order parameter, however, it does not cause strong shifts of the dielectric constant $\varepsilon_{\mathrm{re}}$ of the material, which remains paraelectric, and is hence not considered in the following (cf. Fig. 2 in [77]). More important for $\varepsilon_{\mathrm{re}}$ is another phase transition, which is not due to a crystal deformation and takes place at $T = 37\,\mathrm{K}$ from a paraelectric to a quantum paraelectric state [77–82]. Thereby, the shifting of the oxygen octahedron and the transition metal are suppressed by quantum mechanical vacuum fluctuations, which deserves mention below. However, it was partly found by these authors, that by applying a threshold electric field of $\approx 100{-}300\,\mathrm{kV/m}$, a ferroelectric-like temperature dependence of the dielectric constant can be induced, giving $SrTiO_3$ the property of an incipient ferroelectric. Based on this argumentation and the fact that in the following only the electric field dependence is studied, in the framework of Landau's theory (which neglects any kind of fluctuations), the polarization can be used as order parameter describing the order of orientation of the dipolar moments. The free energy F for a second-order phase transition then reads [83–85]

$$F = \frac{1}{2}a_2P^2 + \frac{1}{4}a_4P^4 - \vec{P}\vec{E}\ , \tag{2.50}$$

where a_2 is a temperature dependent coefficient, and $a_4 > 0$ is constant[5]. Furthermore, the energy related to an externally applied electric field $\vec{E}$ is included via $-\vec{P}\vec{E} \stackrel{!}{=} -PE$, where in the following the problem is reduced to one dimension. The equilibrium polarization $|P_{\mathrm{e}}|$ of the system can then be obtained by minimizing the free energy F.

Electric field dependence

The Landau theory can thus be used to fit experimental data with high precision (see [87]) using

$$\frac{\partial F}{\partial P} \stackrel{!}{=} 0 \quad \rightarrow \quad E = a_2P + a_4P^3\ , \tag{2.51}$$

and

$$\frac{\partial E}{\partial P} \approx \frac{1}{\varepsilon_0\varepsilon_{\mathrm{re}}} = a_2 + 3a_4P^2\ , \tag{2.52}$$

[5] Note, that $a_2 = \gamma(T - T_0)$ for ordinary ferroelectrics, and $a_2 = \gamma(T_1/2\coth T_1/2T - T_0)$ for quantum paraelectrics [78, 86]

where the approximation holds for large dielectric constants $\varepsilon_{\mathrm{re}} \approx \chi_{\mathrm{r}}$, ε_0 is the permittivity of free space and χ_{r} is the electric susceptibility. Eqs. (2.51) and (2.52) implicitly describe the electric field dependence of the dielectric constant $\varepsilon_{\mathrm{re}}$ of a perovskite. The free energy F and the corresponding equilibrium polarization $|P_{\mathrm{e}}|$, as well as the resulting dielectric constant $\varepsilon_{\mathrm{re}}$ are shown in Fig. 2.10(c)–(g) for both, the paraelectric ($a_2 > 0$) and the ferroelectric state ($a_2 < 0$).

2.3.2. Microscopic properties of $SrTiO_3$

The investigation of microscopic properties of perovskites is rather old. It began in the 1950s, when Slater came up with the idea of short-range attractive forces between different types of ions and repulsive dipolar forces, induced by a displacement of these ions, which cancel at the Curie temperature [84]. 10 years later, Cochran suggested regarding lattice dynamics, that the oxygen ion polarizability plays a crucial role for the phase transition and found, that the transverse optical phonon mode could soften, which means that at zero phonon momentum and $T = T_{\mathrm{Cu}}$, the phonon frequency tends to zero, causing a crystal instability [88]. The model Cochran proposed was subsequently extended and compared to neutron scattering data in order to find the best fit between models and experiment considering the phonon dispersion relation [89–91]. This comparison led to the model which can be found to the full extent in Refs. [92–97] and references therein. The main aspects shall be briefly outlined in the following, focusing on the dielectric properties rather than the lattice dynamics.

1D model and double-well potential

For the lattice model, each force is represented by a force constant which couples the different ions (cf. Fig. 2.11(a)). One further basic ingredient of the model is the aforementioned polarizability of the oxygen ion, taken into account by a nonlinear core-shell coupling constant [88]. It was found, that the oxygen ion polarizability strongly depends on its crystalline environment, and in the case of perovskite oxides, is large in the direction of neighboring B^{4+} ions and comparatively small in the plane where the oxygen ions are surrounded by the A^{2+} site ions [91, 94]. This anisotropy is taken into account by two different force constants corresponding to both directions. However, measurements indicated that only the direction towards the B^{4+}

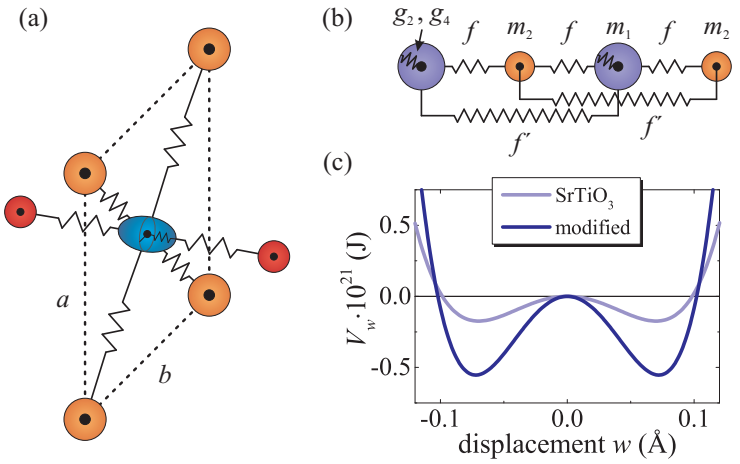

Figure 2.11.: 1D ionic chain model and double well potential. (a) Detail of the $SrTiO_3$ crystal and effective 1D ionic chain model, (b), with the ions being the BO_3^{2-} cluster and the A^{2+} site atoms, respectively. (c) Double well potential for $SrTiO_3$ (light purple) and modified potential (dark purple).

ions is relevant for a reliable fit of the temperature dependence of the soft phonon mode, which enabled a quasi-one-dimensional description [94, 97]. Therefore, the BO_3^{2-} unit is lumped together to a highly polarizable mass m_1, which is illustrated in Fig. 2.11(b). Within this 1D ionic chain model, these *ions*[6] have a charge of $\pm 2e$, where e is the charge of an electron. Then, the total potential energy V for a BO_3^{2-} unit n is given by [94, 97]

$$V = \frac{1}{2}\sum_n \{f'(u_{1n} - u_{1n-1})^2 + f(u_{2n} - v_{1n})^2 + f(u_{2n+1} - v_{1n})^2 + g_2(v_{1n} - u_{1n})^2 + \frac{1}{2}(v_{1n} - u_{1n})^4\} \,, \tag{2.53}$$

where u_{in}, v_{in} are the core and shell displacements of the ion $i = \{1, 2\}$, f' and f are second and nearest neighbor harmonic core-core and core-shell coupling constants, and g_2 and g_4 represent the double-well character of the BO_3^{2-} cluster with $g_2 < 0$, $g_4 > 0$. Defining $w_{1n} = u_{1n} - v_{1n}$ and using the

[6] One *ion* is the BO_3^{2-} cluster, the other *ion* is the A^{2+} ion of the unit cell

adiabatic condition $\partial V/\partial v_{1n}$, which states that the shells always assume the position of minimal energy, one can calculate the potential energy for the displacement of one single BO_3^{2-}-cluster. This double-well potential is shown for $SrTiO_3$ in Fig. 2.11(c) ($w = w_{1n}$ for the nth cell), where the parameters for the force constants were taken from [97] [7].

Ferroelectric vs. quantum paraelectric state

In addition to the potential of $SrTiO_3$, a modified double-well potential is shown in Fig. 2.11(c). The parameters were chosen such that the equilibrium displacement w_e is the same, but the potential is deeper and thus the barrier between the two wells higher. With these two double-well potentials an intuitive picture for the discrimination between a ferroelectric and a quantum paraelectric state can be given.

From the quantum mechanical side, the two wells represent pseudo-spin states between which tunneling processes can take place. The probability for such a tunneling process depends on the barrier height between the two wells. Thus, regarding the two double-well potentials in Fig. 2.11(c), tunneling is more probable for the potential of $SrTiO_3$ than for the modified deeper potential. The 1D ionic chain can be described by using an Ising-like spin model with the Hamiltonian [77, 81, 98]

$$\hat{H} = -\Omega \sum_i S_i^x - \frac{1}{2} \sum_{i,j} J_{ij} S_i^z S_j^z - 2dE \sum_i S_i^z \ , \tag{2.54}$$

where $\hat{S} = (S_x, S_y, S_z)$ represent the dipolar degrees of freedom of the pseudo-spin. In Eq. (2.54), the first two terms constitute the transverse Ising model with the tunneling integral Ω representing the probability of tunneling processes, and the exchange coupling constant between different spins J_{ij}. The last term accounts for effects of an externally applied electric field E with the strength of the electric dipole moments d. In the mean-field approximation one finds [77, 81, 98]

$$\langle S^z \rangle = \frac{1}{2} \frac{J_0 \langle S^z \rangle + 2dE}{H} \tanh\left(\frac{H}{2k_B T}\right) \ , \tag{2.55}$$

[7] $f = 144.05\,\mathrm{kg/s^{-2}}$, $f' = 12.68\,\mathrm{kg/s^{-2}}$, $g_2 = -14.1\,\mathrm{kg/s^{-2}}$, $g_4 = 1.57 \cdot 10^{15}\,\mathrm{kgm^2/s^{-2}}$

where $H = \sqrt{\Omega^2 + (J_0\langle\hat{S}\rangle + 2dE)^2}$ and $J_0 = \sum_j J_{ij}$. Eq. (2.55) has to be solved self-consistently. Then, the polarization P and dielectric susceptibility $\chi_r(E)$ can be calculated using

$$P = 2nd\langle S^z\rangle \quad , \quad \chi_r(E) = \frac{1}{\varepsilon_0}\frac{\partial P}{\partial E} \; , \tag{2.56}$$

where n is the density of dipolar moments and ε_0 is the permittivity of free space. The differences between the ferroelectric and the quantum paraelectric state become obvious by looking at the temperature dependence of the dielectric constant ε_{re}, which is shown in Fig. 2.12. The curves show the tem-

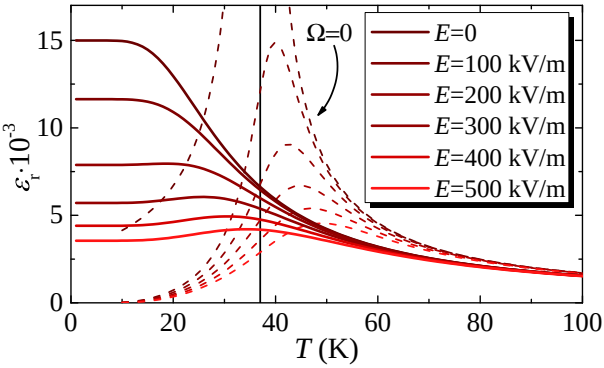

Figure 2.12.: Comparison of the Ising spin model with tunneling (straight lines) and without tunneling (dashed lines) for electric fields E from 0 to 500 kV/m in steps of 100 kV/m.

perature dependence of the dielectric constant ε_r for $\Omega = 0$ and $\Omega/k_B = 87\,\mathrm{K}$ (taken from [81]), calculated solving Eq. (2.55) self-consistently and using Eq. (2.56). For $\Omega = 0$ the behavior is consistent with predictions based on Landau's theory, i.e. a pronounced peak close to the Curie point. For $\Omega \gg 0$, the large tunneling probability causes strong perturbations of the temperature dependence. Around the Curie point at 37 K there is no pronounced peak. Instead the dielectric constant is increased for smaller temperatures to values of several 10^5, saturating at a fixed value at temperatures below 15 K. In addition, at low temperatures, e.g. 4.2 K, the dielectric properties depend strongly on the electric field E. Thus, $SrTiO_3$ is used as a tunable nonlinear dielectric rather than $BaTiO_3$.

Dielectric loss of $SrTiO_3$

Using such a nonlinear dielectric for microwave applications introduces additional dielectric loss. During the end of the last and the beginning of the present century the modeling of the loss mechanisms for centro-symmetric ferroelectrics at microwave frequencies have been studied extensively [99–109]. Instead of going into the details of the loss mechanisms the predominant sources of microwave dissipation are rather briefly listed below (following [108]):

1. Fundamental loss related to multiphonon scattering of the above mentioned soft ferroelectric mode,
2. Quasi-Debye mechanism of loss [106],
3. transformation of microwave electric field oscillations into acoustic oscillations due to field generated by charged defects, e.g. oxygen ions,
4. low frequency relaxation,

where the latter of these points is most likely to have only a small contribution at low temperatures. Typical values for the dielectric loss tangent of $SrTiO_3$ thin films vary between some 10^{-3} and some 10^{-2} [110, 111].

3 Tunable CPW resonators for experiments at a temperature of 4 K

In this section two different concepts of tuning the resonance frequency at a temperature of about 4 K are discussed. First, a nonlinear capacitor containing a nonlinear dielectric is used to change the resonance frequency *in situ* by applying a dc voltage. A full model is employed enabling the extraction of the complex dielectric function of the nonlinear dielectric. Hysteresis effects in magnetic fields as well as nonlinear effects as a function of the applied microwave power are discussed. These resonators have a tunability of up to 50 MHz, while still providing relatively good quality factors.

The second approach is based on the temperature dependent kinetic inductance of a superconductor at temperatures $T/T_c > 0.4$. The superconducting structures are made of niobium (Nb) with a critical temperature of $T_{c,Nb} = 9.2\,K$. Increasing the temperature from $\approx 4\,K$, i.e. temperatures of liquid helium, to $\approx 8.5\,K$, the resonance frequency was found to be tunable by up to 100 MHz.

3.1. Tunable CPW resonators using nonlinear dielectrics[1]

3.1.1. Principle and sample design

This section starts with a short introduction of the resonator and its basic working principle. Subsequently, the input impedance of the resonator is calculated in order to obtain analytical expressions for the resonator properties. These analytical expressions are mandatory for the analysis of the experimental results.

Working principle of the device

A schematic of the device is shown in Fig. 3.1(a), demonstrating the basic idea. The device consists of a typical CPW transmission line with a center conductor and two ground planes (grey), which is short ended at two sides (purple shorts), making this device an inductively coupled half-wavelength ($\lambda/2$)-resonator. Along the transmission line a tuning capacitor (green) is added in the middle between those two coupling shorts. At that position the amplitude of the electric field of the resonant ground mode (solid and dashed orange lines) has an antinode. The basic idea is, that by varying the capacitance of the capacitor *in situ*, and thereby changing the total capacitance, the resonance frequency can be changed. In the following, a model is established allowing one to calculate the resonance frequency as a function of the capacitance. The circuit representation of the device is drawn in Fig. 3.1(b). The device can be modeled as a transmission line with a characteristic impedance Z_0 and a length l_{res}, which is terminated at the two sides of the resonator by the coupling inductances denoted L_{c}. The tuning capacitor is modeled as a parallel combination of a capacitance C_{t} and a conductance G_{t}, which shunts the transmission line in the middle. This conductance G_{t} accounts for loss introduced by the added capacitor. The model includes the coupling to the input and output ports with internal load impedances Z_{L}. In the following, only the ground mode is considered, where its spatial structure can be associated with a half-wavelength between the coupling shorts.

[1] A manuscript containing results as described in this chapter is in preparation: B. Ferdinand, D. Bothner, D. Koelle, R. Kleiner, "Tunable superconducting CPW resonators using a lumped element STO capacitor".

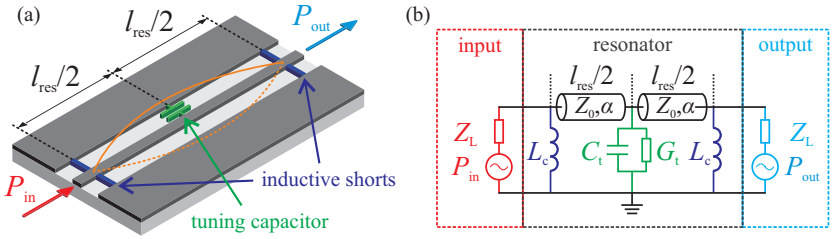

Figure 3.1.: Tunable CPW resonator with tuning capacitor. (a) Sketch of the device, showing a CPW transmission line (grey) with the tuning capacitor (green) in the center between the two inductive shorts (purple). P_{in} (red) and P_{out} (blue) respectively denote the microwave input and output power. The solid and dashed orange lines indicate the electric field amplitude. (b) Circuit used to model the device, with the resonator part in the middle (for details see text), flanked by the input and output port, modeled as a microwave source with an internal load impedance of $Z_{\mathrm{L}} = 50\,\Omega$.

The forward scattering parameter $S_{21}(\omega)$ of the circuit, where ω is the frequency, can be calculated via the $ABCD$-matrix method [54]. The matrices for the coupling inductance L_{c}, the tuning capacitance C_{t}, G_{t}, and a transmission line with a length of $l = l_{\mathrm{res}}/2$ are given by

$$M_{L_{\mathrm{c}}} = \begin{pmatrix} 1 & i\omega L_{\mathrm{c}} \\ 0 & 1 \end{pmatrix}, M_{C_{\mathrm{t}},G_{\mathrm{t}}} = \begin{pmatrix} 1 & 0 \\ i\omega C_{\mathrm{t}} + G_{\mathrm{t}} & 1 \end{pmatrix}, \tag{3.1}$$

$$M_{\mathrm{TL}} = \begin{pmatrix} \cosh(\gamma l) & Z_0 \sinh(\gamma l) \\ \frac{1}{Z_0}\sinh(\gamma l) & \cosh(\gamma l) \end{pmatrix}. \tag{3.2}$$

The total $ABCD$ matrix M_{tot} of the circuit is obtained by performing the matrix multiplication

$$M_{\mathrm{tot}} = \begin{pmatrix} A & B \\ C & D \end{pmatrix} = M_{L_{\mathrm{c}}} M_{\mathrm{TL}} M_{C_{\mathrm{t}},G_{\mathrm{t}}} M_{\mathrm{TL}} M_{L_{\mathrm{c}}}, \tag{3.3}$$

where $\gamma = \alpha + i\beta$, α and $\beta = \omega\sqrt{L_l C_l}$ are the real and imaginary part of the propagation constant, and L_l and C_l are the inductance and capacitance per unit length of the transmission line, respectively. The forward scattering parameter S_{21} taken at the output port with impedance Z_{L} can be calculated using

$$S_{21} = \frac{2}{A + B/Z_{\mathrm{L}} + CZ_{\mathrm{L}} + D}. \tag{3.4}$$

The corresponding transmitted power is given by $P_{\mathrm{out}} = |S_{21}|^2 P_{\mathrm{in}}$. For both $G_{\mathrm{t}} = 1 \cdot 10^{-6}$ (black) and $G_{\mathrm{t}} = 5 \cdot 10^{-6}$ (pink), P_{out} is plotted in Fig. 3.2 as a function of the frequency ω for values of C_{t} varying from 0 to 100 fF in steps of 20 fF. For these calculations a damping of the transmission line of $\alpha = 10^{-2}\,\mathrm{m}^{-1}$, a coupling inductance of $L_{\mathrm{c}} = 3.28\,\mathrm{pH}$ and a load impedance of $Z_{\mathrm{L}} = 50\,\Omega$ is assumed. The calculations show that by increasing the capacitance C_{t} the resonance is shifted towards smaller frequencies.

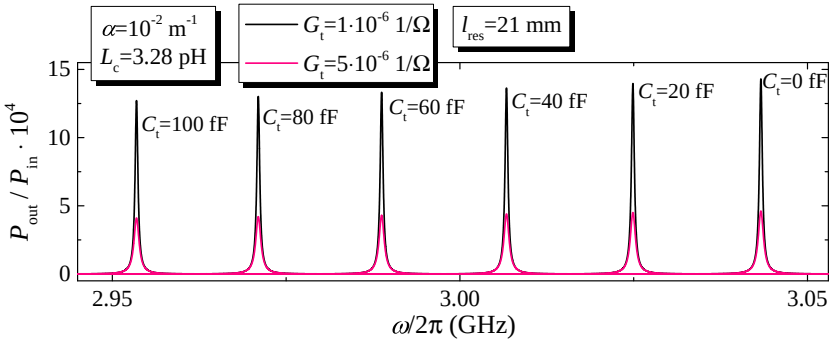

Figure 3.2.: Relative transmitted power $P_{\mathrm{out}}/P_{\mathrm{in}}$ as a function of the frequency ω for combinations of $C_{\mathrm{t}} = 0 - 100\,\mathrm{fF}$ and $G_{\mathrm{t}} = 1 \cdot 10^{-6}$ (black solid line), $G_{\mathrm{t}} = 5 \cdot 10^{-6}$ (pink solid line).

3.1.2. Sample fabrication and device

The fabrication process of the resonators is schematically shown in Fig. 3.3. To form the structure a 330 μm thick r-cut sapphire wafer is used with lateral dimensions of 12x4 mm^2. A two-layer process is used, starting with the deposition of the nonlinear dielectric. A 100 nm thick film of STO is grown by pulsed laser deposition, followed by 15 minutes of annealing at $T = 850\,^{\circ}\mathrm{C}$ (Fig. 3.3(a)). The dielectric is structured as a rectangle with the dimensions $200 \times 30\,\mu\mathrm{m}^2$, indicated by an orange color in Fig. 3.3(a)-(c) and (f), by means of optical lithography and Ar^+-ion milling (Fig. 3.3(b), (c)). Results of a XRD analysis of a $SrTiO_3$ thin film, cf. Appendix A (Sec. A), indicate that the film is polycrystalline with some preferential order. Subsequently, a 300 nm thick niobium film is sputtered on top of the structure (Fig. 3.3(d)). After another optical lithography step and reactive ion etching with SF_6

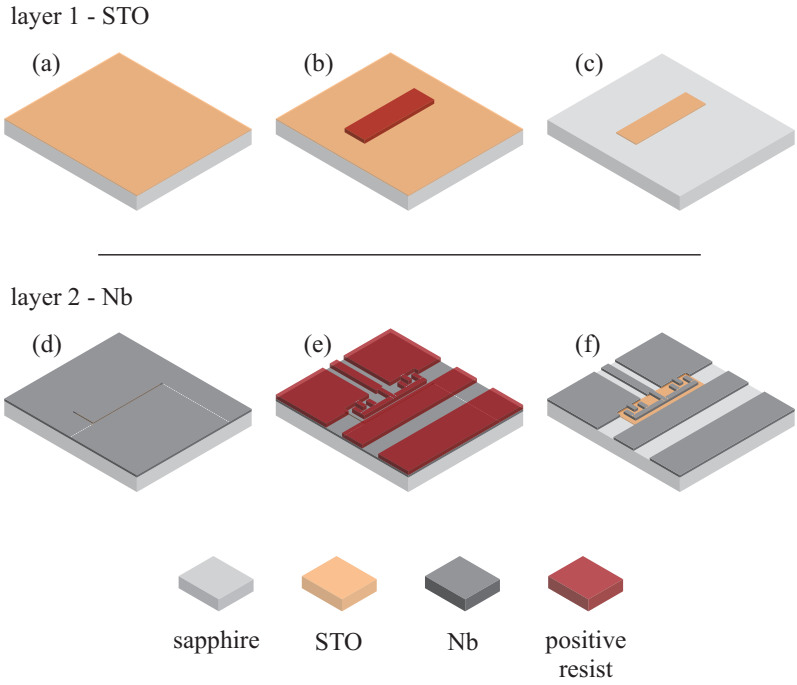

Figure 3.3.: Fabrication steps used for the tunable resonator. Layer 1 - STO deposited by means of pulsed laser deposition (a), optical lithography (positive resist) (b) and Ar^+-ion milling (c). Layer 2 - sputtered niobium thin film (d), structured using optical lithography (e) and reactive ion etching with SF_6.

(Fig. 3.3(e), (f)) the structure shown in Fig. 3.4(a) is obtained, forming an inductively coupled half wavelength CPW resonator with an additional nonlinear dielectric capacitance C_t in the middle between the two coupling shorts with inductance L_c. The meandered TL has cross-sectional dimensions of $S = 50\,\mu$m and $W = 25\,\mu$m (cf. Fig. 3.4(b)), leading to a characteristic impedance of $Z_0 \approx 50\,\Omega$.

The overall structure is shown in Fig. 3.4(a). The niobium parts are represented by the dark grey areas, the orange part indicates the nonlinear dielectric and the bright grey parts represent the substrate. At its left and right end the center conductor has increased cross-sectional dimensions for

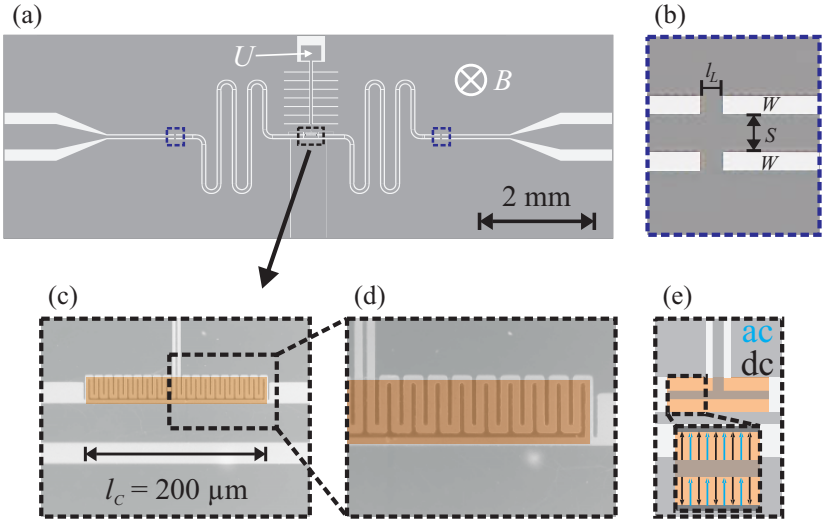

Figure 3.4.: Design of the resonators showing (a) the layout of the overall structure and zoomed optical images of (b) one of the inductive shorts and (c), (d) the tuning capacitor. The niobium parts are represented by the dark grey areas, the orange part indicates the nonlinear dielectric and the bright grey parts represent the substrate. In (a) the dc voltage U applied to the tuning capacitor is indicated. The lengths S, W and l_L are introduced in (b), the length l_C is introduced in (c). Graph (d) is a further zoom into the area of the tuning capacitor and (e) sketches the electric field distribution due to the dc bias U and a snapshot of the ac field distribution induced by the resonator.

the connection to SMA connectors. The TL is terminated at two sides by coupling shorts, such that the geometric length of the $\lambda/2$ resonator is $l_{\mathrm{res}} = 21\,\mathrm{mm}$. These shorts shunt the resonator to both ground planes. Each short has the dimensions $W = 25\,\mu\mathrm{m}$ and $l_L = 30\,\mu\mathrm{m}$ (Fig. 3.4(b)). The parallel combination of the shorts to the ground planes leads to a coupling inductance of $L_{\mathrm{c}} = 3.28\,\mathrm{pH}$.

In the middle between the two coupling shorts along the waveguide a tuning capacitor is added, cf. Fig. 3.4(c) and (d). It is patterned in one of the two gaps between center conductor and ground plane and contains the nonlinear dielectric. The capacitor can be biased with a dc voltage U. The dc bias electrode consists of a two parts. The first is a comb-like structure forming an interdigitated capacitor together with a similar

structure patterned into the upper ground plane. The second is a connecting link to the bond pad, which splits the upper ground plane in two halves. The capacitor has a longitudinal extension of $l_C = 200\,\mu$m. Each finger of the interdigitated capacitor has a length of $a = 25\,\mu$m and a width of $b = 2.2\,\mu$m. The gap between two neighboring fingers is $c = 3.8\,\mu$m. Along the resonator the capacitor is placed at the antinode of the electric field amplitude of the fundamental resonator mode, maximizing its influence on the resonator properties.

The expected electric field distribution in the capacitor is sketched in Fig. 3.4(e). While the dc electric field points from the bias lead to, respectively, the center conductor and the ground plane, the oscillating microwave electric field points from the center conductor to the ground plane, i.e. in the dielectric the dc field and the ac field are partially parallel and partially antiparallel. Due to its small dimensions (a, b, c, $l_C \ll \lambda/2 \approx 21\,$mm), the capacitor can be considered as a lumped element, cf. Fig. 3.4(e).

3.1.3. Model and analysis method

Analysis of the circuit

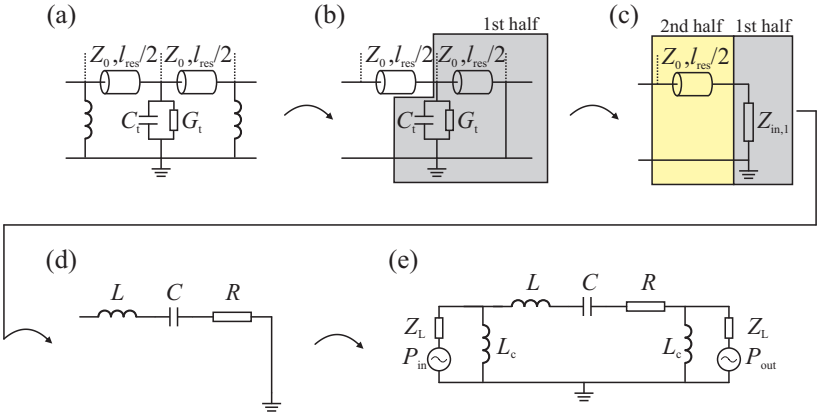

Figure 3.5.: Steps of the derivation of the input impedance Z_{in}.

In order to derive analytical expressions for both the resonance frequency ω_r and the loaded quality factor Q_L of the resonator, the input impedance seen by the microwave source looking towards the resonator is calculated in the following. The circuit used to model the resonator is shown in Fig. 3.5(a). For the calculation of the input impedance Z_in both the load impedance (Z_L) and the inductances L_c of the coupling shorts are neglected for the moment and the first half of the resonator (grey in Fig. 3.5(b)) is modeled as a parallel combination of a lossy capacitor (elements C_t, G_t) and a short-ended segment of a transmission line with a length of $l_\mathrm{res}/2 \approx \lambda/4$. This yields

$$Z_{\mathrm{in},1} = \frac{Z_0 \tanh((\alpha + i\beta) l_\mathrm{res}/2)}{(i\omega C_\mathrm{t} + G_\mathrm{t}) Z_0 \tanh((\alpha + i\beta) l_\mathrm{res}/2) + 1}, \tag{3.5}$$

where α and $\beta = \omega\sqrt{L_l C_l}$ are the real and imaginary part of the propagation constant, respectively. L_l and C_l are the transmission line parameters, i.e. the inductance L_l and the capacitance C_l per unit length.

Next, the second half of the resonator is included as a transmission line of length $l_\mathrm{res}/2$ which is terminated by the load impedance $Z_{\mathrm{in},1}$, yielding the total input impedance (Fig. 3.5(c))

$$Z_\mathrm{in} = Z_0 \frac{Z_{\mathrm{in},1} + Z_0 \tanh((\alpha + i\beta) l_\mathrm{res}/2)}{Z_0 + Z_{\mathrm{in},1} \tanh((\alpha + i\beta) l_\mathrm{res}/2)} \,. \tag{3.6}$$

Substituting $arg = [\alpha + i\beta] l_\mathrm{res}/2$ and performing simplifications, one receives

$$Z_\mathrm{in} = Z_0 \frac{2 \cdot \tanh(arg) + (i\omega C_\mathrm{t} Z_0 + G_\mathrm{t} Z_0) \tanh^2(arg)}{(i\omega C_\mathrm{t} + G_\mathrm{t}) Z_0 \tanh(arg) + 1 + \tanh^2(arg)} \,. \tag{3.7}$$

Using the identity

$$\tanh(a + ib) = \frac{\tanh(a) + i \tan(b)}{1 + i \tanh(a) \tan(b)}, \tag{3.8}$$

and defining $a := \alpha l_\mathrm{res}/2$ and $k := \tan(\beta l_\mathrm{res}/2)$ one can perform approximations of the input impedance Z_in as described in the following.

For the imaginary part $\Im(Z_\mathrm{in})$ of the input impedance Z_in performing a multivariable first-order taylor expansion for the dimensionless parameters $a \approx 10^{-5}$ and $G_\mathrm{t} Z_0 \approx 10^{-4}$ leads to

$$\Im(Z_\mathrm{in}) = -\frac{Z_0(3Z_0\omega C_\mathrm{t} k^2 - Z_0^2 \omega^2 C_\mathrm{t}^2 k^3 - Z_0 \omega C_\mathrm{t} k^4 - 2k + 2k^3)}{1 - 2Z_0\omega C_\mathrm{t} k^2 - 2k^2 + k^4 + 2Z_0 \omega C_\mathrm{t} k^3} + \sigma([a, G_\mathrm{t}]^2), \tag{3.9}$$

The derivation is continued by substituting

$$k = \tan(\beta l_{\mathrm{res}}/2) = \tan(\omega\sqrt{L_l C_l}\, l_{\mathrm{res}}/2) = -1/\tan(\pi\delta\omega/2\omega_0), \tag{3.10}$$

where $\omega = \omega_0 + \delta\omega$ and $\omega_0 = \pi/\sqrt{L_l C_l}\, l_{\mathrm{res}}$ is the resonance frequency without tuning capacitance C_{t}. The part of this derivation defining the precision of the approximation, is performing a multivariable second-order taylor expansion valid for $\omega C_{\mathrm{t}} Z_0 \lesssim 10^{-2}$ and $\delta\omega/\omega_0 \lesssim 10^{-2}$. The imaginary part then reads

$$\Im(Z_{\mathrm{in}}) \approx \frac{Z_0 \pi \delta\omega}{\omega_0} + Z_0^2 \omega C_{\mathrm{t}} + \sigma([a, G_{\mathrm{t}}]^2) + \sigma([\omega C_{\mathrm{t}}, \delta\omega/\omega_0]^3). \tag{3.11}$$

Resonance occurs for $\Im(Z_{\mathrm{in}}) = 0$. Equating to zero and using $Z_0 = \sqrt{L_l/C_l}$ and the resonance frequency without tuning capacitor $\omega_0 = \pi/(\sqrt{L_l C_l}\, l_{\mathrm{res}})$ one finds

$$\omega_{\mathrm{r}} = \frac{\omega_0}{1 + \frac{C_{\mathrm{t}}}{C_l l_{\mathrm{res}}}} = \frac{\omega_0}{1+\gamma} \tag{3.12}$$

for the resonance frequency ω_{r}, where γ is defined as $\gamma = C_{\mathrm{t}}/C_l l_{\mathrm{res}}$.

For further simplifications the product $C_{\mathrm{t}} Z_0$ is described in terms of γ and ω_{r}, which is obtained from

$$\frac{\omega_0 Z_0}{\pi} = \frac{\pi}{\sqrt{L_l C_l}\, l_{\mathrm{res}}} \sqrt{\frac{L_l}{C_l}} \cdot \frac{1}{\pi} = \frac{1}{C_l l_{\mathrm{res}}} \rightarrow \gamma = \frac{C_{\mathrm{t}}}{C_l l_{\mathrm{res}}} = \frac{\omega_0 C_{\mathrm{t}} Z_0}{\pi} \tag{3.13}$$

$$\rightarrow C_{\mathrm{t}} Z_0 = \frac{\pi\gamma}{\omega_0} = \frac{\pi\gamma}{\omega_{\mathrm{r}}(1+\gamma)}\ . \tag{3.14}$$

Then, writing the imaginary part of the input impedance (3.11) as a function of γ and ω_r results in

$$\begin{aligned}
\Im(Z_\mathrm{in}) &\approx Z_0[\frac{\pi\delta\omega}{\omega_0} + \omega C_\mathrm{t} Z_0] = Z_0[\pi\frac{\omega-\omega_0}{\omega_0} + \omega C_\mathrm{t} Z_0] \\
&= Z_0[\pi\frac{\omega-\omega_\mathrm{r}(1+\gamma)}{\omega_\mathrm{r}(1+\gamma)} + \omega C_\mathrm{t} Z_0] \\
&\overset{\omega=\omega_\mathrm{r}+\Delta\omega,(3.14)}{=} Z_0[\pi(\frac{1}{1+\gamma} + \frac{\Delta\omega}{\omega_\mathrm{r}(1+\gamma)} - 1) + (\omega_\mathrm{r}+\Delta\omega)C_\mathrm{t}Z_0] \\
&= Z_0[\pi(\frac{1}{1+\gamma} + \frac{\Delta\omega}{\omega_\mathrm{r}(1+\gamma)} - 1) + (\omega_\mathrm{r}+\Delta\omega)\frac{\pi\gamma}{\omega_\mathrm{r}(1+\gamma)}] \\
&= Z_0[\pi\frac{\Delta\omega}{\omega_\mathrm{r}}\frac{1+\gamma}{1+\gamma} + \pi(\frac{1+\gamma}{1+\gamma} - 1)] \\
&= Z_0\pi\frac{\Delta\omega}{\omega_\mathrm{r}} \ .
\end{aligned} \tag{3.15}$$

Here, $\Delta\omega = \omega - \omega_\mathrm{r}$ is assumed to be a very small value. The last term in Eq. (3.15) is an intermediate result, which will later be used to map the circuit representation of the tunable resonator on an equivalent serial LCR circuit. Before however, an approximate analytical expression for the real part of the input impedance is deduced.

For the real part $\Re(Z_\mathrm{in})$, and correspondingly the loss, the expression of the input impedance Z_in (3.7) is considered and the identity (3.8) is used. For the evaluation of the on resonance ($\omega = \omega_\mathrm{r}$) real part of Z_in, it is advantageous to write both ω_r and $\delta\omega/\omega_0$ as a function of the dimensionless normalized tuning capacitance $\omega_0 C_\mathrm{t} Z_0$.

$$\omega_\mathrm{r} = \frac{\omega_0}{1 + \frac{\omega_0 C_\mathrm{t} Z_0}{\pi}} \ , \tag{3.16}$$

$$\frac{\delta\omega}{\omega_0} = \frac{\omega_\mathrm{r}-\omega_0}{\omega_0} = \frac{1}{\omega_0}\cdot(\frac{\omega_0}{1+\gamma} - \omega_0) = \frac{-\gamma}{1+\gamma} = \frac{-\frac{\omega_0 C_\mathrm{t} Z_0}{\pi}}{1 + \frac{\omega_0 C_\mathrm{t} Z_0}{\pi}} \ . \tag{3.17}$$

Finally, after these substitutions (3.16, 3.17), performing a fourth-order multivariable taylor expansion for a, $G_\mathrm{t}Z_0$ and $\omega_0 C_\mathrm{t} Z_0$ one gets ($a = \alpha l_\mathrm{res}/2$)

$$\begin{aligned}\Re(Z_\mathrm{in}) \approx Z_0 \alpha l_\mathrm{res} \cdot \underbrace{\left(1 - \frac{4}{3}\cdot(\frac{\alpha l_\mathrm{res}}{2})^2\right)}_{S_\mathrm{TL}} \\ + Z_0^2 G_\mathrm{t} \cdot \underbrace{\left(1 - \frac{1}{4}(\omega_0 C_\mathrm{t} Z_0)^2 + \frac{1}{2\pi}\cdot(\omega_0 C_\mathrm{t} Z_0)^3\right)}_{S_\mathrm{t}(C_\mathrm{t})} \\ - 3 G_\mathrm{t} Z_0^2 \cdot (\frac{\alpha l_\mathrm{res}}{2})^2 - G_\mathrm{t}^2 Z_0^3 \frac{\alpha l_\mathrm{res}}{2}.\end{aligned} \tag{3.18}$$

For small values of the variables a, $G_\mathrm{t}Z_0$ and $\omega_0 C_\mathrm{t} Z_0$ the last two terms can be neglected. Furthermore, $S_\mathrm{TL} = 1 = S_\mathrm{t}$ applies well for small values of α and $\omega C_\mathrm{t} Z_0$. Reuniting the approximate expressions for the real and imaginary part of the input impedance, as a first result of the derivation, the input impedance is approximately found as

$$Z_\mathrm{in} \approx Z_0 \alpha l_\mathrm{res} + G_\mathrm{t} Z_0^2 + i Z_0 \pi \frac{\Delta\omega}{\omega_\mathrm{r}}. \tag{3.19}$$

Around resonance, Eq. (3.19) is equivalent to the input impedance Z_{LCR} of a serial LCR resonant circuit [53, 54]

$$Z_{LCR} \approx R + i 2 L \Delta\omega, \tag{3.20}$$

(here, $\Delta\omega = \omega - \omega_{LCR}$, $\omega_{LCR} = 1/\sqrt{LC}$). Thus, a mapping of the tunable device onto the equivalent LCR circuit is possible (Fig. 3.5(d)), which yields the equivalent circuit parameters

$$R = Z_0 \alpha l_\mathrm{res} + G_\mathrm{t} Z_0^2, \tag{3.21}$$

$$L = Z_0 \pi / 2\omega_\mathrm{r}, \tag{3.22}$$

and

$$C = 1/\omega_\mathrm{r}^2 L. \tag{3.23}$$

Following the routine given in [53, 54] one can include effects of the coupling inductances L_c and the coupling to the external measurement circuit with

load impedance Z_0 (Fig. 3.5(e)). By design, the value of the coupling inductances is $L_c = 3.28\,\mathrm{pH}$. The inductive coupling changes both the resonance frequency and the total inductance L_{tot}. However, due to its smallness, the coupling inductance can be neglected in the expressions for the resonance frequency ω_r and the total inductance L_{tot} ($L_c/L \approx 10^{-3}$). Using this assumption, a splitting into internal and external coupling losses is possible (for details see [53]). Hence, one obtains $1/Q_L = 1/Q_i + 1/Q_e$, with

$$Q_e = \frac{Z_0 L}{4\omega_r L_c^2} = \frac{\pi Z_0^2}{4\omega_0^2 L_c^2}(1+\gamma)^2, \tag{3.24}$$

$$Q_i = \frac{\omega_r L}{R} = \frac{\pi}{2(\alpha l_{res} + G_t Z_0)}. \tag{3.25}$$

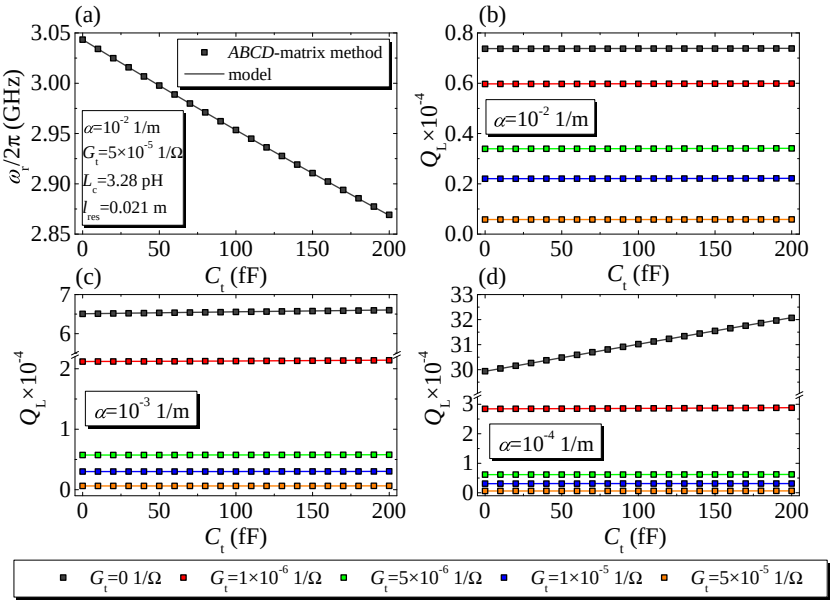

Figure 3.6.: Test of the model: (a) - resonance frequency ω_r vs. tuning capacitance C_t, and (b)-(d) - Q_L vs. C_t, for different values. For all simulations $L_c = 3.28\,\mathrm{pH}$, $l_{res} = 21\,\mathrm{mm}$. Other parameters are marked in the figures. Full squares are simulated values of the *ABCD*-matrix method, solid lines correspond to the model.

In order to compare the approximation to the full circuit, the forward scattering parameter S_{21} of the circuit is calculated via the $ABCD$-matrix method (see Sec. 3.1.1). Performing Lorentzian lineshape fits allows one to compare the extracted values for ω_r and Q_L with the analytical expressions derived above. The comparison is shown in Fig. 3.6, where the resonance frequency and the loaded quality factor are plotted for different values of α and G_t as a function of the tuning capacitance C_t. For the simulated values, no significant change of the resonance frequency with respect to α and G_t is observed (see Eq. (3.16)), and thus ω_r vs. C_t is plotted only for one set of parameters. Depending on the parameters, the relative deviation $\delta x = (x_\mathrm{model} - x_{ABCD})/x_{ABCD}$, where x can be either ω_r or Q_L, is in the worst case (for $\alpha = 10^{-2}\,1/\mathrm{m}$ and $G_\mathrm{t} = 5 \cdot 10^{-5}\,1/\Omega$) on the order of $\delta x = 10^{-3}$.

Combining Eqs. (3.12), (3.24), and (3.25) with simulations of the capacitance network, one can then extract the dielectric function $\varepsilon = \varepsilon_\mathrm{re} - i\varepsilon_\mathrm{im}$ of STO. Therefore, in the following section the capacitance network of the tuning capacitor is analyzed in more detail and the simulation methods are explained.

Capacitance network of the tuning capacitor and simulation

The structure of the tuning capacitor is shown again in Fig. 3.7(a). Note that in Fig. 3.7 metallic layers colored in grey, purple and red correspond to the exact same layer of the fabrication process and that these colors are only introduced for better visibility of the boundary conditions used for the simulations. The picture shows the center conductor (purple) in the middle, surrounded by two ground planes (grey), forming the typical CPW geometry. The ground plane on the right side is interrupted in vertical direction by the dc-bias electrode (red). The dc-bias electrode consists of an interdigitated capacitor (IDC) part, which is located between the center conductor and one of the two ground planes, and a bond pad with an connecting link to the IDC (cf. Fig. 3.4).

Accordingly, for a dc-bias voltage applied to the dc-bias electrode the dc fields and the ac fields of the microwave are partially parallel and partially antiparallel. Note, that the resonator is coupled inductively. Thus, for the dc-bias part of the electric field the center conductor and the ground planes of the structure are on *ground* potential. For the resonant microwave mode, however, the potential between center conductor and ground plane oscillates.

For the ac part of the electric field, this geometry can be modeled with the

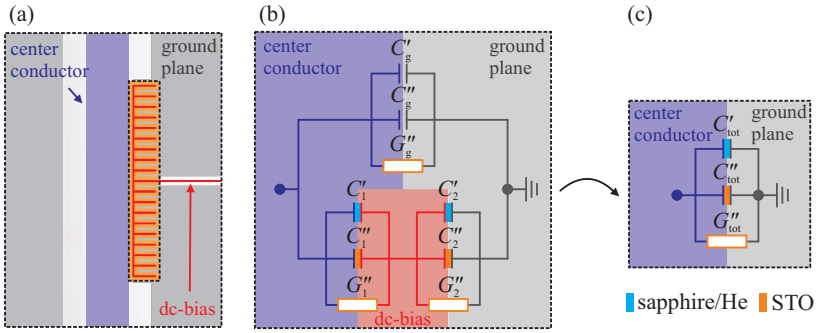

Figure 3.7.: Tuning capacitor and capacitive network. (a) Geometry of tuning capacitor, (b), capacitive network of the tuning capacitor, which can be mapped onto the simplified network drawn in (c).

circuit depicted in Fig. 3.7(b). In general, the capacitive part of the circuit consists of three capacitances, $C_\mathrm{g} = C'_\mathrm{g} + C''_\mathrm{g}$ (center conductor to ground), $C_1 = C'_1 + C''_1$ (center conductor to DC-bias electrode), $C_2 = C'_2 + C''_2$ (DC-bias electrode to ground). Each of those capacitances is separated into a part which is generated by the nonlinear dielectric, denoted by $''$, and another part which is generated by the other dielectrics (sapphire substrate and liquid helium), labeled with $'$. More precisely, for a given voltage U between two conductors, a capacitance C is given by the volume integral of the electric energy density,

$$C = \frac{1}{U^2}\int_V \vec{E}\vec{D}\,\mathrm{d}V = \underbrace{\frac{1}{U^2}\int_{V_\mathrm{STO}} \vec{E}\vec{D}\,\mathrm{d}V}_{C''} + \underbrace{\frac{1}{U^2}\int_{V_\mathrm{rest}} \vec{E}\vec{D}\,\mathrm{d}V}_{C'}, \tag{3.26}$$

which can be divided into an integral over the volume V_STO of the nonlinear dielectric, and the volume V_rest of the remaining part of the geometry. Here, $\vec{E}$ and $\vec{D}$ denote the electric field and electric displacement field, respectively. This separation is necessary for the model, due to the fact that the dielectric loss of both the sapphire substrate ($\tan\delta < 10^{-6}$) and the liquid helium surrounding the sample ($\tan\delta < 10^{-5}$) can be neglected. Thus, the loss added by the tuning capacitor can approximately be assumed to be generated only

by the electric power dissipated by the nonlinear dielectric. This dielectric loss is modeled with the conductances G''_{g}, G''_1 and G''_2, which also depend on the volume integral of the electric energy density (assuming a uniform dielectric function), such that one can write

$$G''_{\mathrm{g}} = \omega C''_{\mathrm{g}} \tan\delta, \quad G''_1 = \omega C''_1 \tan\delta, \quad G''_2 = \omega C''_2 \tan\delta, \tag{3.27}$$

where $\tan\delta = \varepsilon_{\mathrm{im}}/\varepsilon_{\mathrm{re}}$. Note, that in these expressions for the conductances the loss tangent is the same for G''_{g}, G''_1 and G''_2. This circuit can be mapped on a simplified circuit, consisting of a capacitance $C_{\mathrm{tot}} = C'_{\mathrm{tot}} + C''_{\mathrm{tot}}$ in parallel with a conductance G''_{tot} between center conductor and ground plane (Fig. 3.7(c)). Assuming moderate loss tangents (cf. Sec. 2.3.2, $\tan\delta \approx 10^{-2}$) of the nonlinear dielectric, one finds approximately

$$\begin{aligned} C_{\mathrm{tot}} &= C'_{\mathrm{tot}} + C''_{\mathrm{tot}} = \frac{C_1 C_2}{C_1 + C_2} + C_{\mathrm{g}}, \\ G_{\mathrm{tot}} &= G''_{\mathrm{tot}} = \omega \underbrace{\left[\frac{C''_1 C_2 + C_1 C''_2}{C_1 + C_2} + C''_{\mathrm{g}} \right]}_{C''_{\mathrm{tot}}} \tan\delta = \omega C''_{\mathrm{tot}} \tan\delta. \end{aligned} \tag{3.28}$$

The physical meaning of the approximation is given by the fact that phase shifts due to oscillating currents in the conductances are neglected. The software COMSOL Multiphysics is used to simulate the capacitance of the device. Results are presented in Fig. 3.8. By setting the boundary conditions of the center conductor as *terminal*, the ground planes as *ground*, and the DC-bias electrode as *floating potential* with zero charge, the mapping on the simplified circuit is performed automatically. More precisely, the simulation is performed for several values of the real part $\varepsilon_{\mathrm{re}}$ of the dielectric function. The solver calculates the electric fields of the geometry and thus can evaluate the corresponding capacitance using a similar expression as the first one in Eq. (3.26). The results of this simulation of the capacitance C_{tot} as a function of the dielectric constant $\varepsilon_{\mathrm{re}}$ are shown in Fig. 3.8(a). The axes in the plot are exchanged, since from the measurement one obtains the capacitance, and thus the linear fit of the simulation results can be used to extract $\varepsilon_{\mathrm{re}}$. In addition, with these simulations of the electric fields, integrals of the electric energy density over both the volume of the nonlinear dielectric and the remaining geometry can be calculated (Eq. (3.26)). Comparing these integrals

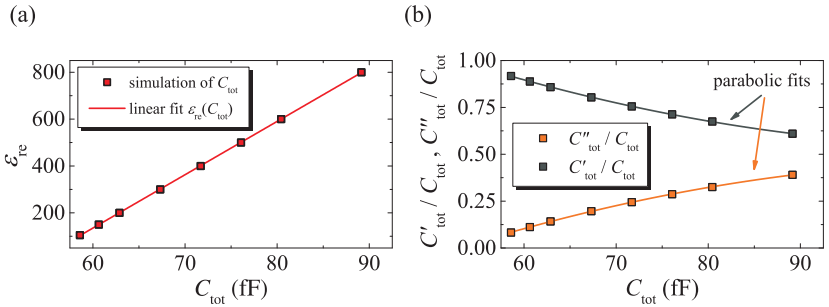

Figure 3.8.: Simulation results of the capacitance network. (a) the real part of the dielectric function ε_{re} as a function of the capacitance C_{tot}. (b) ratios C''_{tot}/C_{tot} (orange) and C'_{tot}/C_{tot} (grey). Data in (a) are fitted with a linear function, data in (b) with a parabolic function.

to the total electric energy, one gets the fraction of the capacitance that dissipates energy, C''_{tot}/C_{tot}, which is plotted as orange squares in Fig. 3.8(b). The grey squares indicate C'_{tot}/C_{tot}. Note that $C''_{tot}/C_{tot} + C'_{tot}/C_{tot} = 1$.

The simulations of the capacitance C_{tot} are performed for a finite piece of transmission line with a length of $l_{TL} = 500\,\mu$m. The capacitance C_t used in the model, however only accounts for the tuning capacitance. Accordingly, the capacitance $C_{TL,noC}$ of a regular transmission line with the same length l_{TL} has to be subtracted. Simulating the transmission line capacitance yields $C_{TL,noC} = 44\,$fF. Thus, for the correct calculation of the dielectric function one has to use $C_{tot} = C_t + C_{TL,noC}$.

The simulation method described above can then be used to calculate the expected resonance frequency of a resonator with the tuning capacitor, but without added nonlinear dielectric. Therefore, the model predicts $\omega_{r,noSTO,sim} = 3.035\,$GHz, whereas the measured resonance frequency is found as $\omega_{r,noSTO} = 3.0343\,$GHz. This can be related to neglecting the connecting link of the dc-bias electrode and the precision of the finite element simulation with COMSOL. Comparing $\omega_{r,noSTO,sim}$ and $\omega_{r,noSTO}$ with $\omega_0 = 3.044\,$GHz and using the expression of the resonance frequency (Eq. (3.12)), the error of the extracted capacitance C_{tot} and the related dielectric function can be estimated to be on the order of $< 10\,\%$.

3.1.4. Experimental data

Virgin sweep

For the transmission measurements, the sample is mounted into a brass box. The ground planes of the sample are electrically connected to the brass box with silver paste. On both sides the signal line is connected to SMA connectors with Indium. Wire bonds, starting at the bond pad, are used to connect the dc-bias electrode to the external dc voltage supply (see Fig. 3.4(a)).

The sample is cooled down to a temperature of $T = 4.2\,\mathrm{K}$ in liquid helium and a dc voltage U is applied to the bias electrode. For each voltage a transmission spectrum is measured and the data are fitted with a Lorentzian to get the resonance frequency ω_r and the loaded quality factor Q_L. For an input power of $P_\mathrm{in} = -25\,\mathrm{dBm}$ the results are shown in Fig. 3.9.

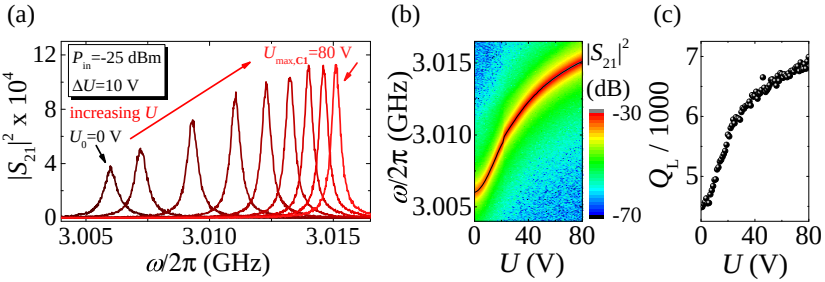

Figure 3.9.: Measurement results. (a) Transmitted power for voltages from 0 V up to 80 V in steps of $\Delta U = 10\,\mathrm{V}$, and (b) transmitted power as a function of frequency ω and voltage U. Black solid line in (b) indicates the resonance frequency ω_r, black circles in (c) show the loaded quality factor Q_L, both extracted from the measured data with a Lorentzian fit.

For this sample the resonance frequency $\omega_\mathrm{r}/2\pi$ can be tuned within $3.006\,\mathrm{GHz} - 3.015\,\mathrm{GHz}$ for a voltage between $0\,\mathrm{V} - 80\,\mathrm{V}$. More precisely, the resonance frequency increases with increasing dc voltage, and tends to saturate for high dc voltages. This effect can be understood by the close relation between the real part of the dielectric function ε_re and the slope of the nonlinear polarization curve P ($\varepsilon_\mathrm{re} = \varepsilon_0^{-1} dP/dE + 1$).

As the slope of the polarization curve, and hence ε_re and C_t, decreases for higher electric fields values and goes into saturation, the resonance frequency

is raised and goes into saturation as well. Furthermore, it is found that both the loaded quality factor Q_L as well as the transmission maximum on resonance to be enhanced at higher dc voltages. The quality factor varies within $4500 - 7000$.

Using the combination of model and simulation described above one can extract the complex dielectric function of the nonlinear dielectric. Therefore, the tunable resonator is compared to a resonator with the same meandered design, but without tuning capacitor. Such resonators typically had a resonance frequency of $\omega_r/2\pi = 3.044\,\mathrm{GHz}$ and a quality factor of about ≈ 12000.

For the real part ε_{re}, Eq. (3.12) is used to calculate the value of the tuning capacitance C_t, corresponding to the resonance frequency change compared to a resonator without tuning capacitor. As described above (Sec. 3.1.3), the software COMSOL Multiphysics is used to simulate C_t for different values of the dielectric constant ε_{re}. Finally, the results of the simulations and the measurements are compared. This comparison enables the calculation of ε_{re}. The result is shown in Fig. 3.10 (blue dots). The zero voltage dielectric constant is $\varepsilon_{re,0V} = 725$. With increasing voltage, ε_{re} is reduced corresponding to the increasing resonance frequency. The values vary between $\varepsilon_{re} = 725$ and 500 for voltages between 0 and 80 V. Similar results have been demonstrated for $SrTio_3$ thin films also grown by means of pulsed laser deposition [110, 111].

For the imaginary part $-\varepsilon_{im}$ of the dielectric function, or more common, the loss tangent $\tan\delta$ of the nonlinear dielectric, first the losses caused by the input-output coupling ($L_c = 3.28\,\mathrm{pH}$) are subtracted using $1/Q_i = 1/Q_L - 1/Q_e$, in order to receive the internal quality factor Q_i of the tunable resonator. The loss factors due to the tuning capacitor $2G_tZ_0/\pi$ are obtained to be about $2 \cdot 10^{-4}$ for 0 V, and $6 \cdot 10^{-5}$ for 80 V. The internal transmission line loss is found as $1/Q_{i,TL} \approx 8 \cdot 10^{-5}$ and the loss due to the coupling to the input-output circuitry can be calculated as $1/Q_e \approx 2 \cdot 10^{-6}$. Thus, the presence of the lossy nonlinear dielectric significantly reduces the loaded quality factor Q_L. Referring to the results of the simulations shown in Sec. 3.1.3, the fraction of the capacitance which introduces loss can then be used to calculate the loss tangent of the nonlinear dielectric. The values of the losses as a function of the applied voltage are shown in Fig. 3.10 (red dots). At zero voltage, the loss tangent is $\tan\delta_{0V} = 11.3 \cdot 10^{-3}$. With increasing voltage the dielectric loss is reduced, corresponding to the enhanced quality factors. In addition to the values for the real part of the dielectric function, also these values agree very well with literature values [110, 111].

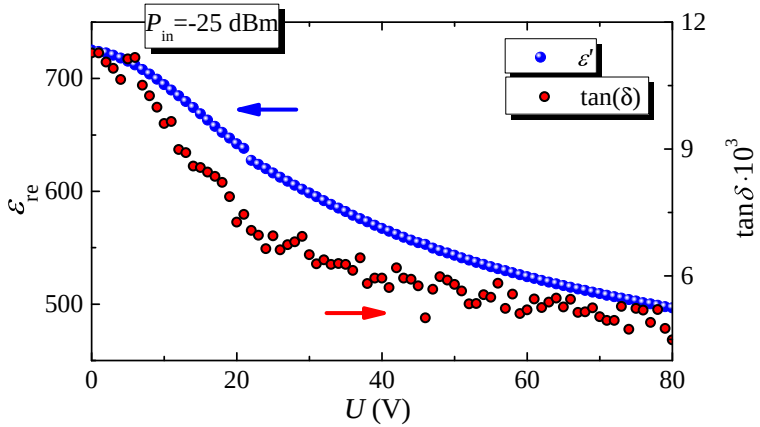

Figure 3.10.: Extracted values for ε_{re} (blue dots) and loss factor $\tan\delta$ (red circles) as a function of the applied DC voltage, with an input power of $P_{in} = -25\,\mathrm{dBm}$. Inset shows loaded quality factors Q_L.

Behavior in magnetic fields

Next, the behavior of the resonator in magnetic fields in out-of-plane configuration is briefly discussed. For the measurements a certain dc voltage U is applied at a temperature above the critical temperature $T_c = 9.2\,\mathrm{K}$, then the sample is cooled down to 4.2 K and finally a full hysteresis sweep of the magnetic field up to a maximum of 2 mT is performed. The magnetic field is generated via a pair of Helmholtz coils. Results are shown in Fig. 3.11. With increasing magnetic field the transmission maximum is reduced and shifted towards smaller frequencies, indicating a reduction of the quality factor and the resonance frequency. A detailed description of magnetic-field-induced losses and frequency shifts, and approaches for a reduction of these losses, are given in [50–52]. Mainly, there are two effects contributing to the frequency shifts. First, the circulating Meissner currents change the kinetic inductance of the superconductor. This non-hysteretic effect results in the decrease of the resonance frequency with increasing magnetic field B. Second, the presence of Abrikosov vortices adds a hysteretic component, if the vortices are pinned to intrinsic defects in the superconductor. In Fig. 3.11(b) the magnetic hysteresis loops for voltages from 0 to 80 V in

steps of 20 V are shown. The frequency shifts due to the nonlinear dielectric tuning overtop the magnetically induced frequency changes. Thus, one can compensate for magnetic-field-induced frequency shifts and tune the resonance frequency to a desired value. Finally, the loss factor of a resonator is

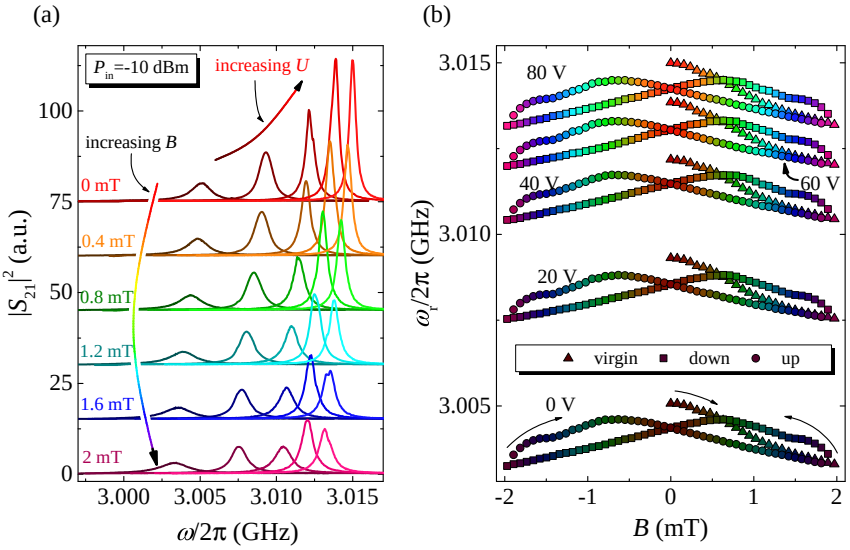

Figure 3.11.: Magnetic field characterization. (a) transmission measurements of the virgin sweep for different voltages and magnetic fields. (b) magnetic field hysteresis loops of the resonance frequency, for different voltages between 0 and 80 V in steps of 20 V. For $U = 0$, the arrows indicate the sweep direction.

estimated whose capacitor is designed such, that the tuning of the resonance frequency equals the frequency shift in a magnetic field of $B = 1\,\mathrm{mT}$, which is $\delta\omega_{\mathrm{r},1\,\mathrm{mT}}/2\pi = 1\,\mathrm{MHz}$. For the capacitor presented in this paper, the tunability for a voltage up to 80 V was $\delta\omega_{\mathrm{r}}/2\pi = 10\,\mathrm{MHz}$. From Eq. (3.12) one finds that one tenth of the tuning capacitance of the resonator would have been sufficient to compensate the field-induced shift. This would reduce the dielectric loss by the same factor. Accordingly, for such a resonator, the conventional transmission line loss would be the dominant loss mechanism.

Hysteresis effects induced by the nonlinear dielectric

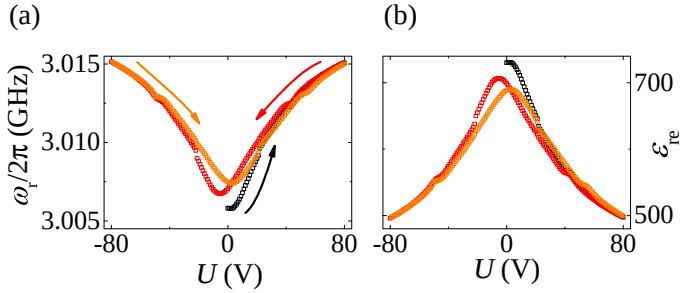

Figure 3.12.: Hysteresis of the applied dc-voltage. Hysteretic behavior of the resonance frequency ω_r (a) and the real part of the dielectric function ε_{re} (b).

Next, measurements of a full hysteresis sweep of the dc voltage are shown (see Fig. 3.12). It is found that for high voltages the resonance frequencies saturate at almost the same frequency for each sweep. After changing the sweep direction, however, the minimum resonance frequency is observed to be increased compared to the previous sweep. In addition, the minimum resonance frequencies during the up- and downsweep occur for different voltages $U_{\mathrm{down}} = -5.5\,\mathrm{V}$ and $U_{\mathrm{up}} = 3\,\mathrm{V}$. A similar asymmetry for the electric field polarity was observed in [112] and attributed to the presence of oxygen vacancies, whose concentration can be increased for negative voltages. For the thin films, these effects also lead to the strong reduction of the real part of the dielectric response compared to bulk material, i.e. substrates.

Such a hysteresis is found for all of the samples containing a nonlinear capacitor fabricated during the thesis (see Appendix B in Sec. B). These effects limit the usefulness of these resonators. For a hybrid quantum system operated at a temperature of about 4 K, such resonators would have to be heated up to a temperature of about 40 K to return to the virgin state of the nonlinear dielectric in order to use the full tunability. On the other hand, for this sample, sweeping the voltage back and forth reduces the tunability of the device from 10 MHz to about 7 MHz. Thus, the device can be used at high voltages at which the resonance frequencies are approximately the same for each sweep (cf. Fig. 3.12).

Nonlinear effects

So far, the tuning capacitor was described as a linear lumped device for the microwave mode, and nonlinear effects were neglected, such as a power dependent shift of the resonance frequency. For each voltage between 0 and 80 V the input power is varied from −40 dBm to 0 dBm and the transmission curves of the resonant device (Fig. 3.13(a) - $U = 0\,\mathrm{V}$, (b) - $U = 80\,\mathrm{V}$) is measured. One observes a reduction of the on-resonance transmission coefficient $|S_{21}|$ with increasing input power, which is more pronounced for small voltages. Simultaneously, curves with strongly reduced on-resonance transmission also display a slight downward shift of the resonance frequency, indicating a nonlinearity of the system. The power dependence of the resonance frequencies and loaded quality factors are shown in Fig. 3.13(c), (d). The dependence of the resonance frequency on the input power P_{in} is rather weak. A close look, however, shows, that for constant voltage the resonance frequency slightly decreases with increasing input power P_{in} (Fig. 3.13(e)). For a comparison of the resonator properties at different voltages, the relative frequency shift is defined for each voltage as

$$\delta\omega_{\mathrm{r,rel},U} = \frac{\omega_{\mathrm{r,LP},U} - \omega_{\mathrm{r}}(P_{\mathrm{in}})}{\omega_{\mathrm{r,LP},U}}, \tag{3.29}$$

where $\omega_{\mathrm{r,LP},U}$ is the resonance frequency at low input powers. For small voltages, relative frequency shifts up to $\approx 10^{-4}$ are observed. For higher voltages, however, the frequency shifts are one order of magnitude smaller. In contrast to these small changes of the resonance frequency, the input power dependence of the loaded quality factor is more pronounced. For each voltage, a significant drop of the loaded quality factor with increasing input power can be found. By calculating

$$\Delta Q_{\mathrm{L,rel}} = \frac{Q_{\mathrm{L}}}{Q_{\mathrm{L,LP},U}} \tag{3.30}$$

one finds that for small voltages the quality factor is reduced to 60 % of the low power quality factor $Q_{\mathrm{L,LP},U}$, whereas for higher voltages the reduction of the quality factor is less than 10 %. It is found that both the relative shift of the resonance frequency $\delta\omega_{\mathrm{r,rel},U}$ and the drop of the quality factor $\Delta Q_{\mathrm{L,rel}}$ have their maximum for $U = 0\,\mathrm{V}$.

The power dependence of the dielectric properties of STO has been studied in theory [113] and experiment [112]. The model of the nonlinear dielectric,

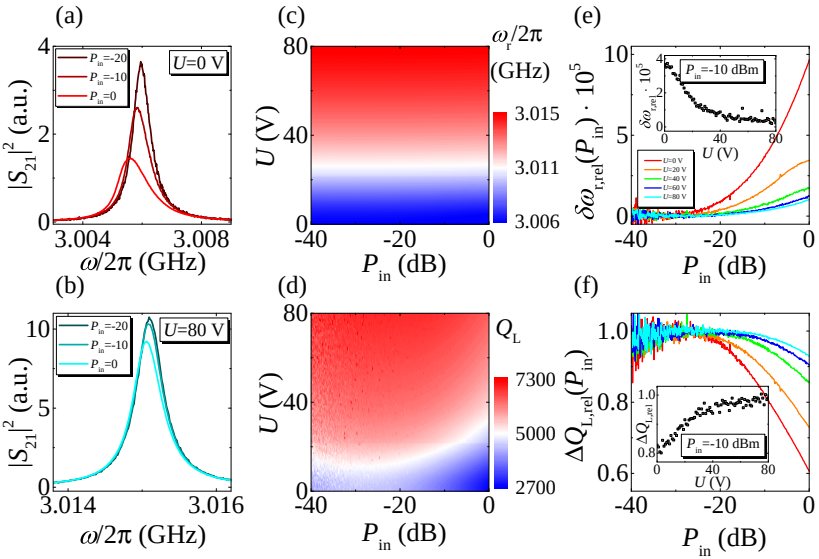

Figure 3.13.: Nonlinear effects. (a), (b) show transmission curves with varying input power for $U = 0\,\mathrm{V}$ and $U = 80\,\mathrm{V}$, respectively. (c) and (d) depict the fitted resonance frequency ω_r and the loaded quality factor Q_L as a function of the input power P_in. (e) and (d) display the relative frequency shift $\delta\omega_\mathrm{r,rel}$ and the relative shift of the quality factor $\delta Q_\mathrm{L,rel}$ for voltages within $0 - 80\,\mathrm{V}$, both compared to the saturation level at small input powers. Insets show the voltage dependence, exemplarily calculated at $P_\mathrm{in} = -10\,\mathrm{dBm}$.

where one assumes a considerable periodic shift of the nonlinear polarization induced by the oscillating voltage across the capacitance, would (at least for zero dc voltage) result in a reduced time-averaged real and imaginary part of the dielectric function ϵ_avg. Hence, in this picture, both the resonance frequency and the quality factor would increase as a function of power, which is in contradiction with the measurements. Thus, it might be that for high input powers, the piezoelectric nature of STO becomes relevant [114]. Accordingly, the lowered resonance frequencies and quality factors would be related to the coupling to phonon modes and corresponding mechanical motion losses (which is one of the loss mechanisms of perovskite oxides). However, the measurements performed for this work do not result in a clear picture describing the observed nonlinearity.

3.2. Tuning CPW resonators by temperature

Another option of tuning the resonance frequency is varying the temperature T of the sample. At least at temperatures above $T/T_c \approx 0.5$ the kinetic inductance of the sample has a significant dependence on temperature, enabling tuning. The resonator presented throughout this section is the resonator used to study the resonant (to the hyperfine splitting) and non-resonant magnetic coupling of the microwave magnetic field of the resonator to an ultracold cloud of ^{87}Rb atoms [45].

These resonators were developed in several works in our group [49, 60, 115]. The resonator design was developed by D. Bothner, H. Hattermann, D. Wiedmaier and me [49, 60, 115]. D. Bothner furthermore fabricated the sample. The test measurements in brass boxes were performed by myself, whereas the measurements in the actual setup for the investigation of the coupling were performed together with L. Y. Ley. The discussion of the temperature and magnetic field dependence was done by D. Bothner and myself. D. Bothner, H. Hattermann and myself performed and discussed the simulation of the magnetic coupling.

3.2.1. Fabrication and sample design

The fabrication process used for the atom chip is presented in Fig. 3.14. For the fabrication a two-layer process is used, starting with a 500 nm thick layer of niobium deposited by magnetron sputtering (Fig. 3.14(a)). The niobium parts are structured by means of optical lithography (Fig. 3.14(b)) and reactive ion etching with SF_6 (Fig. 3.14(c)). The second layer, a Ti/Au bilayer, is structured using a liftoff process, accordingly starting with optical lithography (Fig. 3.14(d)). The normal conducting Ti/Au parts have an overlap of $O = 10\,\mu$m with the superconducting Nb parts. In order to reduce contact resistances between the layers, the niobium parts are etched with SF_6 in the overlap region prior to the deposition of the second layer (Fig. 3.14(d)). The latter consists of a 5 nm thick sticking layer of titanium and a 400 nm thick layer of magnetron sputtered gold (Fig. 3.14(e)). The second layer is finalized using a liftoff in warm acetone (Fig. 3.14(f)). The CPW has a center conductor width of $S = 30\,\mu$m and a gap between the center conductor and the ground planes of $W = 16\,\mu$m.

The integrated design combines a Z-shaped superconducting niobium trapping wire [48] and an inductively coupled superconducting CPW half-

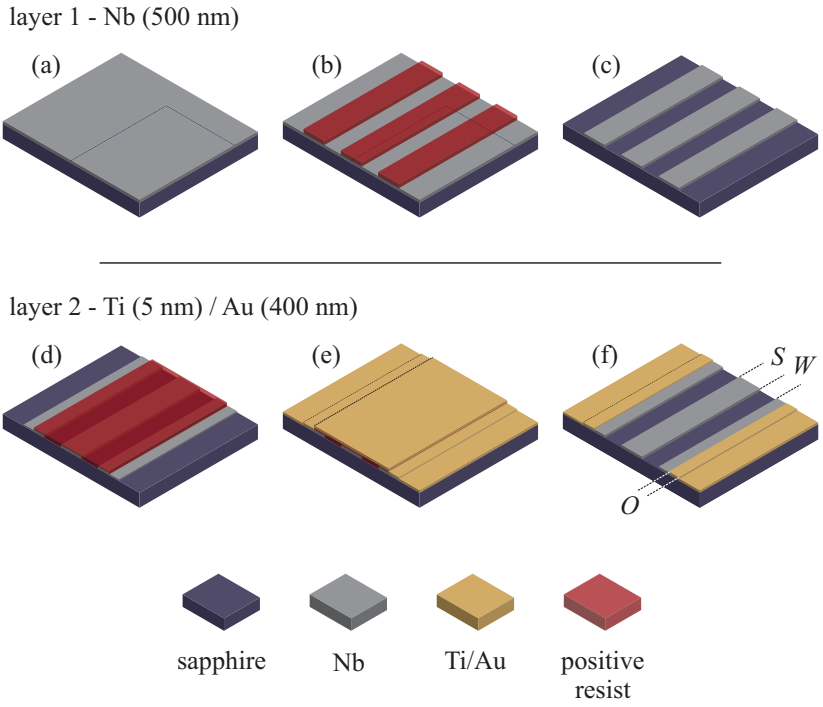

Figure 3.14.: Fabrication steps of the atoms chip. Layer 1 - 500 nm niobium deposited by magnetron sputtering (a), structured using optical lithography (positive resist) (b) and reactive ion etching with SF_6, resulting in (c). Layer 2 - liftoff process starting with optical lithography (positive resist), etching with SF_6 and electron beam evaporation of 5 nm sticking layer of titanium, (d), and 400 nm of gold (e). (f) Liftoff in warm aceton to finalize chip fabrication. $S = 30\,\mu$m, $W = 16\,\mu$m and overlap $O = 10\,\mu$m represent cross-sectional dimensions.

wavelength resonator (cf. Fig. 3.15(a)). The combination of a current of about 1 A biased through the Z-wire and a homogeneous magnetic bias field applied in y-direction allows for trapping the cold atom cloud above one of the CPW gaps at a distance of about $20\,\mu$m (see Fig. 3.15(b)). Parts of the superconducting ground planes are replaced by gold in order to reduce field focusing effects into the gaps between center conductor and TL due to the Meissner effect. The normal conducting ground plane extensions ena-

ble proper grounding conditions, thereby preventing parasitic transmission [52, 116]. The properties of such inductively coupled resonators with normal conducting ground plane extensions are known to be extremely stable in magnetic fields in out-of-plane direction on the order of some mT [52].

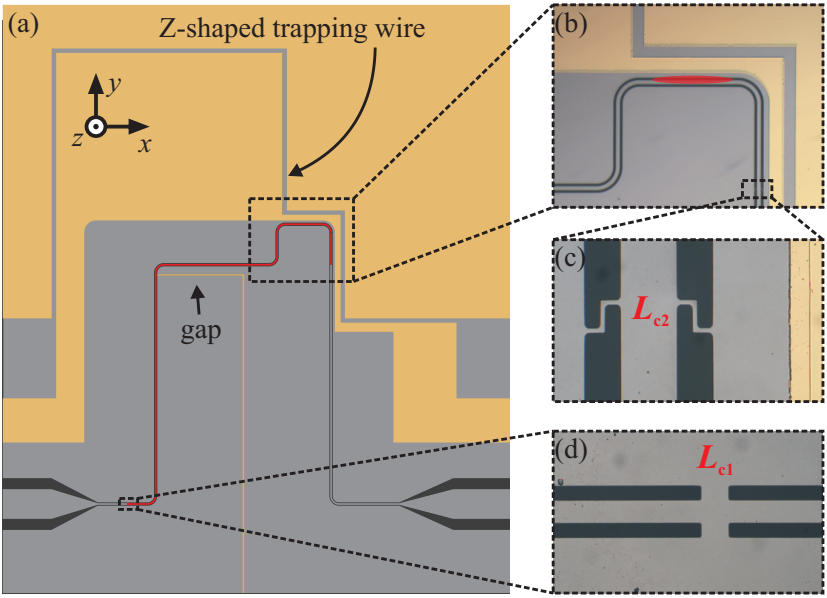

Figure 3.15.: Atom chip design. (a) Top view of the integrated atom chip, containing a Z-shaped niobium trapping wire and a superconducting resonator (center conductor part colored in red). Parts of the superconducting ground planes are replaced by gold, normal conducting gold *slit* in bottom ground plane prevents the formation of a closed superconducting loop. (b)-(d) Optical images of trapping region (red ellipse illustrates trapped atom cloud), output and input coupling inductances, respectively.

The TL representation of the resonator is shown in Fig. 2.4(b) of Sec. 2.1.3. The resonator is formed by a TL with a characteristic impedance Z_0 and attenuation constant α. Two shorts to ground (L_{c1} and L_{c2}) terminate the TL at two sides, forming an inductively coupled half-wavelength CPW resonator. The equivalent lumped circuit of the device can be seen in Fig. 2.4(c) (cf. Sec. 2.1.3). The corresponding capacitance C and inductance L can be calculated using the expressions in Eq. (2.27), whereas the resistor R ac-

counts for internal TL losses due to the attenuation constant α [53]. The inductive shorts between center conductor and ground planes of the TL are respectively shown in Fig. 3.15(c) and (d) for the output and the input port. The equivalent circuit inductances L_{c1} and L_{c2} corresponding to both ports are the parallel combinations of the individual shorts, revealing $L_{c1} = 6.44\,\mathrm{pH}$ and $L_{c2} = 1.47\,\mathrm{pH}$. The external linewidth κ_e and quality factor Q_e due to the inductive coupling to the input-output-circuit are given by

$$\kappa_e = \omega_r \frac{\pi}{2} \frac{L_{c1}^2 + L_{c2}^2}{L^2} = 2\pi \cdot (134 + 7)\,\mathrm{kHz} \rightarrow Q_e = \frac{\omega_r}{\kappa_e} = 5 \cdot 10^4 \ . \qquad (3.31)$$

3.2.2. Temperature dependence

Tuning the resonance frequency by changing the temperature is related to a change of the kinetic inductance per unit length L_k as a function of temperature. Analytical expressions for CPWs and related geometries have been found [70, 117–120]. These expressions depend on the film thickness t, the temperature dependent London penetration $\lambda_L(T)$ and the cross-sectional dimensions of the waveguide. In most of the above mentioned references, however, closed analytical expressions usable for performing best fits to experimental data are found either in the limit of thick ($t \gg 2\lambda_L$, $L_k \propto \lambda_L$) or thin ($t \ll 2\lambda_L$, $L_k \propto \lambda_L^2$) superconducting films. However, for the superconducting film thickness of $t = 500\,\mathrm{nm}$ of the sample and the temperature range of the measurements $0.4 < T/T_c < 1$, the ratio between film thickness and magnetic penetration depth is found to be $t/2\lambda_L \approx 1$. Accordingly, the following discussion is restricted to a closed expression in [118] allowing such a fit procedure (cf. Sec. 2.2.1).

The cross sectional dimensions of the CPW are shown in Fig.2.2. In the experiments the dimensions are given by $W = 30\,\mu\mathrm{m}$, $S = 16\,\mu\mathrm{m}$, $t = 500\,\mathrm{nm}$, and $h = 330\,\mu\mathrm{m}$. Using the replacement $d = W + 2S$, according

to [118] the geometrical and kinetic inductance per unit length are given by (cf. also Sec. 2.1.2)

$$\begin{aligned} L_\mathrm{g} &= \frac{\mu_0}{4} \cdot \frac{K(k')}{K(k)}, \\ L_\mathrm{k}(T) &= \mu_0 \lambda_\mathrm{L}(T) \frac{C}{4ADK(k)} \left(\frac{1.7}{\sinh[t/(2\lambda_\mathrm{L}(T))]} \right. \\ &\quad \left. + \frac{0.4}{\sqrt{[(B/A)^2 - 1] \cdot [1 - (B/D)^2]}} \right), \end{aligned} \tag{3.32}$$

where

$$\begin{aligned} A &= -\frac{t}{\pi} + \frac{1}{2}\sqrt{\left(\frac{2t}{\pi}\right)^2 + W^2} \\ B &= \frac{W^2}{4A} \\ C &= B - \frac{t}{\pi} + \sqrt{\left(\frac{t}{\pi}\right)^2 + \frac{1}{4}(d-W)^2} \\ D &= \frac{2t}{\pi} + C. \end{aligned} \tag{3.33}$$

$K(k)$ and $K(k')$ are the complete elliptic integrals of the first kind with the modules $k = w/d$ and $k' = \sqrt{1-k^2}$. Therefore, the resonance frequency $\omega_\mathrm{r}(T)$ as a function of the temperature T can be expressed in terms of these inductances.

$$\omega_\mathrm{r}(T) = \omega_\mathrm{r}(T=0)\sqrt{\frac{L_\mathrm{g} + L_\mathrm{k}(T)}{L_\mathrm{g} + L_\mathrm{k}(T=0)}}\ . \tag{3.34}$$

As can be seen in Eqs.(3.32), (3.34), the temperature dependence of the resonance frequency originates only from the temperature dependence of $\lambda_\mathrm{L}(T)$. The temperature dependence of the penetration depth for a BCS superconductor can be captured by

$$\lambda_\mathrm{L}(T) = \frac{\lambda_\mathrm{L}(T=0)}{\sqrt{1 - (\frac{T}{T_\mathrm{c}})^4}}\ , \tag{3.35}$$

where T_c is the critical temperature of the superconductor. Accordingly, the $\omega_\mathrm{r}(T)$ dependence is described completely by the resonance frequency

and the penetration depth at zero temperature, $\omega_r(T=0)$ and $\lambda_L(T=0)$, respectively, thus serving as fit parameters, as well as by $T_{c,Nb} = 9.2\,\mathrm{K}$. In the experimental setup the temperature sensor is positioned inside the coldfinger of the flow cryostat, whereas the superconducting atom chip is located at a distance of roughly 10 cm to the sensor. Thus, it is most likely to have a temperature offset ΔT between sample and sensor, which is taken into account as an additional fit parameter by setting the sample temperature T as $T = T_{sensor} + \Delta T$.

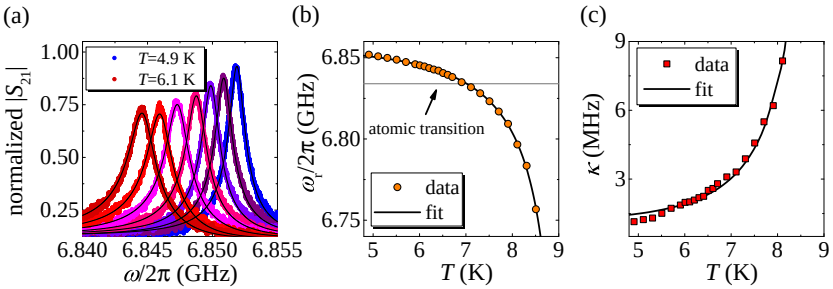

Figure 3.16.: Temperature dependence of the resonator properties. (a) Forward transmission amplitude $|S_{21}(\omega)|$ for temperatures from 4.9 K to 6.1 K in steps of 0.2 K with fits (black solid lines) using Eq. (3.36), (b) and (c) respectively show the temperature dependence of the resonance frequency ω_r and the linewidth $\kappa = \omega_r/Q_L$ (data and fits). Grey solid line corresponds to atomic transition at $\omega_a = 2\pi \cdot 6.834\,\mathrm{GHz}$.

Figure 3.16(a) shows the amplitude of the microwave transmission measurements $|S_{21}(\omega)|$ for temperatures $4.9\,\mathrm{K} < T < 6.1\,\mathrm{K}$ performed in the setup with best fits using a modified asymmetric Lorentzian [121]

$$|S_{21}(\omega)| = \left| \frac{a}{1 + 2iQ_L(\omega - \omega_r)/\omega_r} + Ae^{i\phi} \right| , \tag{3.36}$$

where $Ae^{i\phi}$ accounts for an additional parasitic transmission of a wave which does not show signs of a resonance in the measured frequency range, i.e. the phase ϕ can be assumed as constant. The temperature dependence of both the resonance frequency ω_r and the resonator linewidth $\kappa = \omega_r/Q_L$ is shown in Fig. 3.16(b), (c), respectively. A best fit for $\omega_r(T)$ using Eq. (3.34) is added for the fit parameters $\omega_r(T=0) = 6.855\,\mathrm{GHz}$, $\lambda_L(T=0) = 181\,\mathrm{nm}$

and an offset temperature $\Delta T = 0.91\,\mathrm{K}$[2]. At a temperature of about 7 K the resonator is on resonance with the atomic hyperfine transition frequency of $\omega_\mathrm{a} = 2\pi \cdot 6.834\,\mathrm{GHz}$. The obtained penetration depth seems to be relatively large compared to typical values of about 100 nm for niobium.

For the linewidth κ of the resonator transmission $|S_{21}(\omega)|$ a simple description based on the two-fluid model for the superconductor and a temperature independent linewidth for the normal conductor can be used to fit the data. The surface resistance R_s of superconductor at a frequency ω is given by

$$R_\mathrm{s} = \frac{1}{2}\mu_0^2\omega^2\sigma_1\lambda_\mathrm{L}^3 \ , \tag{3.37}$$

where μ_0 is the vacuum permeability and $\sigma_1 \propto n_\mathrm{n}/n_\mathrm{e} = (T/T_\mathrm{c})^4$ is the real part of the complex conductivity with the quasi-particle density n_n normalized to the electron density n_e. Due to the small relative changes of 10^{-2} of the resonance frequency, the frequency dependence of R_s is neglected in the following. In combination with the temperature dependence $\lambda_\mathrm{L}(T)$ and using $R_\mathrm{s} \propto \kappa$ one can fit the data using

$$\kappa = \kappa_0 + \kappa_1 \left(\frac{T}{T_\mathrm{c}}\right)^4 \cdot \left(1 - \left(\frac{T}{T_\mathrm{c}}\right)^4\right)^{-3/2} \ , \tag{3.38}$$

where κ_0 and κ_1 are fit parameters. While κ_1 accounts for the losses in the superconducting parts, κ_0 captures the residual losses due to currents running in the normal conductor. Note that for the normal conducting parts no temperature dependence was considered due to the Debye temperature of about $\Theta_\mathrm{D} = 175\,\mathrm{K}$ for gold and the correspondingly small reduced temperature T/Θ_D. Data and fit of the linewidth are shown in Fig. 3.16(c) for the best fit parameters $\kappa_0 = 1.2\,\mathrm{MHz}$ and $\kappa_1 = 2.97\,\mathrm{MHz}$. For temperatures below 5.7 K the fit does not describe the dependence of the loss properly, however, at temperatures relevant for the experiments in [45] (around 7 K, i.e. where $\omega_\mathrm{r} \approx \omega_\mathrm{a}$) the temperature dependence of the loss is captured quite well.

Even though the CPW resonator design makes use of normal conductors, the kinetic energy term is dominated by the superconducting parts, since $L_\mathrm{kin} \propto \int j^2 dS$, where the integration is over the cross section S of the CPW.

[2] Best fits were also performed using the expressions given in [119, 120], showing similar results for the penetration depth

At the location of the normal conducting parts, which are separated by about 40 μm from the inner edge of the ground conductor, the sheet current density j has already decreased significantly.

3.2.3. Behavior under biasing conditions

Next, the behavior of the resonator properties in out-of-plane magnetic fields up to 0.3 mT and currents through the Z-shaped trapping wire up to 0.4 A is shown, necessary for trapping the atoms above one of the gaps between center conductor and ground planes. The magnetic field characterization was performed at temperatures of 6.0 K (see Fig. 3.17(a)-(c)) and at 6.6 K (see Fig. 3.17(d)-(f)), i.e. when the resonator is almost on resonance with the atomic transition. Assuming the superconducting parts to be in the Meissner state, the model used to describe the temperature dependence of the resonance frequency can be extended to include the magnetic field dependence by using the nonlinear London equations. The London penetration depth can then be written as

$$\lambda_{\mathrm{L}}(T,B) = \frac{\lambda_{\mathrm{L}}(T,B=0)}{1-\beta B^2}\ , \tag{3.39}$$

where β depends on temperature and describes the degree of the nonlinearity. Using

$$\omega_{\mathrm{r}}(T,B) = \omega_{\mathrm{r}}(T,B=0)\sqrt{\frac{L_{\mathrm{g}}+L_{\mathrm{k}}(T,B)}{L_{\mathrm{g}}+L_{\mathrm{k}}(T,B=0)}} \tag{3.40}$$

for the resonance frequency one can perform best fits to the magnetic field dependence solely using β as a fit parameter, which is shown as solid lines in Fig. 3.17(b) and (e). One finds $\beta_{6.0\,\mathrm{K}} = 0.11\,(\mathrm{mT})^{-2}$ and $\beta_{6.6\,\mathrm{K}} = 0.19\,(\mathrm{mT})^{-2}$. The relative frequency shifts are of order 10^{-4}.

In addition, also the the model for the loss can be extended such that, based on the analysis of the resonance frequency, predictions of the overall losses are possible. The solid lines in Fig. 3.17(c) and (f), however, despite showing a similarity in trend, do not describe the losses properly. It seems most likely that a small number of vortices is present causing additional losses. It is known [50] that in addition to causing losses, the presence of vortices add a hysteretic component due to pinning of vortices to intrinsic defects in the superconductor. However, the temperature control is not stable enough to make such effects visible. The magnetic field induced loss factors

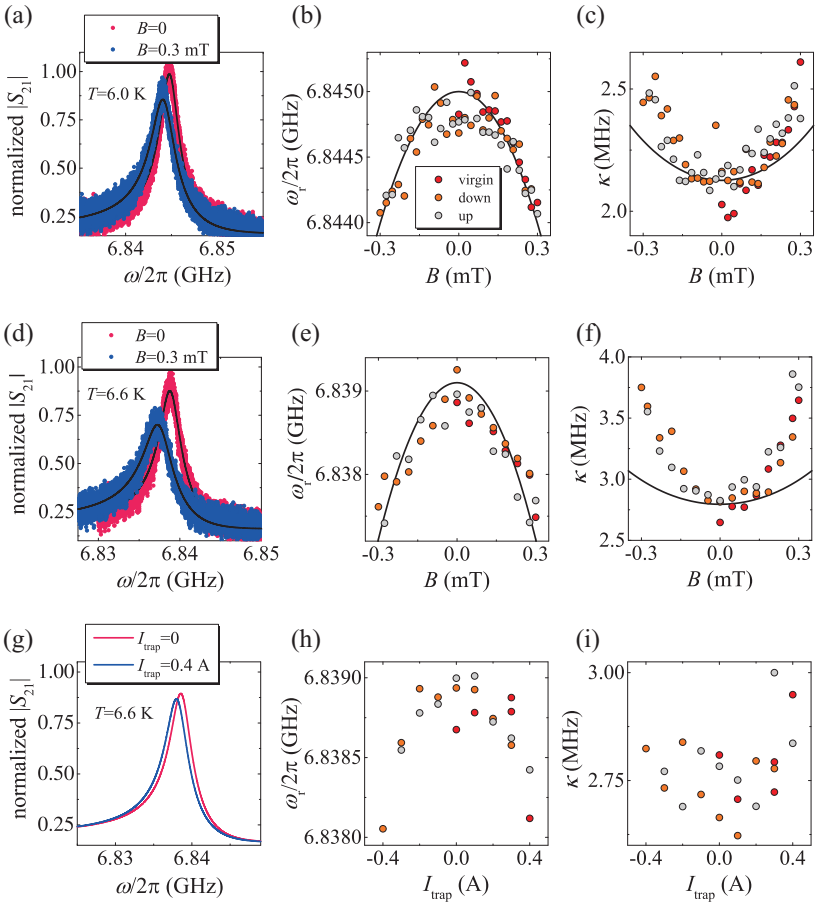

Figure 3.17.: Resonator properties as a function of trapping conditions. (a)-(c) Forward transmission amplitude $|S_{21}(\omega)|$ for $B = 0$ to $B = 0.3\,\mathrm{mT}$, hysteresis of both resonance frequency $\omega_\mathrm{r}(B)$ and $\kappa(B)$ for $T = 6.0\,\mathrm{K}$. (d)-(f) Same as (a)-(c) but for $T = 6.6\,\mathrm{K}$. (g)-(i) Forward transmission amplitude $|S_{21}(\omega)|$ for $I_\mathrm{trap} = 0$ to $I_\mathrm{trap} = 0.4\,\mathrm{A}$, hysteresis of both resonance frequency $\omega_\mathrm{r}(I_\mathrm{trap})$ and $\kappa(I_\mathrm{trap})$ for $T = 6.6\,\mathrm{K}$. Data in (a) and (d) are fitted using Eq. (3.36). In (g) only fits are shown for clarity.

$1/Q_B = 1/Q_\mathrm{L}(B = 0.3\,\mathrm{mT}) - 1/Q_\mathrm{L}(B = 0)$ for these two temperatures are $1/Q_{B,6.0\,\mathrm{K}} = 0.7 \cdot 10^{-4}$ and $1/Q_{B,6.6\,\mathrm{K}} = 1.7 \cdot 10^{-4}$, respectively.

Finally, at a temperature of $T = 6.6\,\mathrm{K}$, the behavior of the resonator with a current applied to the Z-shaped trapping wire is analyzed. The magnetic field generated by the current running close to the resonator structure (cf. Fig. 3.15) penetrates the gaps between center conductor and ground plane, thereby causing Meissner currents and a shift of the kinetic inductance. More precisely, the upper gap is magnetically shielded by the superconducting loop surrounding the gap. Accordingly, frequency shifts (due to any magnetic field) are mainly introduced by the Meissner currents at the lower edge of the center conductor and the lower ground plane. The relative frequency shifts at currents up to 0.4 A are about 10^{-4}. The current induced loss factor is $1/Q_{I,6.6\,\mathrm{K}} = 0.5 \cdot 10^{-4}$.

3.2.4. Coupling between resonator and atomic cloud

As the final part of this section, simulations of the coupling between the $\lambda/2$ mode of the resonator and the ultracold atomic ensemble are shown. The simulations were preformed using 3D-MLSI [68]. The single photon coupling can be estimated using the current amplitude of the standing wave pattern

$$I(l) = I_0 \cos\left(2\pi \frac{l}{\lambda}\right) \ , \tag{3.41}$$

where I_0 is the current amplitude at the antinodes. The current vacuum fluctuations I corresponding to the residual energy of an empty cavity can be calculated via

$$\frac{1}{2}\hbar\omega_\mathrm{r}^2 = \int_0^{\lambda/2} L_\mathrm{g} I \cos^2\left(2\pi \frac{l}{\lambda}\right) dl = \frac{\lambda}{4} L_\mathrm{g} I^2 \ . \tag{3.42}$$

Due to its smallness, the kinetic part is neglected for the calculation of the coupling. Using the geometric inductance of $L_\mathrm{g} = 409\,\mathrm{nH/m}$, one finds $I = 33.5\,\mathrm{nA}$ for the current amplitude of the vacuum fluctuations at an antinode. Note, that at the position of the atoms, the current amplitude has reduced to about $0.95 \cdot I$. The coupling is shown in Fig. 3.18 using

$$g = \frac{|B_\mathrm{MW}| \cdot |\mu|}{\hbar} \ , \tag{3.43}$$

where $|B_\mathrm{MW}|$ is the simulated amplitude of the microwave magnetic field in the cross-section and $|\mu|$ is the magnetic moment of the atoms. The

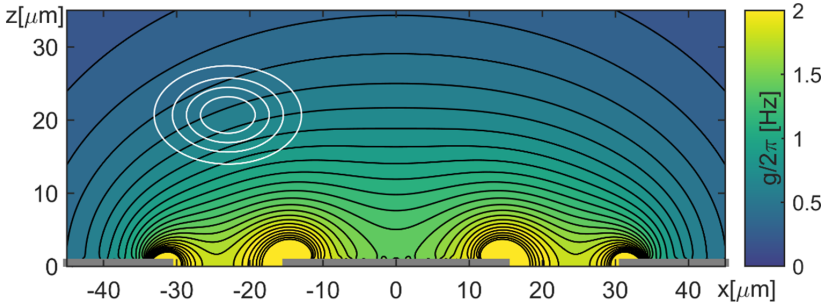

Figure 3.18.: Coupling between a single photon stored in the resonator and an atom in the magnetic ground state. White lines indicate extension of the atomic cloud in the magnetic trap. (adopted from [45])

simulations show that the single-spin to single-photon coupling is roughly $g = 0.5\,\mathrm{Hz}$. Thus, quality factors of about 10^8 or more are required to get close to the desired regime of strong coupling.

3.2.5. Atom chip with nonlinear dielectric

Atom chips are also available with tunable resonators containing a nonlinear capacitor, with $SrTiO_3$ as a nonlinear dielectric. In contrast to the atom chip shown before (cf. Fig. 3.15), the gap in the bottom ground plane is replaced by a dc-bias electrode for applying the voltage to the nonlinear capacitor Fig. 3.19(c). The transmission measurements and the extracted resonance frequencies ω_r can be seen in Fig. 3.19(d), (e). The tunability of the device was 50 MHz. However, the resonance frequency could not be adjusted to the atomic transition. However, with minor adjustment of the physical length of the resonators, resonant conditions can be achieved. Atom chips with nonlinear dielectric tuning are usable in a hybrid quantum system at a temperature of 4 K.

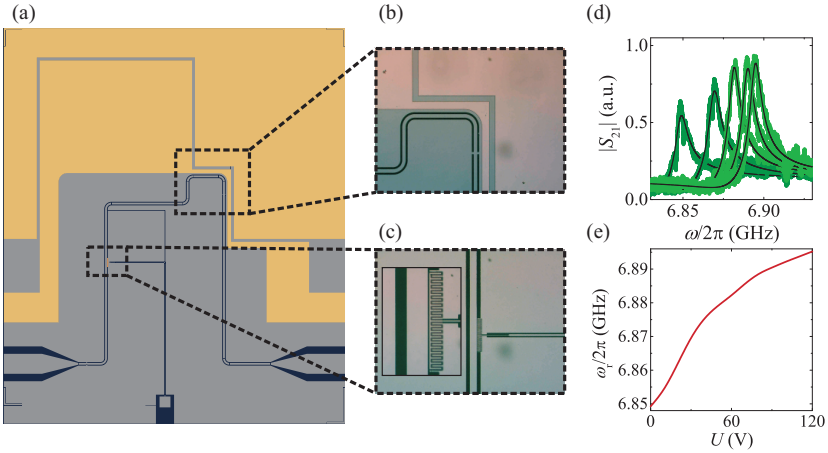

Figure 3.19.: Atom chip with nonlinear dielectric. (a) Layout, (b), (c) optical images of the trapping region of the atoms and the nonlinear capacitor with $SrTiO_3$ as nonlinear dielectric (inset shown zoom). (d) Transmission $|S_{21}(\omega)|$ for different voltages from 0 to 120 V in steps of 30 V with best fits using Eq. (3.36), (e) extracted resonance frequencies. Loaded quality factors were $Q_L \approx 1000$ (not shown).

4 Lumped element resonators

4.1. Design considerations

Lumped element (LE) resonators have gained increasing interest since they can be used to increase the magnetic coupling to spin-systems by designing the resonators to have a low impedance, or to increase the electric coupling using high resonator impedances [122–126]. Such resonators are discussed in the following. During the thesis, three different designs were considered. One of these designs is analyzed in detail in the following, the other two are shown in Fig. 4.1. The first approach shows a LE resonator embedded in a TL, cf. Fig. 4.1(a), (b). The closed superconducting loop formed by the ground plane surrounding the resonator protects the resonator by means of flux conservation. In magnetic fields oriented along the out-of-plane direction the relative frequency shifts were on the order of some 10^{-5} in magnetic fields up to 2.5 mT.

One further LE resonator is formed by interrupting a CPW TL with two lumped capacitors, which are connected via an inductor. On each end the device has two shorts to the ground planes, accordingly forming a closed superconducting loop. Consequently, similarly as in [53], the device can be used to generate a persistent current trap. The inductor of the resonator is protected from magnetic field changes by means of flux conservation. The corresponding relative frequency shifts were 10^{-4} in magnetic fields in out-of-plane configuration up to 10 mT. The main results of the magnetic field characteristics can be found in the Bachelor thesis [127]. In the following, the third approach is considered in more detail.

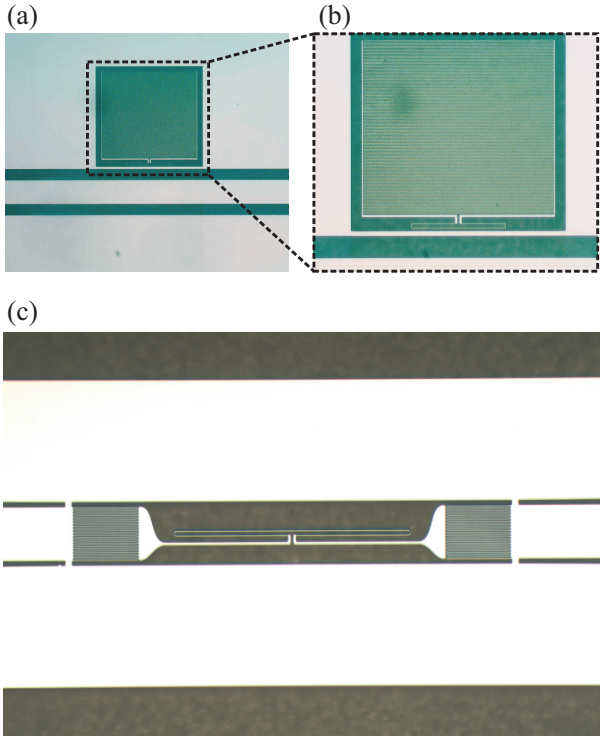

Figure 4.1.: LE resonator designs. Optical images of (a) an overview and (b) a zoomed version of a LE resonator embedded in a ground plane of a TL, and (c), LE resonator interrupting the center conductor of the TL.

4.2. Tunable stacked two-chip design[1]

The LE resonators presented in the preceding section can also be used for experiments at mK-temperatures. However, they have one disadvantage, namely they are not frequency tunable. Thus, either a nonlinear capacitor, similar to the one used for the tunable CPW resonators in Sec. 2.1.3 with STO, or a nonlinear inductor using a Josephson junction [128–130] has to be implemented into the resonator structure. However, adding such a nonlinear element leads to a significant reduction of the internal quality factors. Thus, one aim of this thesis was to fabricate devices which are frequency tunable without introducing additional loss due to the tuning. The resulting device is presented in this section. First, a circuit model of the device is established and simulations of the circuit parameters are used to predict the behavior of the device. Then, the application of the device in hybrid quantum systems is discussed in detail.

4.2.1. Fabrication and sample design

The device consists of two parts, the TL for excitation and readout, and the lumped element (LE) resonator. Each of these two elements is fabricated on a separate Sapphire substrate. For the experiment, the LE-chip is mounted on top of the TL-chip (see Fig. 4.2(a)). The fabrication processes of both chips in general follow the same routine, starting with the deposition of a 500 nm thick layer of superconducting Niobium (Nb, $T_{c,\mathrm{Nb}} = 9.2\,\mathrm{K}$), deposited by magnetron sputtering on a r-cut sapphire substrate with a thickness of $h_{\mathrm{TL}} = 330\,\mu\mathrm{m}$ for the TL, and $h_{\mathrm{LE}} = 100\,\mu\mathrm{m}$ for the LE resonator (see Fig. 4.2). For the resonator chip, a double-sided polished substrate is used to facilitate alignment and a visual position determination during the chip stacking process. After an optical lithography step, the structures are etched by means of reactive ion etching with SF_6. A schematic of the two-chip device is shown in Fig. 4.2(a). The TL has a typical coplanar waveguide (CPW) geometry with finite width ground planes. More precisely, the TL

[1] Parts of this chapter are contained in the submitted manuscript: B. Ferdinand, D. Bothner, R. Kleiner, D. Koelle, "Tunable superconducting two-chip lumped element resonator". Own contributions: For this publication I designed, fabricated and measured the samples. I further wrote a software for both the measurements and the analysis of the measurements. I performed the simulations of the circuit parameters and calculated the model. I analyzed all results, including the simulations and the measurements and wrote the first draft of the manuscript.

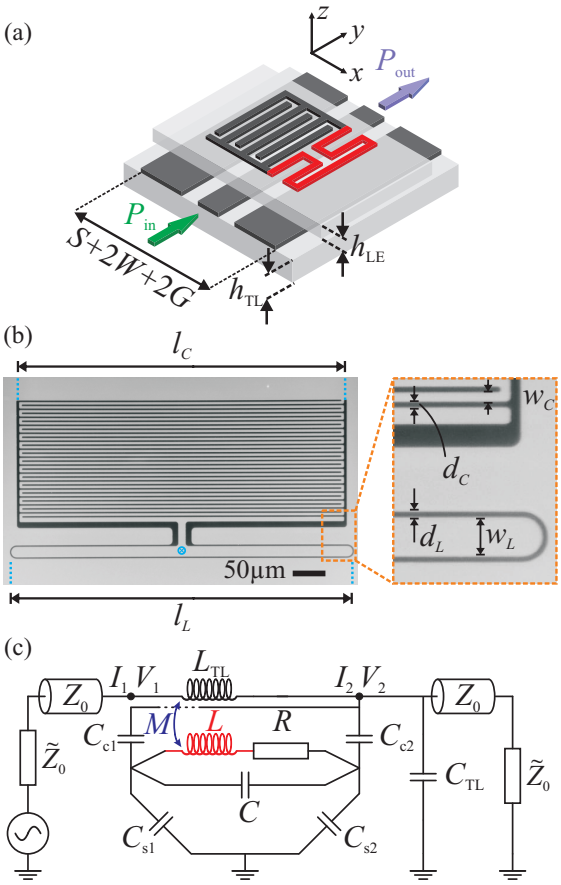

Figure 4.2.: Device and equivalent circuit. (a) Schematic view of the experimental setup with the LE-chip mounted on top of the TL-chip. Dark grey parts on the top chip indicate the capacitor, red parts show the inductive loop of the circuit. (b) Optical image of a LE resonator (here: $l_C = 500\,\mu$m, $l_L = 530\,\mu$m), the blue circle indicates the center of the loop. The zoomed version shows a section of the cigar shaped inductor and of the interdigital capacitor. (c) Circuit representation of the lumped device (for details see text).

has a center conductor width of $S = 200\,\mu$m, a gap between the center conductor and the ground planes of $W = 90\,\mu$m and a width of the ground

planes of $G = 400\,\mu$m. The LE resonators consist of an interdigitated capacitor (IDC, dark grey in Fig. 4.2(a)) in parallel with an inductive loop (red in Fig. 4.2(a)). The capacitor has $N = 30$ fingers with a length of $l_C = 500\,\mu$m. The width of the fingers is $d_C = 2.4\,\mu$m and the gap between neighboring fingers is $\Delta d = 3.6\,\mu$m. The inductive loop has two parts: first, the cigar shaped main part with a length of $l_L = 530\,\mu$m, a loop width $w_L = 15\,\mu$m and a conductor width of $d_L = 2.4\,\mu$m, and the connection to the IDC. For an adequate description, however, the inductance of the capacitor fingers has also to be taken into account. An optical image of the resonator part can be seen in Fig. 4.2(b).

Due to the double-sided polished substrate, the LE-chip can be moved in x-direction without scratching the Nb thin film of the TL. Below it will be shown that moving the resonator can be used to tune both the resonance frequency and the coupling to the TL. In particular, one can place the LE-chip at a "dark position", i.e. at a position where no coupling to the TL can be observed.

4.2.2. Model

Figure 4.2 (c) shows the LE circuit which is used to model the lumped device. The circuit consists of the LE resonator, represented by the inductor L and the capacitor C. The part of the TL along the resonator is modeled by the inductor L_{TL} and the capacitor C_{TL}, which can be understood as the inductance (capacitance) per unit length L_l (C_l) integrated along the LE resonator, such that $\sqrt{L_{\mathrm{TL}}/C_{\mathrm{TL}}}$ is the corresponding characteristic TL impedance. For regions outside the overlap with the LE resonator, but still below the LE substrate, the characteristic impedance of the TL is given by $Z_0 = 41\,\Omega$. The remaining parts of the TL and the connection to a network analyzer have an impedance of $\tilde{Z}_0 = 50\,\Omega$. Several capacitors are used to account for the frequency shifts, induced by the presence of the TL (C_{c1}, C_{c2} - center conductor of the TL to resonator; C_{s1}, C_{s2} - resonator to ground). Due to the symmetry of the sample, $C_{\mathrm{c1}} = C_{\mathrm{c2}} =: C_{\mathrm{c}}$, $C_{\mathrm{s1}} = C_{\mathrm{s2}} =: C_{\mathrm{s}}$ is assumed in the following, resulting in a vanishing capacitive coupling between LE resonator and TL. The coupling to the TL, which is thus purely inductive, is mediated via a mutual inductance M. At a temperature of $T = 4.2\,\mathrm{K}$, resistive losses are dominant, which is taken into account via a resistance R in series with the inductor L.

Solving Kirchhoff equations (without the capacitor C_{TL} and the impedance $\tilde{Z}_0$)) for the circuit shown in Fig. 4.2(c) leads to

$$
\begin{aligned}
V_2 = \frac{1}{i\omega C_{\mathrm{c}}}\Bigg\{ & \frac{V_1 - V_2 + i\omega M I_{L,R}}{i\omega L_{\mathrm{TL}}} - I_2 - \frac{1}{2}\Bigg\{ \frac{V_1 - V_2 + i\omega M I_{L,R}}{i\omega L_{\mathrm{TL}}} - I_2 \\
& + [(i\omega L + R) I_{L,R} - i\omega M \frac{V_1 - V_2 + i\omega M I_{L,R}}{i\omega L_{\mathrm{TL}}}] \cdot i\omega C_{\mathrm{c}} \Bigg\} \Bigg\} \\
& + (i\omega L + R) I_{L,R} - i\omega M I_1 + \frac{1}{i\omega C_{\mathrm{s}}}\Bigg\{ \frac{1}{2} \frac{V_1 - V_2 + i\omega M I_{L,R}}{i\omega L_{\mathrm{TL}}} - I_2 \\
& + [(i\omega L + R) I_{L,R} - i\omega M \frac{V_1 - V_2 + i\omega M I_{L,R}}{i\omega L_{\mathrm{TL}}}] \cdot i\omega C_{\mathrm{c}} \Bigg\} \Bigg\} \\
& + I_{L,R} + [(i\omega L + R) I_{L,R} - i\omega M \frac{V_1 - V_2 + i\omega M I_{L,R}}{i\omega L_{\mathrm{TL}}}] \cdot i\omega C,
\end{aligned}
$$

$$
I_1 = \frac{V_1 - V_2 + i\omega M I_{L,R}}{i\omega L_{\mathrm{TL}}},
$$

$$
I_{L,R} = \frac{i\omega M[(V_2 - V_1) \cdot (2C + C_{\mathrm{c}} + C_{\mathrm{s}})]}{-2L_{\mathrm{TL}} - i\omega L_{\mathrm{TL}} R(2C + C_{\mathrm{c}} + C_{\mathrm{s}}) + \omega^2 (L L_{\mathrm{TL}} - M^2) \cdot (2C + C_{\mathrm{c}} + C_{\mathrm{s}})}. \tag{4.1}
$$

Using these expressions (4.1), one can evaluate the matrix elements of the $ABCD$ matrix $\hat{S}_{\mathrm{LE}}$ of the LE resonator via

$$
\begin{pmatrix} V_1 \\ I_1 \end{pmatrix} = \begin{pmatrix} A & B \\ C & D \end{pmatrix} \begin{pmatrix} V_2 \\ I_2 \end{pmatrix} = \hat{S}_{\mathrm{LE}} \begin{pmatrix} V_2 \\ I_2 \end{pmatrix}. \tag{4.2}
$$

Multiplying this matrix with the $ABCD$ matrix

$$
\hat{S}_{C\mathrm{TL}} = \begin{pmatrix} 1 & 0 \\ i\omega C_{\mathrm{TL}} & 1 \end{pmatrix} \tag{4.3}
$$

of the capacitor C_{TL}, one gets the total $ABCD$ matrix of the circuit, and hence, the transmission S-parameter $S_{21}(\omega)$ by using [54]

$$
S_{21} = \frac{2}{A + B/Z_0 + C Z_0 + D}. \tag{4.4}
$$

Equation (4.4) will in the following be referred to as the exact solution of the transmission function S_{21}, since up to this point no approximations have been made. The uncoupled resonance frequency is $\omega_\mathrm{u} = (\sqrt{LC})^{-1} = 2\pi \cdot 5.98\,\mathrm{GHz}$ ($L = 1129\,\mathrm{pH}$, $C = 626\,\mathrm{fF}$). However, due to the presence of the superconducting surfaces of the TL, the frequency is shifted significantly. In order to get analytical expressions for the resonance frequency and the quality factors, approximations are made in the following. By assuming a high internal quality factor $Q_\mathrm{i} > 10^3$, and consequently a small resistance R of the resonator, one can expect little influence of the resistance on the resonance frequency. Thus, the resonance frequency ω_r of the resonator can be calculated using $R = 0$, which leads to the form

$$S_{21,R=0} = \frac{a_0 + a_2\omega^2}{\sum_{j=1}^{4} b_j \omega^j} \ . \tag{4.5}$$

Introducing the dimensionless parameters,

$$\mu = \frac{M}{L}, \quad \lambda = \frac{L_\mathrm{TL}}{L}, \quad \gamma_\mathrm{c} = \frac{C_\mathrm{c}}{C}, \quad \gamma_\mathrm{s} = \frac{C_\mathrm{s}}{C}, \quad \gamma_\mathrm{TL} = \frac{C_\mathrm{TL}}{C}, \quad \zeta = \frac{\sqrt{L/C}}{Z_0}, \tag{4.6}$$

and defining $\gamma = \gamma_\mathrm{c} + \gamma_\mathrm{s}$, one obtains two solutions by equating the numerator of the transmission function to zero, one of which is the negative of the other. The solution for $\omega_\mathrm{r} > 0$ is shifted towards smaller values, compared to the uncoupled resonance frequency $\omega_\mathrm{u} = 1/\sqrt{LC}$. The resonance frequency in absence of internal losses is found as

$$\omega_\mathrm{r} = \frac{2\omega_\mathrm{u}}{\sqrt{2\gamma + 4}} \ . \tag{4.7}$$

According to Eq. (4.7), the resonance frequency depends only on the coupling capacitances C_c and C_s, or more precisely, on the sum of these capacitances, which will later turn out to be almost constant when the position x is varied with respect to the TL. Thus, the frequency changes are barely induced by these capacitances.

For the implementation of internal losses into the model, one can transform $i\omega L \to i\omega L + R$, or equivalently, the inductance L to

$$L \to L + \frac{R}{i\omega} = L(1 - iq), \tag{4.8}$$

where the definition of the internal quality factor Q_i of this LCR circuit (cf. Eq. (2.12))

$$q = \frac{1}{Q_\mathrm{i}} = \frac{R}{\omega_\mathrm{r} L} \tag{4.9}$$

is inserted. In Eq. (4.9) it is assumed that the system is considered only close to resonance ($\omega \approx \omega_\mathrm{r}$).

Expanding the derived expression for the forward transmission S_{21} around ω_r up to the linear order in $\Delta\omega = \omega - \omega_\mathrm{r}$ for both the numerator and the denominator, one finds as an approximation, analogous to [131],

$$S_{21}(\omega) = A e^{i\phi} \frac{1 + 2iQ_\mathrm{i}\frac{\Delta\omega}{\omega_\mathrm{r}}}{1 + \frac{Q_\mathrm{i}}{Q_\mathrm{e}} + i\frac{Q_\mathrm{i}}{Q_\mathrm{a}} + 2iQ_\mathrm{i}\frac{\Delta\omega}{\omega_\mathrm{r}}} \ , \tag{4.10}$$

where A and ϕ respectively are an amplitude and phase offset, ω_r is the resonance frequency and Q_e and Q_i are the external and internal quality factor. The dimensionless parameter Q_a accounts for an asymmetric lineshape of the transmission function $S_{21}(\omega)$ around resonance. Performing a multivariable Taylor expansion for both the numerator and the denominator separately in orders of μ, γ_c and γ_s one approximately gets

$$Q_\mathrm{e} \approx \frac{\gamma_\mathrm{TL}^2 + 4\zeta^2 - 2\gamma_\mathrm{TL}\lambda\zeta^2 + \zeta^4\lambda^2 + \zeta^2\gamma_\mathrm{TL}^2\lambda^2}{(2\zeta^2 + \gamma_\mathrm{TL}^2)\zeta\mu^2} \tag{4.11}$$

as an analytic expression for the external quality factor Q_e. For the asymmetry parameter one finds

$$Q_\mathrm{a} \approx \frac{\gamma_\mathrm{TL}^2 + 4\zeta^2 - 2\gamma_\mathrm{TL}\lambda\zeta^2 + \zeta^4\lambda^2 + \zeta^2\gamma_\mathrm{TL}^2\lambda^2}{(\gamma_\mathrm{TL} - \gamma_\mathrm{TL}^2\lambda - \zeta^2\lambda)\zeta^2\mu^2} \ . \tag{4.12}$$

In the model, the impedance $\tilde{Z}_0 = 50\,\Omega$ is neglected and the transmission function is calculated using the impedance Z_0 in Eq. (4.4). Thus, the calculated transmission function and the corresponding external quality factors can be seen as measured next to the resonator structure. Using $\tilde{Z}_0$ instead of Z_0 reduces the calculated external quality factors Q_e to $\approx 85\%$.

4.2.3. Simulation of the circuit parameters

For the simulation of the inductive part of the circuit the finite element software 3D-MLSI is used [68]. Based on the London and the Maxwell equations,

this software enables the simulation of circuits in 2.5 dimensions, meaning that the boundary conditions are applied at the edges of a two-dimensional structure (x- and y-direction), and in the remaining z-direction, effects of the generated magnetic fields and the corresponding inductances and mutual inductances are taken into account using the Biot-Savart law. A schematic of the circuit is drawn in Fig. 4.3(a), with an enlarged version in (b) focusing on the LE resonator. The figure illustrates the boundary conditions for current paths used to simulate the inductance matrix. The currents in the TL are defined to flow from the left hand side of the center conductor (port 1 (TL)), across the inductive shorts (grey dashed frames) to the left hand side of the ground planes (port 2 (TL)). Of course, these shorts are not present in the real TL structure, however, including them this way for the simu-

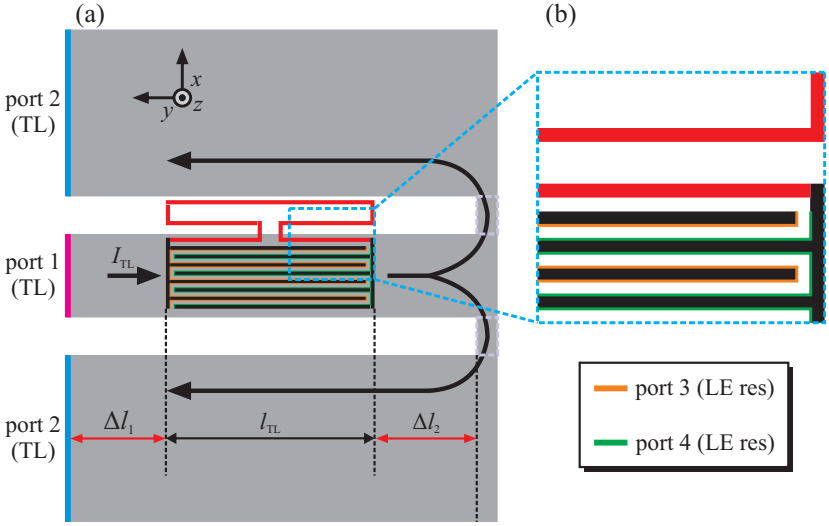

Figure 4.3.: Schematic of the boundary conditions used to calculate the inductance matrix numerically. The whole geometry is shown in (a), consisting of the TL part (grey) and the LE resonator with the inductive loop (red) and the IDC (black). For the simulation of the inductance matrix, the TL current I_{TL} (direction indicated by the black arrows) flow from port 1 to port 2, whereas the currents of the LE resonator go from port 3 to port 4. The grey dashed rectangle frames inductive shorts from the center conductor of the TL to the ground planes. Panel (b) shows an enlarged picture of the IDC in order to make the choice of boundary conditions for the currents of the LE resonator more clear.

lations automatically maps both, the inductance of the ground planes and the mutual inductance between center conductor and ground plane, onto the TL inductance, as typical for the description in the framework of TL theory [54]. The distance $\Delta l_2 = 250\,\mu$m between the right end of the LE resonator and the shorts is chosen as a compromise, such that, on the one hand, no significant amount of flux generated by the currents along these shorts is threading the inductive loop of the LE resonator, and on the other hand, the mesh is small enough to be able to simulate the structure. In addition, the inductance of the shorts does not change the TL inductance by much. Based on the simulations it is found that the presence of the LE resonator does not affect the inductance of the TL. Hence, the simulated value of the TL can easily be adjusted to the correct length of the LE resonator along the TL in order to get L_{TL}.

The capacitance matrix is calculated using COMSOL Multiphysics, which offers the possibility of a full 3D simulation. For the simulation, only the IDC part of the LE resonator (black in Fig. 4.3) is taken into account and the inductive loop structure is absent (red in Fig. 4.3). Thus, the two sides of the capacitor are galvanically separated for the simulations. Furthermore, the inductive shorts of the TL (grey dashed frames) are not present in this simulation. Similar as for the TL inductance L_{TL}, also the matrix entry C'_{TL} corresponding to the TL capacitance C_{TL} has to be adjusted to the length of the resonator after the simulation. This is done by calculating the capacitance per unit length C_l of the TL cross-section with the second substrate on top, but without any LE resonator structure. Afterwards the capacitance $C_l \cdot (\Delta l_1 + \Delta l_2)$ is subtracted from C'_{TL} on both sides of the TL to get $C_{\mathrm{TL}} = C'_{\mathrm{TL}} - C_l \cdot (\Delta l_1 + \Delta l_2)$ (cf. Fig. 4.3 for definition of Δl_1 and Δl_2).

The parameters of the device depend on the position of the LE resonator with respect to the TL. For the device presented in Sec. 4.2.1, simulations of these circuit parameters are performed, as the position x of the resonator is varied with respect to the TL. The inductive parts were simulated using the numerical software package 3D-MLSI [68]. For the simulation of the capacitance matrix COMSOL Multiphysics is used. The results of the simulations are shown in Fig. 4.4. Here, $x = 0$ corresponds to the position where the center of the inductor loop (blue circle in Fig. 4.2) is centered above the center conductor of the TL. Thereby, the capacitor is on the left side of the inductor. Varying the position x, the inductance L is modified (see Fig. 4.4(c)). For positions x at which the inductive parts of the LE

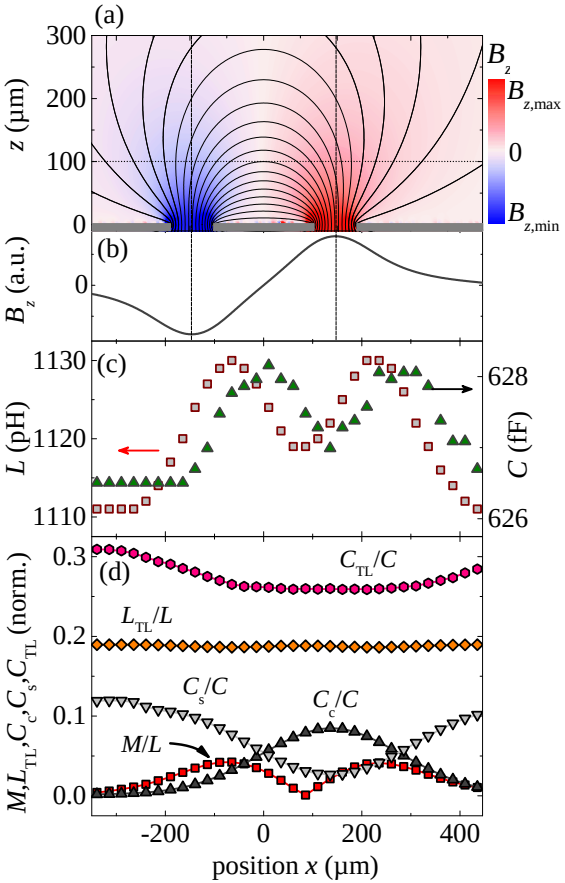

Figure 4.4.: Simulation results of the circuit. (a) Cross-sectional view of the magnetic field lines and B_z-component of the TL microwave magnetic field. Grey boxes picture the CPW. Solid line at $z = 100\,\mu$m indicates plane for, (b), linescan of B_z-component, (c), simulated variation of the inductance L and the capacitance C, and (d), normalized mutual inductance M, TL inductance L_{TL}, and capacitances C_c, C_s and C_{TL} for the position x across the TL structure. (for details see text)

resonator are above a superconducting surface, the inductance L decreases due to screening currents in the superconducting parts of the TL. These cur-

rents correspond to a mutual inductance which is mapped on L and, thereby, reduce L. Note, that this mutual inductance is not the same as M, since the origin of this mutual inductance is the bare presence of a superconducting surface below the resonator, and the origin of the mutual inductance M is the coupling to the TL. The magnetic coupling between TL and resonator is mainly mediated via the z-component of the magnetic field, or more precisely, by the flux threading the resonator. Figures 4.4(a), (b) show that the z-component B_z of the magnetic field of the TL, and hence, the inductive coupling, is expected to be strong directly above the gaps between the signal line and the ground conductor of the TL. Intuitively, one might assume that both the inductance L and the mutual inductance M are symmetric around $x = 0$. However, the symmetry axis is shifted towards $x > 0$, which can be seen in Figs. 4.4(c), (d). This is due to the fact, that the inductance of the IDC is taken into account in the simulations. The TL inductance L_{TL} remains constant (Fig. 4.4(d)).

In addition to the inductive changes, also the capacitance is modified for different positions x. Whenever the IDC is above a conducting surface, part of the electric field lines end on this surface, reducing the IDCs capacitance (Fig. 4.4(c)). This is the case when the center of the loop is above the center of the gaps of the TL at $x < -150\,\mu$m and $x \approx 150\,\mu$m, and when the LE resonator is completely above the right ground conductor at $x \approx 400\,\mu$m (note, that the IDC is on the left side of the inductor). Furthermore, changing the position x of the resonator, the TL capacitance C_{TL} is modified. For the same reason as for the capacitance C, the presence of other conducting parts, at positions of non-vanishing electric fields, leads to a reduction of the capacitance C_{TL} (Fig. 4.4(d), $-100 < x < 300\,\mu$m). In Fig. 4.4(d) the variation of the capacitances C_{c}, C_{s} is shown. The trend of C_{c} along the position x is inverted to the one of C_{s}. Thus, the sum of these capacitances remains almost constant. According to Eq. (4.7), this results in a resonance frequency which has a weak dependence on the changes of the capacitances C_{c} and C_{s} of the circuit.

Combining simulation and model

The above results of the simulations can be combined with the model of Sec. 4.2.2 in order to predict the behavior of the stacked device as a function of the position x. First, however, a short comparison between the exact model and the approximation of Eq. (4.10) is performed. $R = 0.005\,\Omega$ is

estimated for the resistance, leading to an internal quality factor of about $Q_\mathrm{i} \approx 8200$. In order to demonstrate the validity of the above approximations, for selected values of the position x, both the exact (grey circles) and approximated (red lines) amplitude and phase of the forward scattering parameter $S_{21}(\omega)$ are shown in Fig. 4.5 as a function of frequency ω. Excellent agreement for all experimentally relevant regimes is found. Thus, fits to measurement data using Eq. (4.10) is valid for all of these regimes.

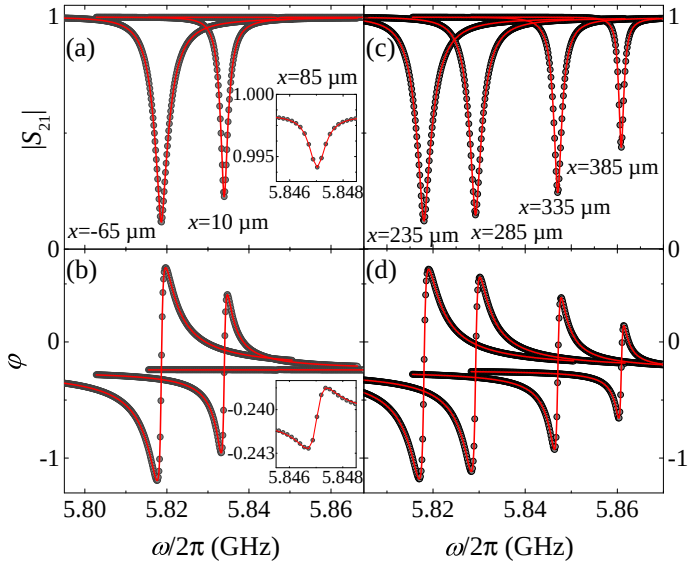

Figure 4.5.: Comparison between the exact model (grey circles) and Eq. (4.10) (red lines). (a), (c) show the amplitude, (b) and (d) the phase of the forward scattering parameter $S_{21}(\omega)$ for various positions x.

For different positions x, the simulation results are used to calculate $S_{21}(\omega, x)$, illustrated in Fig. 4.6. Regarding the corresponding resonance frequencies $\omega_\mathrm{r}(x)$ and external quality factors $Q_\mathrm{e}(x)$ in Fig. 4.7(a), one finds that both resonator properties have extremal values at $x_1 \approx 85\,\mu$m, $x_2 \approx -65\,\mu$m and $x_3 \approx 230\,\mu$m, where the former position corresponds to a maximum and the latter two denote minima. Moreover, on the one hand the maximum at $x = x_1$ appears to be more peaked for the external quality factor than for the resonance frequency, on the other hand, the minima

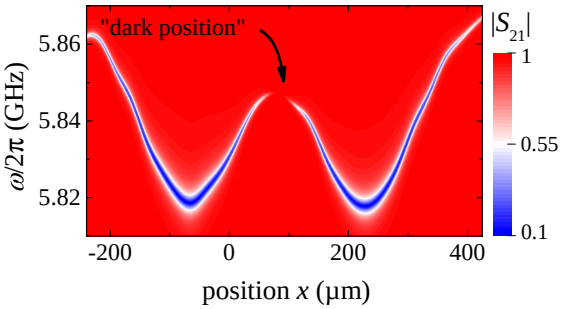

Figure 4.6.: Simulated transmission amplitude $|S_{21}(\omega, x)|$ as a function of the position x.

($x = x_{2,3}$) are more spiky for the resonance frequency (note, that this behavior is also found for a linear plot of $Q_e(x)$). This behavior enables the discrimination of regimes, in which either shifts of the resonance frequency ω_r compared to the resonator linewidth ω_r/Q_L or the relative change of the external quality factor Q_e is dominant. Here, Q_L is the loaded quality factor calculated via $1/Q_L = 1/Q_e + 1/Q_i$, where Q_i is the internal quality factor. In order to analyze these regimes in more detail, the relative change of the external quality factor $dQ_e/dx \cdot 1/Q_e$, and the spatial derivative $d\omega_r/dx$ of the resonance frequency, normalized to the resonator linewidth ω_r/Q_L (cf. Fig. 4.7(b)) is calculated. For the calculations, the internal quality factor was chosen to be $Q_{i,4\,K} = 10^4$ and $Q_{i,mK} = 10^5$ to account for internal losses at $T = 4\,K$ and mK temperatures, respectively. For an intuitive understanding of the regimes it is useful to look at the absolute values of the resonator properties (Fig. 4.7(a)) and their normalized spatial derivatives (Fig. 4.7(b)) simultaneously.

In **regime I** around the maximum at $x = x_1$, the coupling strongly depends on x, indicated by the sharp peak of Q_e and the comparatively large values of its relative changes (cf. Fig. 4.7(a), (b)). However, the absolute change of the resonance frequency is rather small. Thus, in this regime, ranging from $60\,\mu m < x < 100\,\mu m$, the position can be varied such that the device is either over-coupled ($Q_e < Q_i$), or under-coupled ($Q_e > Q_i$), without causing significant changes of the resonance frequency. In particular, at the maximum of the external quality factor ($x_1 = 85\,\mu m$), corresponding to the minimum of the mutual inductance M, one finds a position where

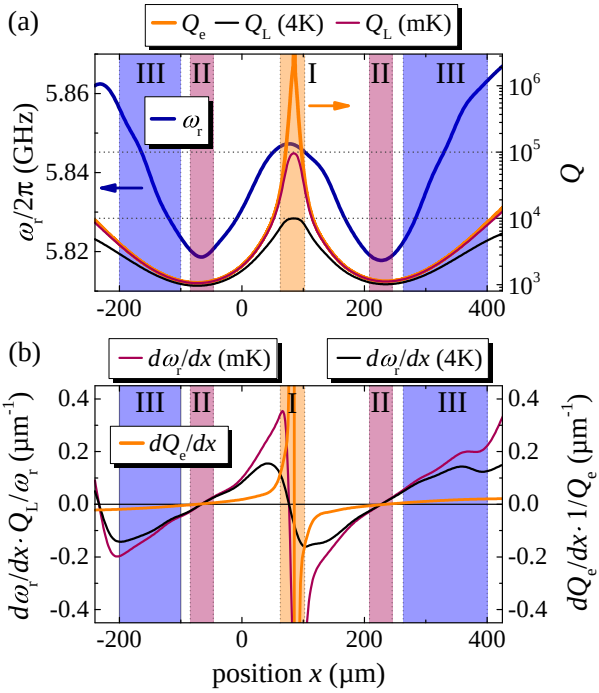

Figure 4.7.: Discrimination of regimes for varying position x. (a) Resonance frequency (blue line; left axis) and external quality factor (orange line; right axis). In addition, the loaded quality factor Q_L is plotted for two different Q_i's, taking realistic values for 4 K (black line) and 10 mK (red line). Here, $Q_{i,4\,K} = 10^4$ and $Q_{i,mK} = 10^5$ is assumed, indicated by dashed grey lines. (b) spatial derivative of the resonance frequency normalized to the cavity linewidth ω_r/Q_L (black line, $T = 4$ K; red line $T \approx$ mK), and relative change of the external quality factor. Colored areas correspond to regimes **I** to **III** (for details see text).

almost no coupling can be observed, which is called "dark position" in the following (cf. Fig. 4.6(a)).

One further regime, namely **regime II**, can be found close to the minima $x_{2,3}$ ($-85\,\mu m < x < -45\,\mu m$ and $210\,\mu m < x < 250\,\mu m$). Here, according to the vanishing spatial derivatives, neither of the resonator properties shows significant changes. Thus, for these positions, the resonator properties are quite stable against variations of the position x.

Finally, in **regime III**, which can be found within $-200\,\mu\text{m} < x < -100\,\mu\text{m}$ and $260\,\mu\text{m} < x < 400\,\mu\text{m}$, the relative changes of Q_e are still rather small, however, the resonance frequency is shifted. In this regime, varying the position can be efficiently used to tune the resonance frequency of the device, without leaving the over-coupled limit ($Q_\text{e} < Q_\text{i}$). Therefore, the model predicts a tunability of 25 MHz. Opposed to using SQUID arrays or ferroelectrics, the tuning due to the variation of the position does not result in significant changes of the internal quality factor [128, 129] (cf. Sec. 3.1).

In summary, the device enables the operation in regimes where both the external quality factor and the resonance frequency can be shifted independently of each other. In addition, there is a regime in the over-coupled limit, where none of the resonator properties depends strongly on variations of the position x.

4.2.4. Comparison between model and measurement

As a demonstration of suitability, a comparison between the model using the simulation results, and measurement, is performed for varying position x. In

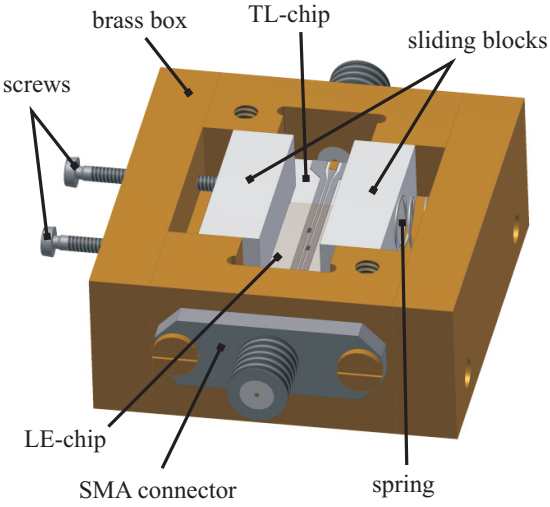

Figure 4.8.: Sample holder used for varying the position x (for details see text).

the experiment at $T = 4.2\,\mathrm{K}$, the position of the resonator is changed using the sample holder shown in Fig. 4.8. It consists of a brass box, in which the TL with finite ground planes is mounted. The TL is connected to the input and output circuit via SMA connectors. On top of the TL-chip, the LE-chip is clamped between two sliding blocks, which have small millings such that the LE-chip is tightly attached to the TL-chip. A lid closes the sample holder (not shown). The position can be changed by rotating the screws, whereas the spring takes care for a small pressure on the LE-chip, which accordingly can be moved in both directions. At different positions x, the forward scattering parameter $S_{21}(\omega, x)$ is measured (Fig. 4.9(b)). Regarding Figs. 4.6 and 4.9(b) the calculated and measured forward scattering parameter $S_{21}(\omega, x)$ can be compared, demonstrating a qualitatively good agreement. As predicted by the model, by changing the position x, the measured resonance frequency of the device is shifted. Furthermore, the depth of the dip is modified, indicating position dependent coupling strengths. More precisely, in accordance with the model, Fig. 4.9(b) demonstrates that the depth of the resonance dip decreases when x is increased from $-65\,\mu\mathrm{m}$ to $\approx 85\,\mu\mathrm{m}$, and gets deeper again when x is increased even more. The measured data are fitted using Eq. (4.10) (see Fig. 4.9(a)). In Fig. 4.9(b)-(d) the extracted fit parameters, ω_r, Q_e (green circles) are compared with the calculations of the model (Eqs. (4.7), (4.11)) using the simulations (red squares). For the sake of comparability, the calculated resonance frequencies were shifted upwards by a factor of 1.0023. This small difference can be assigned to originate from a slightly larger substrate thickness of the LE-chip, resulting in smaller capacitances C_c, C_s and higher resonance frequencies. Then, model and measurement agree both qualitatively and quantitatively very well for the resonance frequency ω_r. Despite the qualitative agreement, the external quality factor Q_e is underestimated by the model since it does not include the entire experimental setup, e.g. the in- and output coupling to the SMA connectors (note, that this is the reason for the different color scales in Figs. 4.6(a) and 4.9(b)). This can lead to standing waves on the transmission line [131], decreasing the coupling between the resonator and the TL for the resonator being close to a magnetic field node of such a standing wave. One further issue, falsifying the extracted value of Q_e, is the finite width of the ground planes of the TL, disabling proper grounding conditions and supporting parasitic transmission through the sample holder [52, 132]. In that case the sample holder acts as a hollow waveguide. Thus, some parasitic microwave power is transmitted from one port to the other,

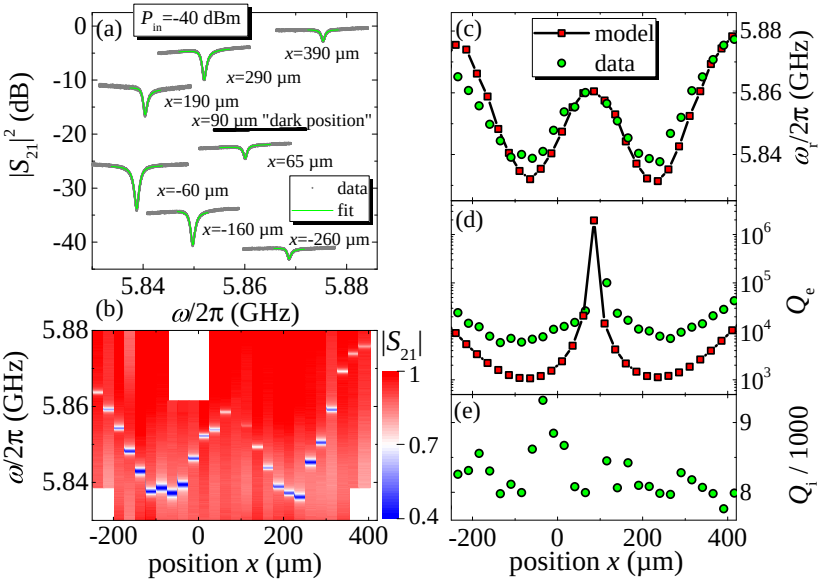

Figure 4.9.: Comparison of model and measurement. (a) transmission measurements for different positions x with an input power of $P_{\mathrm{in}} = -40\,\mathrm{dBm}$ (grey) with best fits using Eq. 4.10 (green lines) - for clarity, data are shifted along the vertical axis randomly. Black line corresponds to data at the dark position. (b) measured $|S_{21}(\omega, y)|$, (c)-(e) ω_{r}, Q_{e} and Q_{i} as a function of x for model (red squares) and measured data (green circles).

masking the ratio of off-resonance and on-resonance transmission, which, due to the fit with Eq. (4.10), defines $Q_{\mathrm{i}}/Q_{\mathrm{e}}$. However, as the model predicts for $x \approx 85\,\mu$m, also in the measurements there is a certain position above the signal line of the TL, at which no coupling between resonator and TL can be observed. Such a position corresponds to a huge external quality factor Q_e (peak in Fig. 4.9(d)). Experimentally, a dark position is found at $x = 90\,\mu$m (see black data in Fig. 4.9(b)), which is close to the position predicted by the model. The measurement for this position does not show a resonance dip. Hence, in Fig. 4.9, at $x = 90\,\mu$m one data point of the extracted fit parameters of the measurement is missing. As expected, the internal quality factor Q_i does not show a systematic dependency on the position x, and is $Q_i \approx 8000$ (Fig. 4.9(e)).

To conclude, in this section a circuit model for the stacked two-chip device was developed. Based on simulations of the circuit parameters for varying position x of the LE resonator with respect to the TL, the model allowed for predicting the forward transmission $S_{21}(\omega, x)$ as a function of frequency and position. A systematic analysis of the position dependent resonator properties revealed different regimes in which the device can be operated. In particular, moving the resonator can be used to tune the resonance frequency by about 25 MHz. The comparison with experimental results of the device for different positions x demonstrated excellent agreement with the predictions of the model. As a consequence, there are two very important conclusions of this section: First, the not very obvious approach of simulating the circuit parameters (especially considering the inductance matrix) seems likely to capture the underlying physics of the device properly and motivates the investigation of circuit parameters as a function of geometry using simulations, and second, the excellent agreement between model and measurement stimulates the optimization of the resonator geometry with respect to maximized coupling to the atoms. The latter will be addressed in one of the following sections.

4.3. Lumped element resonators - platform for ultracold atoms

In order to use the LE resonators as an atom chip, the atoms have to be trapped above the inductive loop of the LE resonator. This section deals with the optimization of the resonator geometry regarding maximum coupling to the atoms.

4.3.1. Optimization of geometrical parameters

In order to get an estimate of the geometry of a resonator optimized for maximum magnetic coupling to the magnetic ground state of the ^{87}Rb atoms, the optimization of the circuit parameters as a function of the geometry of a symmetric resonator is discussed. In order to maximize the magnetic coupling, the on-resonance current $I_{\mathrm{res}} \propto 1/\sqrt{L}$ has to be maximized, and accordingly the inductance L minimized. The symmetric geometry is schematically shown in Fig. 4.10(a). It consists of an interdigital capacitor (IDC) with a width l_C and a number of fingers N with a corresponding length l_N.

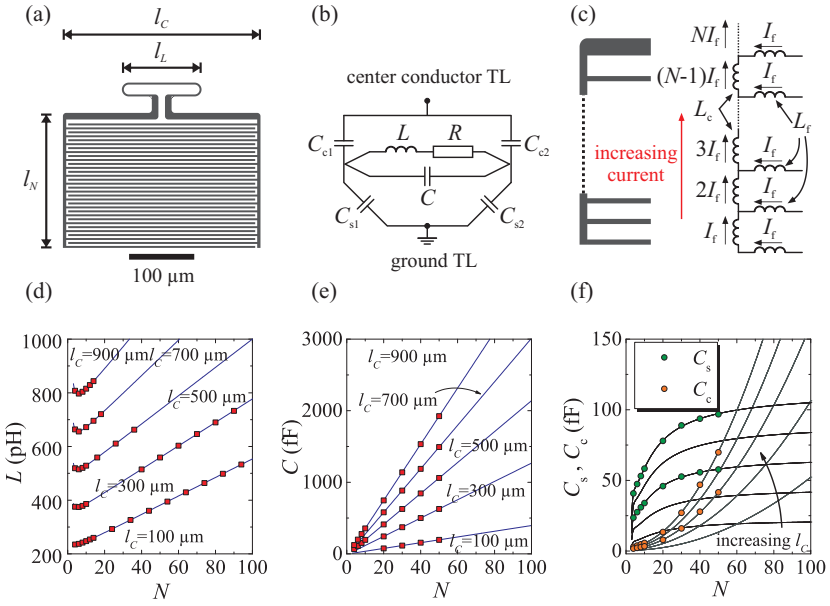

Figure 4.10.: Circuit parameters as a function of geometry. (a) geometry of the LE resonator with loop width l_L, capacitor width l_C and number of capacitor fingers N with corresponding length l_N. (b) simplified circuit model, (c) circuit model for the inductance of the IDC, (d), (e), (f) inductance L, capacitance C and capacitances C_c, C_s for different l_C as a function of N.

The inductive loop has a width l_L. In Sec. 4.2 it has been shown that the resonance frequency ω_r of such a symmetric resonator is independent of the magnetic coupling to the TL via the mutual inductance M. Furthermore, the following optimization is restricted to considering the resonance frequency using the simplified circuit depicted in Fig. 4.10(b). Thus, the magnetic coupling is neglected. The simplified circuit consists of the inductance L, the capacitance C and the capacitances between the resonator and the center conductor ($C_{c1,2}$) and ground plane ($C_{s1,2}$) of the TL. For a symmetric resonator $C_{c1} = C_{c2} = C_c$ and $C_{s1} = C_{s2} = C_s$ is satisfied. Later on, an asymmetry regarding these capacitances is introduced, necessary for loading the resonator capacitively instead of inductively.

Suppose the loop width is given, say, $l_L = 130\,\mu\text{m}$. Then, the choice of l_C and N defines the total inductance L and the capacitances C, C_c, C_s, setting the resonance frequency to

$$\omega_\text{r} = \frac{\omega_\text{u}}{\sqrt{1+\gamma/2}} \ , \tag{4.13}$$

where $\omega_\text{u} = 1/\sqrt{LC}$ is the uncoupled resonance frequency and $\gamma = (C_\text{c} + C_\text{s})/C$ (cf. Sec. 4.2.2). In order to facilitate resonant coupling between the resonator and the atoms using the desired atomic ground state transition, the resonance frequency has to obey $\omega_\text{r} = \omega_\text{a} \approx 2\pi \cdot 6.834\,\text{GHz}$. Thus, l_C and N can not be chosen independently and the choice of N restricts the capacitor width l_C to a specific value. On the one hand increasing l_C leads to an increased inductance of both the connecting inductive part between IDC and inductive loop and each individual finger. On the other hand, increasing N leads to an increased inductance related to the length l_N. Accordingly, the total inductance L increases with both l_C and N. Thus, there has to be an optimal combination of l_C and N minimizing L while satisfying the resonance condition.

For different capacitor widths l_C the circuit parameters are simulated as a function of N. Then, fits of the simulation results are performed, shown in Fig. 4.10(d)-(f). These fits for different capacitor widths l_C are compared, allowing to describe both the inductance $L(l_C, N)$ and capacitance $C(l_C, N)$ as a function of l_C and N analytically. The capacitance is found to be (affine) linear in both arguments. The inductance, however, has a slightly more complex dependence on the geometrical parameters. This dependence can be understood from Fig. 4.10(c). For small N, the inductance L is reduced with increased N due to combining each individual finger inductance L_f in parallel, causing a $1/N$ dependence. Increasing the number of fingers even further, however, results in an increasing current from bottom to top in the connecting links between neighboring capacitor fingers (cf. Fig. 4.10(c)). Thus, the inductance L_c of each individual link has to be scaled by the current running through the link, resulting in a linear dependence for large $N > 20$. With increasing l_C, the minimum of L can be found for higher values of N, which is consistent with the described model. The analytical expressions $L(l_C, N)$ and $C(l_C, N)$ allow for the calculation of the resonance frequency ω_r as a function of the geometry parameters l_C and N. In particular, parameter sets satisfying the resonance condition $\omega_\text{r} = \omega_\text{a}$ can be filtered. The obtained parameter sets and the corresponding inductances

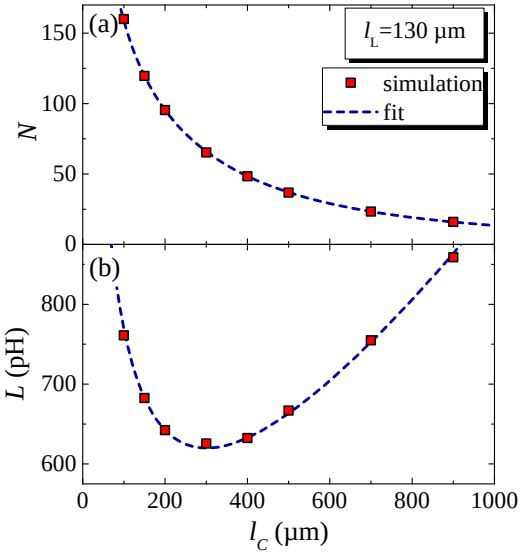

Figure 4.11.: Optimization of geometric parameters for maximum magnetic coupling. (a) number of fingers N as a function of l_C corresponding to parameter sets satisfying $\omega_r \approx 2\pi \cdot 6.834\,\mathrm{GHz}$, and (b), associated inductance L. Red squares and blue dotted lines correspond to simulated and fitted results of the calculations, respectively.

are depicted in Fig. 4.11(a) and (b), respectively. Maximum magnetic coupling for the symmetric geometry is found to be achieved for $l_C \approx 300\,\mu\mathrm{m}$ and $N = 66$ with an inductance of $L \approx 620\,\mathrm{pH}$.

4.3.2. Driven resonator and single-photon coupling

Next, the coupling of the optimized resonator to an ultracold cloud of ^{87}Rb atoms is discussed. First, consider the case where the resonator is driven by an external microwave source via the coupling to the TL. For this special case, the atoms couple to both the LE resonator and the TL. Thus, at first the coupling g of the atoms to both subsystems, or more precisely the magnetic field amplitude $|B| \propto g$, assuming the currents running in the TL and the LE resonator to be equal ($I_{\mathrm{TL}} = I_{\mathrm{LE}}$) is simulated. Then, the ratio $B_{\mathrm{LE,max}}/B_{\mathrm{TL}}$ of the magnetic fields at the prospective position of the atoms corresponding to these currents, as a function of the position x of the

inductive loop with respect to the TL, is analyzed. Finally, the "real" ratio $I_{\mathrm{LE}}/I_{\mathrm{TL}}$ of these currents as a function of both the external coupling of the LE resonator to the TL (which also depends on x) and the internal quality factor Q_{i} is studied using the input-output formalism.

The microwave magnetic field amplitude of the TL B_{TL} normalized to the maximum of the magnetic field of the LE resonator $B_{\mathrm{LE,max}}$ can be seen in Fig. 4.12(a) as well as its inverse for $I_{\mathrm{TL}} = I_{\mathrm{LE}}$. The curves demonstrate that for $x = 0$ the magnetic field of the TL is about a factor of 10 smaller than the magnetic field of the LE resonator. For $x = \pm 350\,\mu\mathrm{m}$ the factor is increased to about 50, increasing even more for higher values of $|x|$. This is due to the focusing of the magnetic field to positions close to the gap between center conductor and ground plane of the TL (even for a distance $z = 115\,\mu\mathrm{m}$ to the TL-chip surface). Accordingly, it is more favorable to place the inductive loop of the LE resonator at a position $|x| > \pm 300\,\mu\mathrm{m}$ above one of the ground planes of the TL.

The analysis of the experimental setup is refined by taking into account the internal and external quality factors Q_{i}, Q_{e} and correspondingly the ratio $I_{\mathrm{LE}}/I_{\mathrm{TL}}$. Using the input-output formalism, the average number of photons $\bar{n}$ of a coherent state in the side-coupled resonator can be calculated as

$$\bar{n} = \frac{2P_{\mathrm{in}}}{\hbar\omega_{\mathrm{d}}} \frac{\kappa_{\mathrm{e}}}{\kappa^2 + 4\Delta^2} \ , \tag{4.14}$$

with the average power flow $P_{\mathrm{in}} = 1/2 Z_0 I_{\mathrm{TL}}^2$ of the wave propagating along the TL (with current amplitude I_{TL}) and the offset $\Delta = \omega_{\mathrm{d}} - \omega_{\mathrm{r}}$ between drive frequency ω_{d} and the resonance frequency $\omega_{\mathrm{r}} = 2\pi \cdot 6.834\,\mathrm{GHz}$. $\kappa_{\mathrm{e}} = \omega_{\mathrm{d}}/Q_{\mathrm{e}}$ and $\kappa_{\mathrm{i}} = \omega_{\mathrm{d}}/Q_{\mathrm{i}}$ respectively denote the external and internal part of the overall loss $\kappa = \kappa_{\mathrm{e}} + \kappa_{\mathrm{i}}$. Note that Eq. (4.14) describes a Lorentzian lineshape. On resonance ($\Delta = 0$) Eq. (4.14) simplifies. Then, the time-averaged on-resonance current in the LE resonator can be found as

$$I_{\mathrm{res}} = \sqrt{\frac{\hbar\omega_{\mathrm{r}}(\bar{n} + 1/2)}{L}} \approx \sqrt{\frac{Z_0}{L}\frac{\kappa_{\mathrm{e}}}{\kappa^2}} \cdot I_{\mathrm{TL}} \ , \tag{4.15}$$

where the approximation applies to high input powers P_{in} and accordingly large average photon numbers $\bar{n}$, allowing to neglect the vacuum fluctuations. For different internal quality factors ranging from typical values of about $Q_{\mathrm{i,4K}} = 10000$ at a temperature of 4.2 K to $Q_{\mathrm{i,mK}} = 100000$ at mK-temperatures, the ratio $I_{\mathrm{LE}}/I_{\mathrm{TL}}$ is shown in Fig. 4.12(b) as a function of the

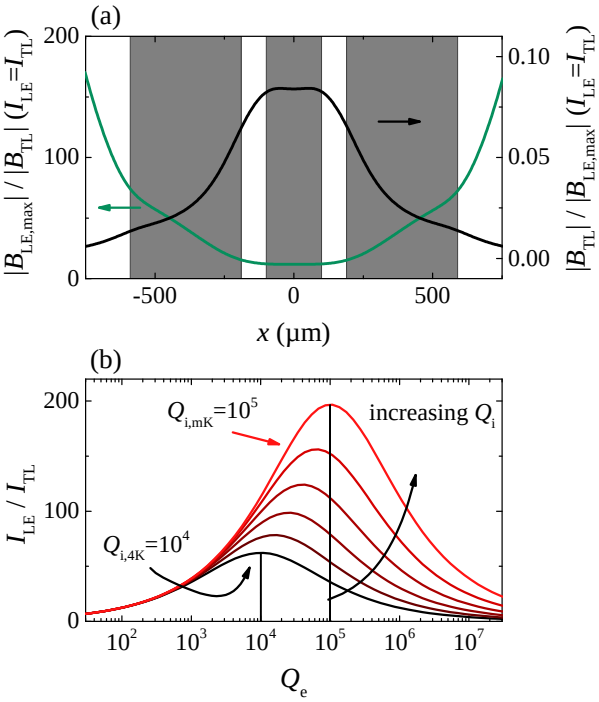

Figure 4.12.: Calculation of the coupling between atoms and both TL and LE resonator. (a) Magnetic field amplitude $|B_{\mathrm{TL}}|$ of the TL normalized to the magnetic field amplitude of the LE resonator $|B_{\mathrm{LE,max}}|$ (black line, right axis) and its inverse (green line, left axis). (b) Ratio $I_{\mathrm{LE}}/I_{\mathrm{TL}}$ as a function of Q_{e} for different Q_{i} from $Q_{\mathrm{i,4K}} = 10000$ to $Q_{\mathrm{i,mK}} = 100000$.

external quality factor Q_{e}. For the internal quality factor at 4 K one can find optimum values of $I_{\mathrm{LE}}/I_{\mathrm{TL}} \approx 60$, increasing for the mK-$Q_{\mathrm{i}}$ to a factor of about 195. The optimum external quality factor $Q_{\mathrm{e,opt}}$ maximizing the ratio $I_{\mathrm{LE}}/I_{\mathrm{TL}}$, thereby maximizing the average number of photons in the LE resonator, can easily be found to obey $Q_{\mathrm{e,opt}} = Q_{\mathrm{i}}$ (cf. vertical lines in Fig. 4.12(b)).

For the analysis of the coupling of the atoms to both the TL and the LE resonator the relative coupling ratio g_{rel} is defined as

$$g_{\mathrm{rel}} = \frac{g_{\mathrm{LE}}}{g_{\mathrm{TL}}} = \frac{|B_{\mathrm{LE,max}}|}{|B_{\mathrm{TL}}|} \cdot \frac{I_{\mathrm{LE}}}{I_{\mathrm{TL}}} \tag{4.16}$$

with the coupling rates g_{LE} and g_{TL} of the atoms to the LE resonator and the TL, respectively. Referring to Fig. 4.7 in Sec. 4.2, for the symmetric resonator and the 4 K internal quality factor $Q_{\mathrm{e,opt}} = Q_{\mathrm{i}}$, optimized coupling is achieved for $x \approx 40\,\mu$m. For the mK-Q_{i} the corresponding position is $x \approx 70\,\mu$m. Accordingly, in both cases the atoms are placed above the center conductor of the TL with $|B_{\mathrm{LE,max}}|/|B_{\mathrm{TL}}| \approx 12$ (for $I_{\mathrm{LE}} = I_{\mathrm{TL}}$). Multiplying with the "real" ratio $I_{\mathrm{LE}}/I_{\mathrm{TL}}$ for the optimized coupling between the LE resonator and the TL one gets a relative coupling of about $g_{\mathrm{rel,4K}} = 720$ for $Q_{\mathrm{i,4K}}$ and a factor of about $g_{\mathrm{rel,mK}} = 2350$ for $Q_{\mathrm{i,mK}}$ between the coupling of the atoms to the TL and the LE resonator. In order to increase the relative coupling g_{rel} even further, it is advantageous to couple the resonator capacitively instead of inductively to the TL. Therefore, modifications of the resonator geometry have to be made, as shown in Sec. 4.3.3. First, however, the single spin - single photon coupling is discussed.

Coupling between individual spins and photons

The figure of merit of any cQED architecture is given by the gate fidelity, i.e. the reliability of the process used to exchange single excitations (or even less) between subsystems. As shown in the preceding section, based on the large possible values of $g_{\mathrm{rel,mK}}$ the residual coupling to the TL can be neglected and the stacked two-chip approach in principle allows for gate fidelities close to unity. Then, the limitations of the gate fidelity are given by the coherence time of the atoms as well as both the internal and external quality factors of the resonator device. For the purpose of large gate fidelities one has to enter the strong coupling regime, i.e. $g_{\mathrm{LE}} \gg \kappa, \gamma$, where $\kappa = \omega_{\mathrm{r}}/Q_{\mathrm{L}}$ is the overall cavity loss and γ accounts for the coupling of the atoms to modes other than the resonator mode (e.g. to the TL). The coupling between the magnetic moment $\vec{\mu}_{\mathrm{a}}$ of the atoms and magnetic field $\vec{B}_{\mathrm{LE}}$ of the resonant microwave mode of the LE resonator for parallel orientation is given by

$$g_{\mathrm{LE}} = \frac{|\mu_{\mathrm{a}}| \cdot |B_{\mathrm{LE}}|}{\hbar} \sqrt{N} \ , \tag{4.17}$$

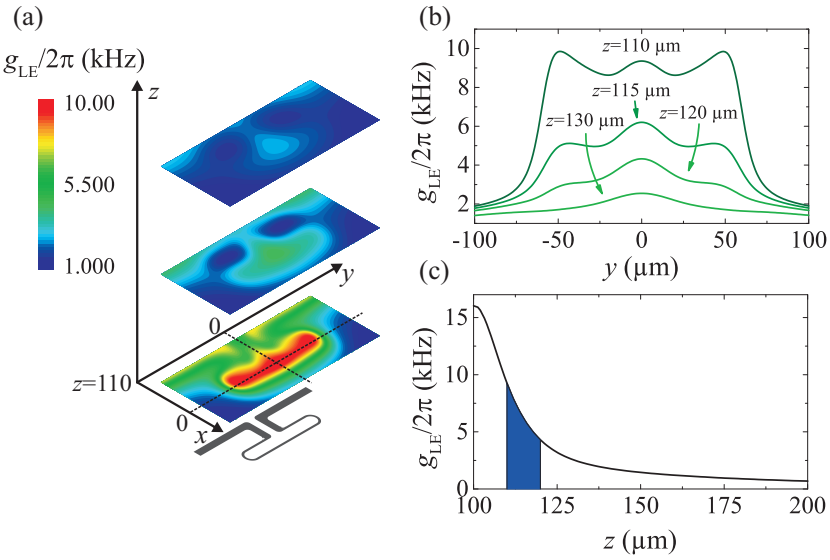

Figure 4.13.: Coupling between LE resonator and cold atoms. (a) Inductive loop of the resonator with color plots of the collective coupling of $N = 10^6$ atoms for distances $z = 110, 120, 130\,\mu$m (from bottom to top). (b), (c) linescans of the coupling for the y- and z-direction, respectively. Blue area in (c) corresponds to positions of trapped atoms. $y = 0$ corresponds to center of the loop, the surface of the LE resonator is located at $z = 100\,\mu$m.

where N is the number of atoms coupled to the same resonant microwave magnetic field mode with amplitude $|B_{\mathrm{LE}}|$, and the magnetic moment for the desired transition is $|\mu_{\mathrm{a}}| = 0.612\mu_{\mathrm{B}}$[2] [133]. The collective coupling of the atoms and the resonator is summarized in Fig. 4.13 for a number $N = 10^6$ of trapped atoms, as usual for such experiments [21, 44]. Figure 4.13(a) shows the coupling g_{LE} for the distances $\Delta z = 10, 20, 30\,\mu$m to the surface of the LE-chip ($z = \Delta z + 100\,\mu$m). For increasing distance, the coupling is reduced. Moreover, the homogeneity considering the y-direction is reduced and shows pronounced maxima for $y = 0$, i.e. the center of the loop, due to the expansion of the magnetic field (cf. Fig. 4.13(b)). For experiments at

[2]The magnetic moment of the transition is calculated using the dipole-matrix-element $\langle 0|\,\hat{\mu}\,|1\rangle$, where $\hat{\mu}$ is the matrix of all possible transmissions.

single-photon energies this will result in a reduced effective number of atoms and thereby will reduce the coupling. For the desired trapping positions of the atoms ($110\,\mu\text{m} < z < 120\,\mu\text{m}$) the coupling can be found as $g_{\text{LE}} = 4 - 8\,\text{kHz}$. The weakening of the coupling g_{LE} in the z-direction above the center of the loop is shown in Fig. 4.13(c). At a distance of $\Delta z = 50\,\mu\text{m}$ to the LE-chip surface, the coupling has reduced to about 2 kHz.

As a result of this section, using LE-resonators instead of the $\lambda/2$-resonators can increase the coupling by roughly one order of magnitude (cf. [45]). At 200 mK internal quality factors of about $Q_{\text{i}} = 5 \cdot 10^5$ have been reported for niobium [134]. It seems plausible that this can be increased even further for realistic temperatures of about 50 mK in our cryostat [46]. Accordingly, such coupled systems are at the threshold for strong coupling, i.e. $g_{\text{LE}} \approx \kappa, \gamma$. For internal quality factors above 10^7, coupling directly to the magnetic ground state becomes a reasonable option for using the atoms as quantum memory. To date, such high quality factors have been reported only for CPW resonators in the high power regime [135]. For LE resonators at single photon energies, however, the best quality factors reported yet are about several 10^5. Accordingly, coupling LE resonators at single photon energies to the magnetic ground states of ultracold atoms directly will result in poor gate fidelities for the moment.

4.3.3. Modifications of the experimental setup

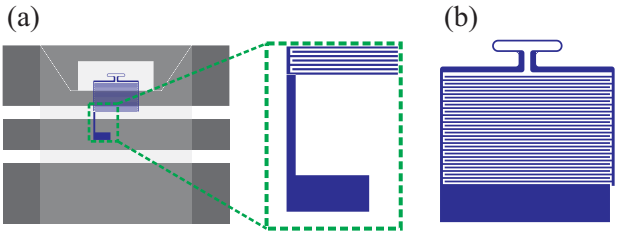

Figure 4.14.: Modifications of the resonator geometry. (a) Schematic of TL with a rectangular hole in the upper ground plane and a LE resonator with "hockey stick"-like capacitive part on top, adding an asymmetry regarding the capacitances C_{c1}, C_{c2} and C_{s1}, C_{s2}. Zoomed version shows "hockey stick" geometry. (b) Alternative for adding an asymmetry with the lowest finger having a significantly increased width.

For the symmetric case of the resonator geometry of the preceding section, the coupling between the TL and the resonator is purely inductive via the mutual inductance M. The main part of the mutual inductance between TL and resonator is due to the inductive loop of the LE resonator. Accordingly, the microwave magnetic field of the TL can be quite large close to the loop. Thus, if ultracold atoms are trapped there, the atoms couple to both the LE resonator and the TL. Consequently, modifications of both the TL and the resonator geometry can be made in order to further increase the relative coupling g_{rel}. In short, the coupling between resonator and TL then is chosen to be (almost) purely capacitive.

More precisely, a hole is cut in one of the ground planes of the TL close to the position where the atoms are to be trapped (cf. Fig. 4.14(a)). The closed superconducting loop thus allows for freezing in the desired amount of flux by applying a magnetic field in z-direction during cooling down below the critical temperature T_{c} of the superconductor, and afterwards switching off the applied field. In combination with homogeneous magnetic fields in all spatial directions and a current through the center conductor of the TL, the field cooling of flux into the hole offers the possibility of generating a magnetic trap for ultracold atoms, as discussed in the following section.

Furthermore, two of several possible approaches to add an asymmetry regarding the capacitances C_{c1} and C_{c2} as well as between C_{s1} and C_{s2} are presented in the following. The first approach is adding a "hockey stick"-like capacitive structure which connects to one side of the IDC (see zoom in Fig.4.14(a)). The second approach is simply increasing the width of the lowest capacitor fingers, as shown in Fig.4.14(b). In addition, with respect to the TL the LE-chip is aligned such that the microwave magnetic field of the TL is negligible compared to the magnetic field of the LE resonator, thus reducing both the magnetic coupling between the TL and the resonator via $M \approx 0$ and the coupling between the TL and the ultracold atoms.

Using this approach the relative coupling g_{rel} can be increased by a further factor of ≈ 5 compared to the symmetric resonators shown before.

4.3.4. Magnetic trap for Rubidium atoms

One upcoming challenge for hybrid quantum systems which combine superconducting resonators and ultracold ensembles of ^{87}Rb atoms, is to trap the atoms in close vicinity to the maximum of the magnetic field of the resonant microwave mode. The solution which has been established in our labs, is to

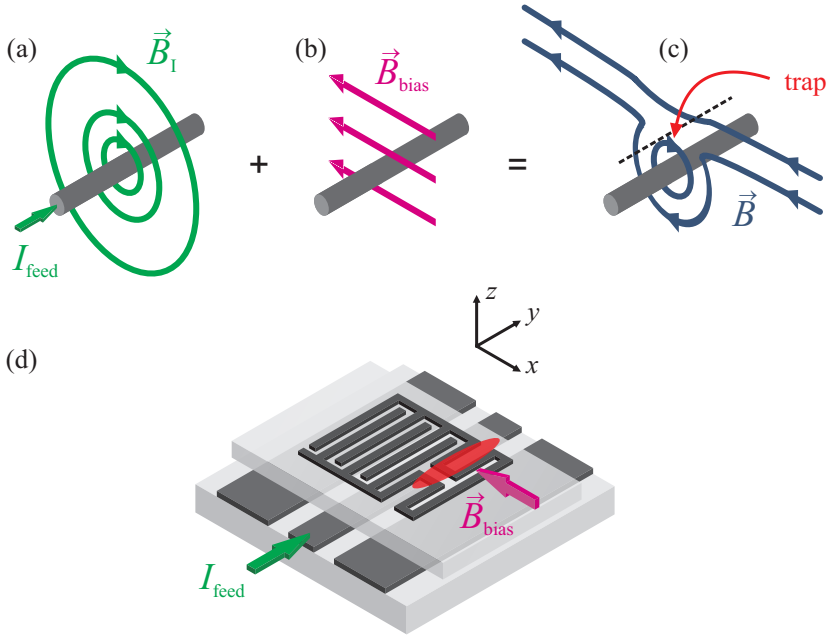

Figure 4.15.: Working principle of the magnetic trap for paramagnetic atoms. The superposition (c) of (a) a radially decreasing magnetic field $\vec{B}_{\mathrm{I}}$ generated by a current carrying wire with a current I_{feed}, and (b) a homogeneous bias field $\vec{B}_{\mathrm{bias}}$, vanishes above the wire. Thereby, a magnetic trap for paramagnetic atoms is formed. (d) Realization of a trap for paramagnetic atoms using the TL center conductor as current carrying wire.

generate a local minimum of the magnetic field magnitude $|\vec{B}(\vec{r})|$ [48]. The working principle of such a trap is demonstrated in Fig. 4.15. Superimposing a radially decreasing magnetic field generated by using a current carrying wire (I_{feed} in Fig. 4.15(a)) with a homogeneous bias field $\vec{B}_{\mathrm{bias}} = B_x\hat{e}_x$ (Fig. 4.15(b)) leads to a vanishing magnetic field above the wire at a distance proportional to $I_{\mathrm{feed}}/|\vec{B}_{\mathrm{bias}}|$ (Fig. 4.15(c)). Thereby, a magnetic trap for paramagnetic atoms is formed (if $g_F m_F < 0$). The stacked two-chip approach can very elegantly be used to form such a trap by simply applying the current I_{feed} to the center conductor of the TL (Fig. 4.15(d)). Accordingly,

no additional trapping wires are required, reducing both stray capacitances and inductances and thus parasitic transmission.

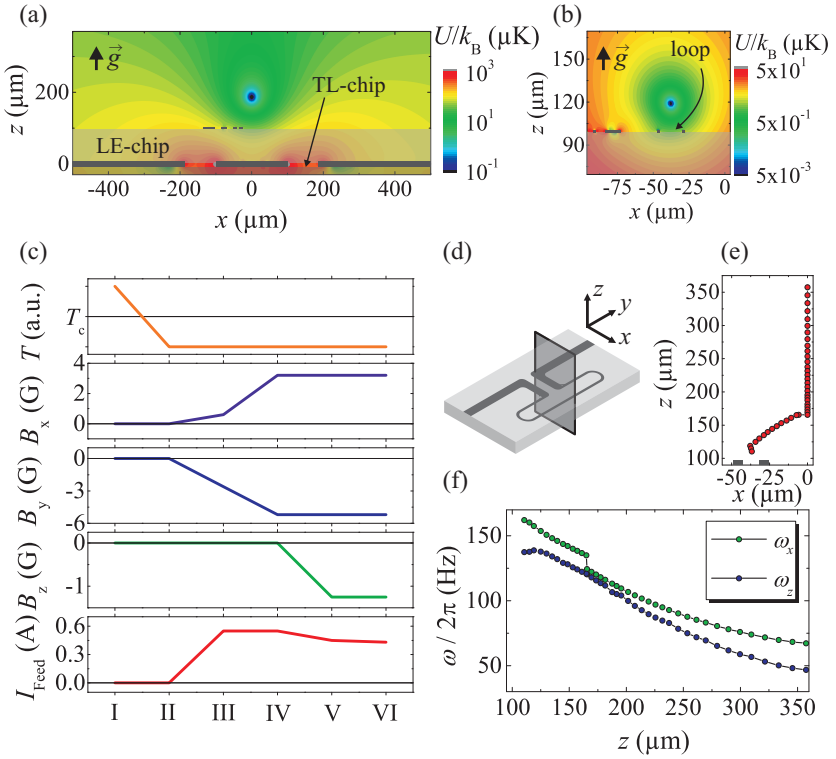

Figure 4.16.: Magnetic trap for paramagnetic ^{87}Rb atoms. Trapping potential U showing an intermediate (a) and the final position (b) of the magnetic trap. Gravity is included. $x = 0$ corresponds to the center of the center conductor of the TL, the plane $z = 0$ represents the surface of the TL. Black circle marks the trap minimum. (c) Sweep sequence for the magnetic field and the current I_{feed} through the feed-line. (d) Schematic of the experimental setup, (e) position of the trap minimum and (f), corresponding trap frequencies ω_x and ω_z during the sweep sequence as a function of the distance z to the surface of the TL-substrate.

For the two-chip device numerical simulations of the magnetic trap for ^{87}Rb atoms in the magnetic ground states $|0\rangle := |5S_{1/2}, F = 1, m_F = -1\rangle$ and $|1\rangle := |5S_{1/2}, F = 2, m_F = 1\rangle$ are performed. Both of these states are

so-called low-field-seeking states ($g_F m_F > 0$). The magnetic potential for such atoms is given by $U(\vec{r}) = m_F g_F \mu_B |\vec{B}(\vec{r})|$, with the Bohr magneton μ_B and the Landé-factors g_F of the magnetic ground states under consideration $g_1 = -1/2$ and $g_2 = 1/2$ [136]. Thus, under the influence of an inhomogeneous magnetic field, atoms in these states sense a force directed towards the magnetic field minimum. Lateral confinement is guaranteed using two additional confinement wires located below the TL-chip and pointing towards the x-direction (not shown). These wires are symmetrically aligned with regard to the LE resonator and have a separation of $1000 - 1500\,\mu$m.

For the simulation of the trap the linear London equations are solved numerically for the experimental setup shown in Fig. 4.15(d) using the finite element software 3D-MLSI [68]. The magnetic field vectors for different configurations of all experimentally relevant parameters, namely the magnetic field perpendicular to the chip surface $\vec{B_z} = B_z \hat{e}_z$, the magnetic field generated by the current I_{feed} through the center conductor of the TL and the magnetic fields generated by the currents through the confinement wires are superimposed. Furthermore, the screening currents arising from the field expulsion (M.-O.-effect) of the above mentioned magnetic fields, flowing at the edges of each superconductor, are included. Finally, gravity is taken into account via $U_g = -m_{\text{Rb}} g z$ with $g = 9.81\,\text{m/s}^2$. For the parameters $B_z = 0$, $B_x = |\vec{B}_{\text{bias}}| = -4.6\,\text{G}$, $B_y = 2.6\,\text{G}$ and $I_{\text{feed}} = 550\,\text{mA}$, the resulting potential landscape for a ^{87}Rb atom is shown in Fig. 4.16(a) (note, that in Fig. 4.16(a) and (b) gravity points upwards). The magnetic field component in parallel with the TL, B_y, is unequal to zero in order to form a harmonic trap [48] preventing Majorana spin-flips. Furthermore, the total field strength $|B_{\text{tot}}| = 3.2\,\text{G}$ is chosen such that for the desired transition $|0\rangle \rightarrow |1\rangle$ the transition frequency is extremely stable against variations of the magnetic field, according to the minimum of the Breit-Rabi-parabola [48]. This magnetic field is often referred to as the *magic offset field*.

For an infinitely thin wire the distance of the trap minimum to the chip surface is given by $z = \mu_0 I_{\text{feed}} / 2\pi B_y$, where μ_0 is the vacuum permeability. Despite the finite width of the center conductor of the TL, this expression provides an intuition of the trapping position. Thus, either decreasing I_{feed} or increasing B_y shifts the trap minimum towards the chip surface. The sweep of the experimental parameters is shown in Fig. 4.16(c). The sample is cooled below its critical temperature T_c without any applied fields or currents (I-II). After the cool-down, the current I_{feed} is ramped up to a value

of 550 mA (III), whereas the magnetic fields $B_{x,y}$ are ramped up slowly up to $B_x = -5.2\,\mathrm{G}$ and $B_y = 3.2\,\mathrm{G}$, respectively (III-IV). Using these parameters a trap forms above the center conductor of the TL at a distance of about $250\,\mu\mathrm{m}$ to the surface of the LE resonator, i.e. the final position of the atoms during the transfer from the MOT (magneto-optical-trap) to the chip using optical tweezers. Then, I_{feed} and thus the distance to the LE-chip surface is subsequently decreased (V). Finally, while I_{feed} is lowered even more, the magnetic field perpendicular to the chip surface B_z is ramped to a final value of $B_z = -1.25\,\mathrm{G}$ for trapping the atoms at a distance of about $13\,\mu\mathrm{m}$ above the loop of the LE resonator. Figure 4.16(b) shows the trapping potential $U(\vec{r})$ for the final position, using the parameters $B_z = -1.25\,\mathrm{G}$, $B_x = -5.2\,\mathrm{G}$, $B_y = 3.2\,\mathrm{G}$ and $I_{\mathrm{feed}} = 430\,\mathrm{mA}$. The positions of the atoms during the parameter sweep can be found in Fig. 4.16(e). The steepness of the trap regarding the x- and z-direction is shown in Fig. 4.16(f) respectively captured by the trapping frequencies ω_x, ω_z for a parabolic potential $U(\vec{r})$ along both the x- and z-direction. The trap frequencies for the final position are about $\omega_x = 160\,\mathrm{Hz}$ and $\omega_z = 140\,\mathrm{Hz}$, respectively. Such frequencies have shown to be suitable for achieving long atomic coherence times [32].

4.3.5. Behavior under biasing conditions

Magnetic field performance

Next, the performance of symmetric resonators similar to the one shown in Fig. 4.10 is characterized under the influence of the biasing conditions. First, the properties of such resonators are studied in magnetic bias fields oriented perpendicular to the chip surface with a maximum absolute value of $B_{z,\mathrm{max}} = 2.5\,\mathrm{mT}$. The geometrical parameters of the measured samples varied within $100\,\mu\mathrm{m} < l_L < 900\,\mu\mathrm{m}$, $100\,\mu\mathrm{m} < l_C < 900\,\mu\mathrm{m}$ and $8 < N < 120$. However, it is found that the properties of the resonators in magnetic fields do not have a strong dependence on the geometry of the resonators for the investigated range of parameters. Thus, at first the discussion is restricted to one of those resonators ($l_L = 320\,\mu\mathrm{m}$, $l_C = 900\,\mu\mathrm{m}$, $N = 10$). Later on, the discussion is extended to the full data set. The experimental setup used for the investigation of the resonator properties in out-of-plane magnetic fields is schematically shown in Fig. 4.17(a). The LE-chip is mounted on top of the TL chip such that the inductive loop of the resonator is above the center conductor of the TL. For a homogeneous magnetic field B_z applied

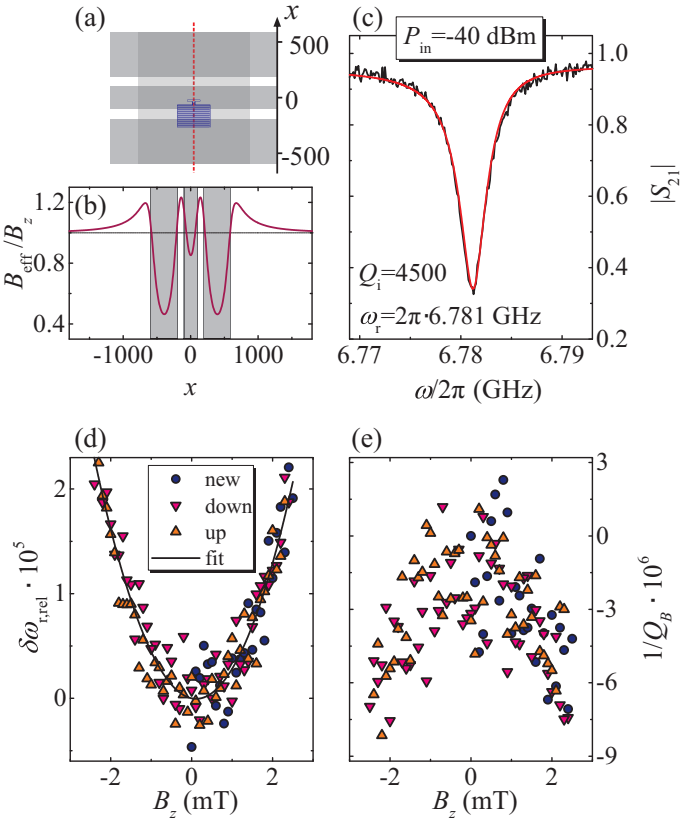

Figure 4.17.: Characterization of the resonator properties in magnetic fields. (a) Experimental setup, (b) linescan along the red line in (a) of the magnetic field distribution at $z = 100\,\mu$m above the TL for a homogeneous magnetic field B_z applied perpendicular to the chip surface. (c) Data and fit of the transmission amplitude $|S_{21}|$ for $B_z = 0$. (d), (e) Relative frequency shift $\delta\omega_{r,rel}$ and magnetic field induced loss factor $1/Q_B$ as a function of the magnetic field B_z for a hysteresis sweep. In (d), data are fitted using a parabolic dependence $\delta\omega_{r,rel} \propto B_z^2$.

perpendicular to the chip surface, the magnetic field distribution above the TL chip for a distance $z = 100\,\mu$m to the TL-chip surface is simulated using 3D-MLSI. In this simulation the LE resonator is not taken into account. The

result of the simulation is shown as a linescan across the TL in Fig. 4.17(b). Due to the Meissner currents generated by the superconducting TL parts, the magnetic field is distorted close to the TL. In particular, the field is focused into the gaps of the TL, thereby increasing the ratio of the actual value of the z-component of the magnetic field B_{eff} and the applied magnetic field B_z to a maximum of 125% above these gaps at a distance to the TL surface of $z = 100\,\mu$m. Above the ground planes of the TL, the magnetic field is reduced to about 45% of the applied magnetic field B_z, above the center conductor the field is reduced to about 90%. However, the z-component of the magnetic field required to generate a magnetic trap for paramagnetic atoms is $< 1\,$mT. Thus, the magnetic fields used to test the resonators are representative for the surrounding conditions of the experimental setup used to couple the atoms to the resonator.

The amplitude $|S_{21}(\omega)|$ of the transmission measurement at $B_z = 0$ is shown as a function of the frequency ω in Fig. 4.17(c) with a fit using the expression

$$S_{21} = Ae^{i\phi}\frac{1 + 2iQ_{\mathrm{i}}\frac{\Delta\omega}{\omega_{\mathrm{r}}}}{1 + \frac{Q_{\mathrm{i}}}{Q_{\mathrm{e}}} + i\frac{Q_{\mathrm{i}}}{Q_{\mathrm{a}}} + 2iQ_{\mathrm{i}}\frac{\Delta\omega}{\omega_{\mathrm{r}}}}\,. \tag{4.18}$$

In this expression ω_{r} is the resonance frequency, Q_{i} and Q_{e} denote the internal and external quality factors, and Q_{a} accounts for an asymmetric lineshape of the resonance dip.

For a superconductor in the Meissner-phase, one finds a parabolic dependence of the resonance frequency on a magnetic field aligned perpendicular to the chip surface using the nonlinear London equations [137]. However, for a superconductor in the Shubnikov-phase, one expects hysteresis effects of both the resonance frequency and the internal quality factor Q_{i} of the resonator [50]. These resonator properties are analyzed using the relative frequency shift $\delta\omega_{\mathrm{r,rel}} = (\omega_{\mathrm{r}}(B_z = 0) - \omega_{\mathrm{r}}(B_z))/\omega_{\mathrm{r}}(B_z = 0)$ and the magnetic field induced internal loss factor $1/Q_B = 1/Q_{\mathrm{i}}(B_z) - 1/Q_{\mathrm{i}}(B_z = 0)$. The results are presented in Fig. 4.17(d), (e). Both the relative frequency shift and the magnetic field induced loss factor are found to be shifted in magnetic fields. More precisely, in accordance with the measurements presented in Ref. [137] the relative frequency shift shows a parabolic dependence. A relative frequency shift of about $\delta\omega_{\mathrm{r,rel}}(2.5\,\mathrm{mT}) = 2.2 \cdot 10^{-5}$ and a magnetic field induced loss factor of roughly $1/Q_B(2.5\,\mathrm{mT}) = 5 \cdot 10^{-6}$ is found at the maximum applied magnetic field of $B_{z,\mathrm{max}} = 2.5\,$mT. Due to the smallness of these magnetic-field-induced relative shifts, the data presented in

Fig. 4.17 seem noisy. Thus, a hysteresis of the resonator properties can not be observed. However, if a significant number of vortices were present in the sample, the related relative frequency shifts and field induced loss factors, at least for TL resonators, would be up to two orders of magnitude larger [50]. Accordingly, it seems likely that, if any, there are only a few Abrikosov vortices present in the superconducting parts of the resonator. This is due to the narrow width $w_L = w_C = 2.4\,\mu$m of the current carrying parts of the resonators and the corresponding small distortion of the magnetic field B_z.

For all investigated samples, the difference of the relative frequency shift $\delta\omega_{\mathrm{r,rel}}$ and the magnetic field induced loss factors lie within a factor of 0.5 to 3 compared to the sample presented above. The full data set does not show a systematic dependence on the resonator geometry or the resonance frequency.

Performance under current bias

In addition to the magnetic field characterization, the behavior of the resonator as a function of a bias current I_{feed} running along the center conductor of the TL is measured as well. The experimental setup used to apply both microwave signals and direct currents to the stacked device is shown in Fig. 4.18(a). The superconducting device is cooled down to a temperature of 4.2 K in liquid helium (yellow box). The capacitances and inductances were explained in Sec. 4.3.1. The room temperature part of the experimental setup consists of a PNA network analyzer and a dc current source, which are combined using a bias-T.

The forward transmission $S_{21}(\omega)$ is measured as a function of the current I_{feed} to a maximum of $I_{\mathrm{feed,max}} = 200\,$mA. A simulated linescan of the corresponding z-component of the magnetic field generated by the maximum current is shown in Fig. 4.18(b) at a distance $z = 100\,\mu$m to the TL. Obviously, close to the position of the LE resonator, the field does not exceed a value of 0.2 mT. Thus, even if the current was on the order of 1 A, the z-component of the magnetic field maximum for $z = 100\,\mu$m generated by the current through the center conductor would be smaller than the maximum applied homogeneous magnetic field (cf. Sec. 4.3.5). Accordingly, it seems likely that the resonator properties are quite stable when the dc current is applied. This can be seen in in Figs. 4.18(c), (d). In accordance with the magnetic field performance, also the data presented in this section seem very noisy, which once again can be attributed to the fit procedure. The "noise

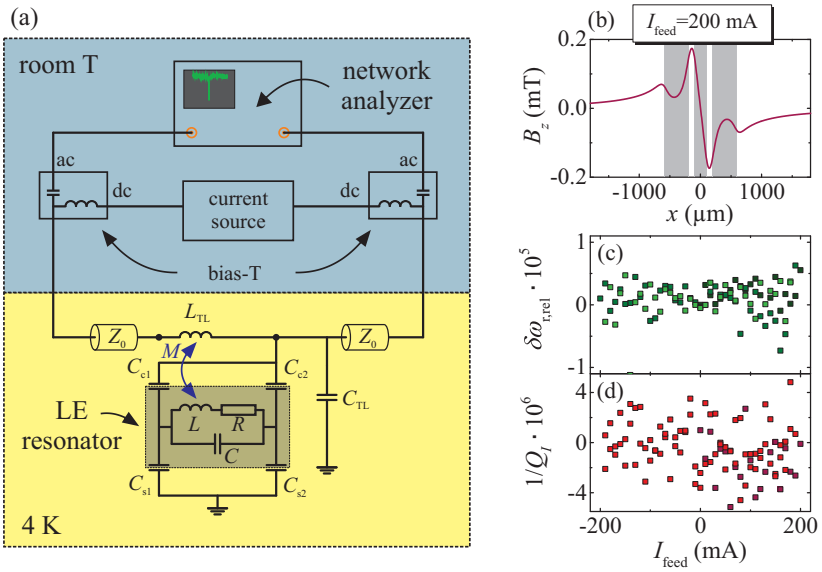

Figure 4.18.: Characterization of the resonator properties with dc current. (a) Experimental setup, (b) linescan of the z-component of the magnetic field generated by a current $I_{\mathrm{feed}} = 200\,\mathrm{mA}$ through the center conductor of the TL. (c), (d) Relative frequency shift $\delta\omega_{\mathrm{r,rel}}$ and current induced internal losses $1/Q_I$, respectively.

amplitude" is about $\delta\omega_{\mathrm{r,rel,max}} \approx 1 \cdot 10^{-5}$ for the relative frequency shift, and about $1/Q_{I,\mathrm{max}} \approx 8 \cdot 10^{-6}$ for the current induced internal loss factor. Note, that the quantities $\delta\omega_{\mathrm{r,rel}}$ and $1/Q_I$ are defined in analogy to the corresponding quantities of the magnetic field characterization, except that instead of the dependence on the magnetic field B_z the quantities are considered as a function of the current I_{feed}.

Summarizing this section, the resonator properties are found to be very stable in magnetic bias fields up to $B_{z,\mathrm{max}} = 2.5\,\mathrm{mT}$ and under the influence of the magnetic field generated by a current through the center conductor of the TL up to $I_{\mathrm{feed,max}} = 200\,\mathrm{mA}$. Due to the non-hysteretic behavior of the resonator properties it seems likely that almost no vortices are present in the superconducting parts of the LE resonator. Simulations of the magnetic field generated by the dc bias current suggest that this is true even for larger

currents of about 1 A. Accordingly, the resonators work well for all conditions applied to the sample in experiments with ultracold atoms.

Moreover, the stacked two-chip device allows for trapping cold atoms in close vicinity to the inductive loop of the LE resonator, bringing the atoms into the area of influence of the resonator. Using the center conductor of the TL as trapping wire reduces the number of stray capacitances and inductances and reduces parasitic transmission. Furthermore, due to the narrow superconducting wires of the LE resonator, Meissner-currents running along these wires cause only small distortions. Thus, without the chip mounted, or with any other chip (using narrow wires), trapping of atoms at roughly the same position is possible for minor changes of the experimental parameters. The optimized design of the resonators and the ultracold atoms in magnetic ground states enables pushing the coupled LE resonator/cold atom system towards the desired regime of strong coupling $g_{\mathrm{LE}} \approx \kappa, \gamma$.

4.3.6. LE resonators for coupling to Rydberg atoms

Based on the best quality factors reported for LE resonators to date [134] it seems most likely that coupling to the magnetic ground states of cold atoms is not suitable for an application in cQED experiments, where $g_{\mathrm{LE}} \gg \kappa, \gamma$ is required. As an alternative, increased coupling to the internal quantum mechanical degrees of freedom of the ^{87}Rb atoms can be achieved by using the highly excited Rydberg states instead of magnetic ground states [138, 139]. In analogy to the magnetic coupling, the exchange energy g_{Ry} between a single Rydberg atom with an electric dipole moment of $\vec{d}_{\mathrm{Ry}}$ and the microwave electric field $\vec{E}_{\mathrm{LE}}$ is given by

$$g_{\mathrm{Ry}} = \frac{\vec{d}_{\mathrm{Ry}} \cdot \vec{E}_{\mathrm{LE}}}{\hbar} \ . \tag{4.19}$$

Due to the large electric dipole moments related to the high principal quantum number ($n = 40-100$) of the outermost electron, the coupling of a single Rydberg atom to a LE resonator can outperform the collective coupling of 10^6 atoms in the magnetic ground state. In particular, it is shown below, that the coupling of a single Rydberg atom to a LE resonator can be on the order of several tens of megahertz. On the other hand, these Rydberg atoms are also very sensitive to any source of interference due to the large dipole moments. Correspondingly, the coherence times of such Rydberg atoms close

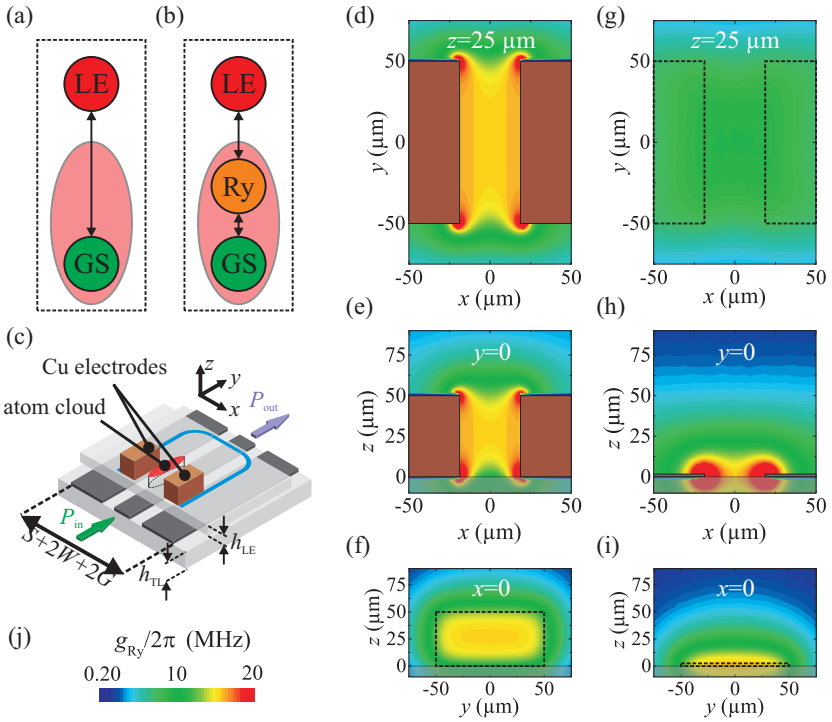

Figure 4.19.: High fidelity gate via Rydberg states using ground states as quantum memory. Schemes for coupling directly to ground state (GS) (a) and via intermediate Rydberg state (Ry), (b). Slight red ellipsoid indicates the atom part of the experiment. (c) Schematic of the stacked device with a TL with typical cross-sectional dimensions, i.e. center conductor width $S = 200\,\mu$m, gap between center conductor and ground planes $W = 90\,\mu$m and ground plane width $G = 400\,\mu$m. Brown parts indicate a parallel plate capacitor (copper), blue wire indicates the inductor, red ellipsoid illustrates the trapped atom cloud. (d)-(f) and (g)-(i) Coupling g_{Ry} of Rydberg atoms to the LE resonator in the xy-plane for $z = 25\,\mu$m, xz-plane for $y = 0$ and yz-plane for $x = 0$, respectively, for a LE resonator with parallel plate capacitor and one with a flat capacitor. Transparent grey parts indicate the substrate. If present in the respective profiles, bronze parts indicate copper electrodes, else dashed boxes show the projection onto the profile. (j) Color scale of the coupling g_{Ry} for (d)-(i).

to a superconducting resonator are on the order of $\tau_{\mathrm{Ry}} \approx 100\,\mu$s. In order to make use of the long-living magnetic ground states and for preventing

a fast decay of quantum information a mapping technique to the magnetic ground states of the atoms has been proposed [35]. Instead of coupling to the magnetic ground states directly (Fig. 4.19(a)), these strongly interacting Rydberg atoms can serve as an intermediate state (Fig. 4.19(b)) allowing both large gate fidelities and the transfer of quantum information to the long-living ground states with coherence times of several seconds [44].

As a first step towards the implementation of such a mapping technique, resonators have to be designed and the coupling to Rydberg atoms has to be simulated. A schematic of such a resonator is shown in Fig. 4.19(c). The device combines two approaches: First, the use of a parallel plate capacitor (here copper) as a part of a ($\lambda/4$-) resonator in order to have the electric fields between the parallel plates uniform in both magnitude and direction [139]. And second, the use of the stacked two-chip approach elaborated in Sec. 4.2. As a consequence of using the two-chip approach, the results of Sec. 4.2 also apply to the present approach. As an example, the parallel plate LE resonator will also have a tunable resonance frequency and a tunable coupling to the TL depending on the position of the resonator with respect to the TL. Thus, varying the position can be used for adjusting the resonance frequency to a desired value. Trapping of atomic clouds between the capacitor plates can be achieved by using a trapping scheme similar to the one described in Sec.4.3.

The following estimation of the coupling will be restricted to the transition between the Rydberg states $57S_{1/2} \rightarrow 57P_{3/2}$ with an atomic resonance transition frequency of about $\omega_{\mathrm{Ry}} = 20.2\,\mathrm{GHz}$ and a dipolar moment of $d_{\mathrm{Ry}} = 2700 a_0 e$, where a_0 is the Bohr radius and e is the charge of an electron. The dimensions of the copper electrodes will be about $(x, y, z) = (50, 100, 50)\,\mu\mathrm{m}$ with a gap of $40\,\mu\mathrm{m}$ between the parallel plates. The corresponding capacitance is $C = 19\,\mathrm{fF}$ (sapphire substrate $\varepsilon_{\mathrm{re}} = 10.06$, voltage for vacuum fluctuations $U = \sqrt{\hbar\omega_{\mathrm{Ry}}/2C} = 18.8\,\mu\mathrm{V}$). For this transition, the coupling g_{Ry} between a single Rydberg atom and the radiation field of the LE resonator is shown in Fig. 4.19(d)-(f) in any possible plane. For comparison, the coupling to a LE resonator without parallel plates, but with the same dimensions in the xy-plane, is shown in Fig. 4.19(g)-(i), referred to in the following as the flat resonator. Using the parallel plate capacitor, the electric field is pulled out of the surface of the substrate. Thus, between the parallel plates, the coupling g_{Ry} is almost homogeneous and has a value of about $g_{\mathrm{Ry}} \approx 15\,\mathrm{MHz}$. On the other hand, for the flat resonator the coupling is found to decay strongly, such that at a typical trapping distance for

Rydberg atoms of about $z = 25\,\mu$m, g_{Ry} is reduced to $< 1/2$ of the maximum coupling. Nevertheless, the coupling is large enough to achieve strong coupling ($g_{\mathrm{Ry}} \approx 10\,$MHz). The main disadvantage of the flat resonator is the decay of the electric field amplitude along the z-direction. Accordingly, the coupling to Rydberg atoms and the corresponding energy level shift related to the dressed states depends strongly on z, inducing an inhomogeneous broadening, and thus, reducing the coherence of the atoms.

Assuming a (pessimistic) quality factor at mK-temperatures of about $Q = 5 \cdot 10^4$ the photon lifetime in the cavity can be found as $\tau_{\mathrm{LE}} = Q/\omega_{\mathrm{Ry}} \approx 2.5\,\mu\mathrm{s} \ll \tau_{\mathrm{Ry}}$. Thus, the number of Rabi oscillations n_{Rabi} is mainly limited by the cavity decay rate and can approximately found as $n_{\mathrm{Rabi}} = 2g_{\mathrm{LE}} \cdot \tau_{\mathrm{LE}} = 75$. Accordingly, using LE resonators with parallel plate capacitors can boost the coupled system deep into the desired regime of strong coupling.

One crucial point for the realization of a high fidelity gate, however, will be transferring the quantum information stored temporarily in the Rydberg state to the long-living ground state of the atoms.

5 Towards the implementation of dc-biased microwave devices in a mK-setup

This section deals with the application of the superconducting microwave devices to the mK-stage of a He^3/He^4 dilution refrigerator. For the realization of a cold atom trap, some of these microwave devices must necessarily be supplied with a direct current on the order of 300 mA. In order to not generate any heat on the mK-stage this current inevitably has to be purely superconducting. Therefore, as one part of a complex sample holder, an integrated chip design combining a bias-T with a dc-block has been developed. In the following, however, the integrated design is only referred to as the *bias-T-chip*. One further condition for the sample holder is the necessity of optical access to the surface of the atom chip. This is due to the readout of the atomic state or the transfer of atoms to the chip surface. In the following, first an overview of the sample holder is given, followed by a detailed analysis of the bias-T-chip and the first characterization of the microwave transmission through the sample holder.

5.1. Sample holder

The sample holder which is to be used for first experiments on the mK-stage is shown in Fig. 5.1(a). There are three large supporting structures of the sample holder, each of which is made of Au-coated OFHC copper due to

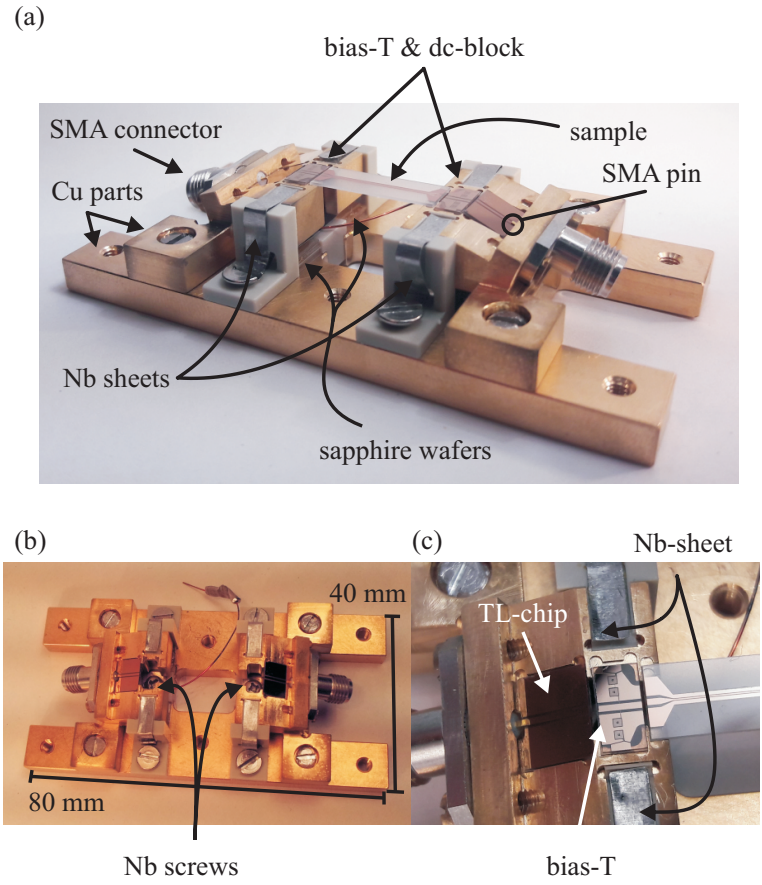

Figure 5.1.: Sample holder for experiments on the mK-stage. Optical image of (a) sample holder, (b) top view of the sample holder with removed bias-T-chip, (c) bias-T-chip mounted on top of a copper block (for details see text).

its high thermal conductivity[1]. These three parts are the bottom plate and

[1] OFHC stands for *oxygen-free high thermal conductivity*. Depending on the residual-resistance ratio (RRR), the thermal conductivity of OFHC copper typically can be found as $\sigma_{\mathrm{Cu}} \approx 80 - 700\,\mathrm{W/(m\,K)}$ at a temperature of 50 mK. At room temperature the thermal conductivity is about $\sigma_{\mathrm{Cu,RT}} \approx 400\,\mathrm{W/(m\,K)}$ independent of the RRR.

two identical copper blocks screwed on top of the bottom plate with sloping millings. Due to these millings SMA connectors can be mounted under an angle, allowing for the connection of coaxial cables which do not interfere with the optical access. In order to suppress oxygen gas emission, gold is grown on the copper surface (directly after a cleaning step in hydrochloric acid) using electro-galvanization with a thickness of about 1 μm.

The superconducting parts of the sample holder carrying large direct currents have to be galvanically decoupled from the normal conducting copper and gold parts of the sample holder in order to avoid both normal conducting (heating) currents and ground loops. Thus, insulators have to be used. The insulating parts manufactured in the workshop are made of PEEK[2] (cf. grey parts in Fig. 5.1(a), (b)). However, the niobium parts have to be connected thermally to the mK-stage in order to be cooled down below the critical temperature ($T_{\mathrm{c,Nb}} = 9.2\,\mathrm{K}$). Due to the small thermal conductivity of PEEK ($\sigma_{\mathrm{PEEK}} \approx 0.25\,\mathrm{W/(m\,K)}$) sapphire wafers are added ($\sigma_{\mathrm{sapphire}} \approx 42\,\mathrm{W/(m\,K)}$), trimmed to fit between a PEEK block and a copper block (cf. Fig 5.1(a)). Six of these sapphire wafers with a thickness of 330 μm are stacked on top of each other and glued together using VARNISH. On both sides of the symmetric sample holder a niobium sheet is glued on top of the stacked sapphire wafers.

The direct current supplied to the niobium sheets is transported to the mK-stage via niobium single-filament wires in a copper matrix, which are connected to a sub-D connector located at the 4 K-stage. The wires are thermally anchored successively on the 4 K- and mK-stages. Finally, the wires are connected to the niobium sheet by screwing a niobium screw through the sheet into a PEEK block (cf. Fig. 5.1(b)). The niobium sheets are wrapped around the upper copper blocks but are well separated from them by thin PEEK parts to prevent shorts to ground.

Each niobium sheet ends close to both short edges of a bias-T-chip mounted on top of a copper block (cf. Fig. 5.1(c)). The connection to the bias-T-chip is made using either niobium or aluminum wire bonds. From left, the microwave signal is transferred to the bias-T from a separate TL-chip, which is linked to the SMA connector using indium. The center conductor and the ground planes of these two chips are connected with indium plates along the longer edge of the bias-T-chip.

[2] PEEK stands for **p**oly**e**ther**e**ther**k**etone and is an UHV compatible insulator.

5.1.1. Details of the bias-T-chip

Fabrication

The bias-T-chip is fabricated using three different layers shown in Fig. 5.2. The first one of these starts with the deposition of a 500 nm thick film of superconducting niobium deposited by magnetron sputtering on a r-cut sapphire wafer with a substrate thickness of $h_{\mathrm{sub}} = 330\,\mu$m (Fig. 5.2(a)). After an optical lithography step using positive resist (Fig. 5.2(b)) and reactive ion etching with SF_6 the first layer is finished. This first layer contains all main parts of the chip including spiral inductors, bond pads, the TL and the bottom plate of any parallel plate capacitor of the bias-T (Fig. 5.2(c)).

All insulating parts of the chip are fabricated in the second layer using SiO_2 as an insulator. These parts are patterned via a lift-off process, starting with an optical lithography step with negative resist (Fig. 5.2(d)), followed by the deposition of SiO_2 by means of rf-sputtering with a thickness of about 300 nm (Fig. 5.2(e)) and resist removal in warm acetone supported by ultrasound. Due to the small deposition rate (3 nm/min) of the SiO_2 rf-sputtering process and the corresponding long deposition time, the whole chip, and in particular the resist, is strongly heated, resulting in drying out of the resist causing increased adherence. Thus, thereafter the sample is additionally cleaned using oxygen plasma ashing to obtain the finished second layer (Fig. 5.2(f)).

Finally, the niobium top layer is structured using a lift-off process. After another optical lithography step with negative resist (Fig. 5.2(g)), the parts of the first oxidized niobium layer which are unprotected by the resist are gradually cleaned first by plasma etching (2 minutes, Ar^+-ions) and then by reactive ion etching (SF_6, 3 minutes). The aim of the cleaning process is the disposal of the naturally oxidized niobium surface of the first niobium layer in order to avoid contact resistances, e.g. via Josephson junctions, between the two niobium layers. Then, the chip is transferred in-situ to the sputtering chamber of a UHV cluster tool. Once again superconducting niobium is deposited by magnetron sputtering with a thickness of 500 nm (Fig. 5.2(h)). Thereafter, the resist is removed in warm acetone supported by ultrasound to finalize the bias-T-chip (Fig. 5.2(i)). The top layer forms the top plates of the capacitors and connects the spiral inductors as well as ground planes via microbridges.

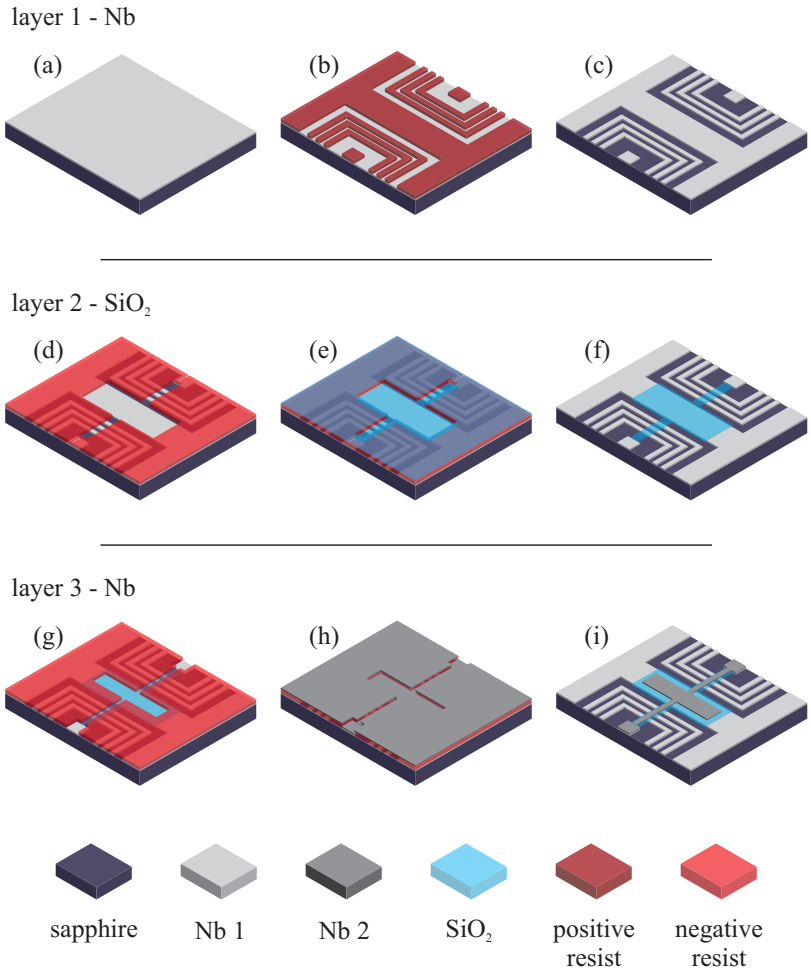

Figure 5.2.: Fabrication steps of the bias-T-chip. Layer 1 - first niobium layer used to pattern spiral inductors, bond pads and the TL. Layer 2 - SiO_2 as insulator of all parallel plate capacitors and microbridges. Layer 3 - capping layer made of niobium, forming the top plane of the capacitors and the microbridges.

T-filter and IV-characteristics

A bias-T typically has three ports. The two input ports of the bias-T, i.e. one port for dc-signals and one port for ac-signals, are combined in one output port transferring both input signals to the sample. The dc-port of the bias-T

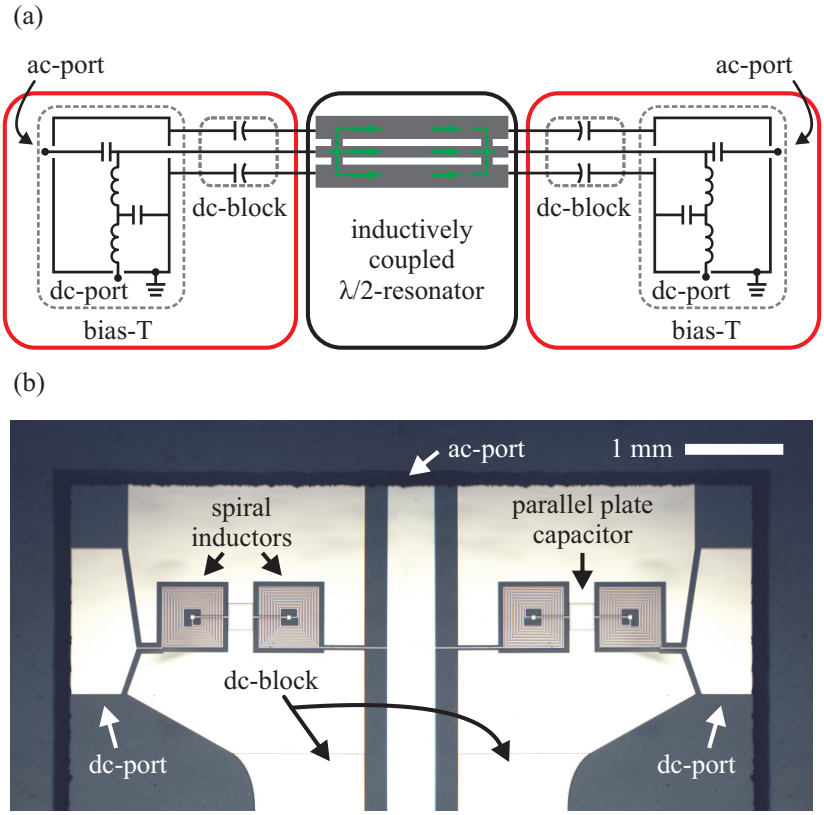

Figure 5.3.: Integrated bias-T and dc-block chip design. (a) Circuit model of the experimental setup, (b) optical microscope image of the bias-T-chip. Red boxes in (a) correspond to the circuit model for each bias-T-chip, black box frames an inductively coupled half-wavelength resonator, green arrows indicate dc-current applied to the center conductor of the resonator using the integrated bias-T-chip (for details see text).

circuit presented in Fig. 5.3(a) is linked to the output via a T-filter consisting of a combination of an inductor with a large inductance, a capacitor to ground, and another inductor with the same inductance as the first one. Thus, microwave signals are blocked efficiently. In addition, noise introduced by a current source is filtered due to the T-filter design. The ac-port is galvanically decoupled from the output using a large capacitor, preventing the flow of direct current. For large capacitances of the capacitor, however, microwave signals are transmitted to the output port with no significant amount of insertion loss. The circuit representation of the sample holder including the integrated bias-T-chip is illustrated in Fig. 5.3(a). The circuit furthermore contains a sample, i.e. in this case an inductively coupled $\lambda/2$-resonator. Such resonators allow one to trap atoms in close vicinity to the resonator gap using persistent currents running around the closed superconducting loops of the resonator [53] in addition with homogeneous magnetic bias fields and a direct current applied to the center conductor of the resonator (cf. green arrows in Fig. 5.3(a)). Due to the inductive shorts of the resonator, the ground planes of the resonator must be galvanically decoupled from the *universal* ground in order to prevent the dc-currents from flowing through it. This is provided by implementing on-chip dc-blocks forming an integrated chip design. More specifically, these are so-called *outside dc-blocks* having the ground conductors interrupted by a large capacitor, enabling the microwave to be transmitted through the ground conductors whilst dc-signals are blocked with respect to the universal ground.

The layout of the integrated chip combining a bias-T and a dc-block is shown in Fig. 5.3(b). The device is symmetric with respect to the center conductor of the TL. At both short edges of the chip bond pads are patterned for the dc-port connection to the niobium sheets using wire bonds, as shown before. Each bond pad is connected to a T-filter consisting of two spiral inductors interrupted by a capacitor to ground. Close to the center conductor of the TL, the tail of the each second inductor (from the outside to the inside) splits the corresponding ground plane in two halves and connects to the center conductor of the TL. Thus, a dc-current can be applied to the center conductor of the TL from both sides via T-filters. Two of four available designs of T-filters are shown in more detail in Fig. 5.4. As already mentioned, a T-filter consists of a serial circuit of two inductors interrupted by a capacitor to ground. The spiral inductors shown in Fig. 5.4 have 15 windings of a wire with a width of 10 μm and a gap between neighboring wires of 5 μm, leading to an inductance of about 100 nH for each

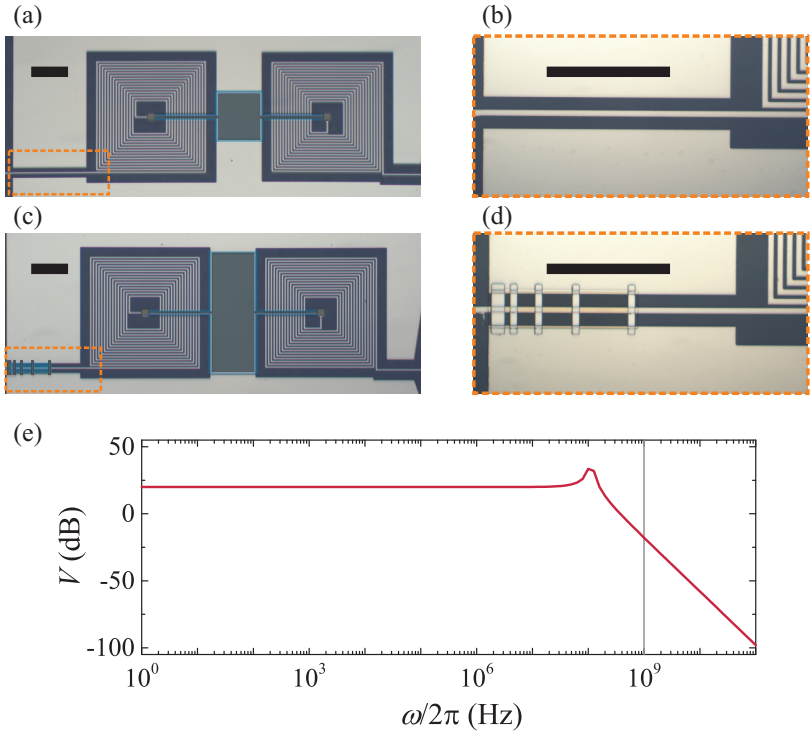

Figure 5.4.: Design variations of the T-filters and the microbridges. (a) Optical image of T-Filter design *Type 1* with smaller parallel plate capacitor and without microbridges, orange box indicates zoom for (b). (c) Optical image of T-Filter design *Type 2* with larger parallel plate capacitor and microbridges, orange box indicates zoomed version in (d). In (a) and (c), the second layer of SiO_2 is colored light blue, the third layer of superconducting niobium is colored dark grey. Black bars in (a)-(d) correspond to a length of 200 μm. (e) Simulated transmission through the T-filter as a function of frequency using LT-spice for the large capacitor. Vertical line corresponds to 1 GHz.

spiral inductor. With respect to an applied current, the spiral inductors have a reverse winding sense in order to prevent large magnetic fields in the far field (e.g. at the location of the atoms). The parameters of the spiral inductors, i.e. the number of windings, the width of the inductor and the gap between neighboring wires, were *not* varied during the thesis. However,

for the capacitor two different designs were fabricated. The sizes of these capacitors are $270 \times 270\,\mu\text{m}^2$ for the smaller, $270 \times 670\,\mu\text{m}^2$ for the larger capacitor (cf. Fig. 5.4(a) and (c), respectively), resulting in capacitances of about 9 pF and 22 fF, respectively, assuming a dielectric constant of 4.2 for the SiO_2 layer with a thickness of 300 nm. Due to the relatively large values of both the inductance and the capacitance of the T-filter, a resonance of both filters occurs for frequencies on the order of $100 - 200$ MHz. Figure 5.4(e) shows the simulation result of the transmission characteristics of the T-filter with the larger capacitance as a function of the frequency tested via a resistance of 1 MΩ. The curve demonstrates that for small frequencies the signal is transmitted through the inductors. In particular, the curve shows that the T-filter is designed such that dc-currents required to trap the atoms close to the chip can be ramped in a couple of milliseconds. Increasing the frequency across the resonance of the T-filter leads to a temporary increase of the voltage at the resistor, i.e. the resonance frequency. Increasing the frequency even further results in a drastic reduction of the transmitted voltage (note the logarithmic dB-scale). Thus, at high frequencies in the microwave domain the T-filter is expected to block microwave signals applied to the ac-port of the bias-T.

In addition to the variations of the capacitor there are also samples with and without microbridges (cf. Fig. 5.4(b), (d)). The microbridges are used to interconnect the two ground plane parts separated by the tail of the T-filter directing towards the center conductor of the TL (cf. Fig. 5.4(d)). Instead of one single large bridge that extends over the entire width of the separated ground conductor, which would result in a large capacitance to ground and thus would represent a short for high frequencies, five narrow microbridges are structured. Due to the large microwave currents at the edges of the ground planes, the innermost bridge has a width of 20 μm. Owing to the decay of the microwave currents running in the ground planes for increasing distance to the center conductor, all other microbridges have a width of 10 μm with an increasing separation between neighboring bridges.

Next, the IV-characteristics are discussed for one of the two T-filters located on each bias-T-chip (for a filter with microbridges and the large capacitor). Therefore, the bias-T chip is mounted in a standard sample holder and connected to its ports by wire bonds at the bond pad and the output port. Assuming a typical critical current density of superconducting niobium of about $6 \cdot 10^6\,\text{A/cm}^2$ and taking into account the thickness of 500 nm and the width of the conductor 10 μm, the device should allow for currents of about

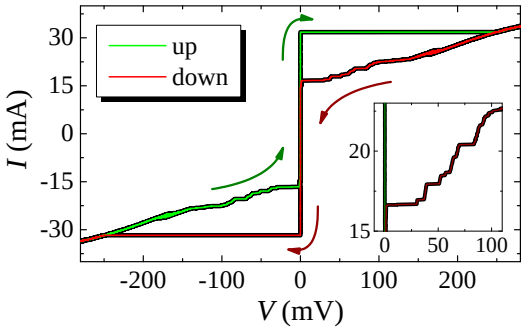

Figure 5.5.: IV-characteristics of the T-filter. Measurement of the voltage for a bidirectional up- and down-sweep of the current through the T-filter. Inset shows a zoom into the down-sweep part for positive currents.

300 mA for each T-filter. The result of the IV-measurement is presented in Fig. 5.5 showing a similar behavior as the IV-curve of a hysteretic Josephson junction with a large shunt resistance. For a virgin sample currents up to ≈ 31 mA are purely superconducting. For higher currents the sample enters the resistive branch. The associated resistance grows so strongly with increasing current that the linear regime of the IV-curve can not be measured with the experimental setup. After turning the sweep direction, the curve does not follow the same behavior as during the up-sweep. Moreover, the inset in Fig. 5.5 shows that during the down-sweep of the applied current the voltage does not vanish at once but stepwise instead. Finally, for currents below 14 mA the device returns to the superconducting state. With respect to positive and negative currents and voltages the IV-curve of the T-filter is symmetric.

Based on the results of the IV-measurement it seem likely that the T-filter structure forms weak links, leading to the formation of hot spots[3] [140] (note, that the weak link most certainly does not result in a Josephson junction). Accordingly, the occurrence of the hysteresis can be explained as caused by the large resistance in the resistive branch and the associated heating due to the hot spot. Due to the discrete steps during the down-sweep it furthermore seems plausible that the T-filter contains several weak links. As

[3] At least, the maximum current should not be limited by the maximum supercurrent through a 10 μm wide and 500 nm thick wire.

soon as one of the many weak links enters the resistive state during the up-sweep, generating a hot spot, the heating due to the hot spot instantaneously forces all other weak links to enter the resistive regime as well. During the down-sweep, however, the weak links turn back into the superconducting state separately.

For the multi-layered device it seems moos likely that weak link is induced by the numerous ups and downs of the niobium top layer above the spiral inductors. At these points, the conductor may break or at least be much thinner than the film thickness of about 500 nm, thereby forming a weak link. A reliable interpretation of the results, however, can only be made using imaging techniques, e.g. low-temperature scanning electron microscopy.

Briefly summarizing, it has been shown that the T-filter design can carry supercurrents up to 31 mA, adding up to ≈ 60 mA if the second filter is included. For the formation of a cold atom trap, however, purely superconducting currents on the order of 200 mA are required. Despite the roughly three times smaller current achieved for the bias-T-chip, the IV-characteristics demonstrate that the device can in principle work. Using meandered inductors instead of spiral inductors enables the fabrication of all inductive parts in one layer, thereby avoiding steps.

dc-blocks and microwave characterization

For the transmission of microwaves, the general layout of the bias-T-chip is structured as a CPW TL with a width of the center conductor of $S = 500\,\mu$m and gap between center conductor and the ground planes of $W = 223\,\mu$m. The dc-blocks integrated into the bias-T-chip can be seen in Fig. 5.6. As one part of the bias-T-chip the inside dc-block consists of a parallel plate capacitor with the dimensions $500 \times 500\,\mu$m and a capacitance of about 30 pF interrupting the center conductor of the TL (cf. Fig. 5.6(a)). The capacitor blocks dc-signals while microwave currents can be transmitted according to an absolute value of the impedance below $1\,\Omega$ for frequencies above $2\pi \cdot 6$ GHz. The same principle applies to the outside dc-bocks shown in Fig. 5.6(b) with dimensions of about $275 \times 1200\,\mu$m, or alternatively $650 \times 1200\,\mu$m.

The basic concept of the sample holder is tested in liquid helium using the experimental setup depicted in Fig. 5.3(a) including an inductively coupled $\lambda/2$-resonator. The measurement results of the transmission through the whole sample holder are summarized in Fig.5.7(a)-(c), showing the absolute value of the forward transmission $|S_{21}(\omega)|$ as a function of the frequency ω.

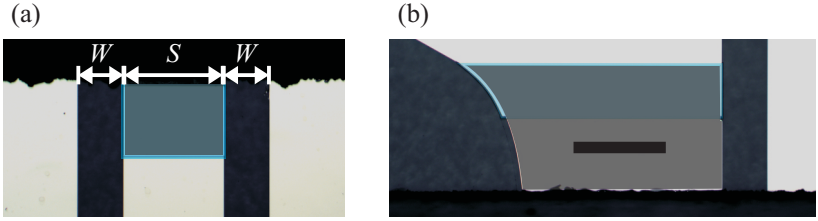

Figure 5.6.: dc-blocks of the integrated bias-T-chip. (a) inside dc-block as part of the bias-T, (b) outside dc-block of one ground plane. Second layer of SiO_2 in (a) and (b) is colored light blue, third layer of niobium is colored dark grey. Black bar in (b) corresponds to 500 μm.

The $\lambda/2$-resonator used for the test of the sample holder has a fundamental frequency of $\omega_{r,1} = 2\pi \cdot 6.83\,\mathrm{GHz}$. However, close to this resonance a lot of parasitic transmission is observed around this frequency (Fig. 5.7(a)), preventing from performing a reliable data analysis[4]. Contrary, for the first and second harmonic distinct transmission peaks can be observed. Best fits to the data are performed using a Lorentzian with asymmetric lineshape introduced by an additional term $Ae^{i\phi}$ [121], i.e.

$$|S_{21}(\omega)| = \left| \frac{a}{1 + 2iQ_{\mathrm{L}}(\omega - \omega_{\mathrm{r}})/\omega_{\mathrm{r}}} + Ae^{i\phi} \right| , \tag{5.1}$$

where A and ϕ are the amplitude and phase of the additional *parasitic wave term*, respectively, a is the *on-resonance* amplitude of the Lorentzian, and ω_{r} and Q_{L} are the resonance frequency and the loaded quality factor of the resonator. The properties of the first and second harmonic are found as $\omega_{r,2} = 2\pi \cdot 13.67\,\mathrm{GHz}$, $Q_{\mathrm{L},2} = 8990$ and $\omega_{r,3} = 2\pi \cdot 20.50\,\mathrm{GHz}$, $Q_{\mathrm{L},3} = 13780$, respectively. Interestingly, the quality factor of the third harmonic overtops its counter part of the second harmonic by roughly a factor of two. Such effects as well as the occurrence of asymmetric transmission peaks can arise as a consequence of the parasitic electromagnetic environment introduced by the complex sample holder. In addition, the choice of finite width ground planes of the resonator supports the coupling to parasitic environments.

[4]Note, that also in other sample holders the fundamental resonance frequency of the exact same sample could not be observed, which might be related to a general problem of the resonator layout (cf. [141]).

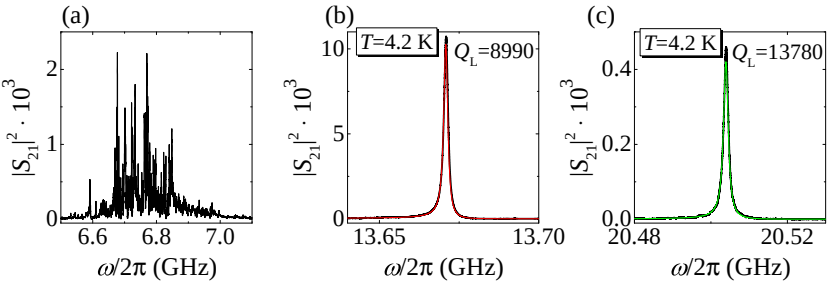

Figure 5.7.: Microwave spectroscopy of the sample holder. (a), (b) and (c) transmission amplitude $|S_{21}(\omega)|$ as a function of the frequency ω close to the fundamental ($\omega_{r,0} \approx 2\pi \cdot 6.83\,\mathrm{GHz}$), first and second harmonic resonance frequency of an inductively coupled $\lambda/2$-resonator.

Briefly summarizing, the sample holder presented throughout this section, including a bias-T-chip and several dc-blocks, in general works and demonstrates that both microwaves and dc-signals can be applied to the sample. The surface of the sample represents the uppermost plane of the sample holder allowing for optical access in order to trap and manipulate atoms in close vicinity to the chip surface. It seems likely that with minor modifications of the bias-T-chips, the maximum superconducting current can be increased by more than a factor of three, as required for the generation of a magnetic trap for ultracold atoms.

6 | Summary and outlook

This work towards the realization of a hybrid quantum system combining superconducting thin film structures and ultracold atomic clouds dealt with the development of superconducting resonators allowing one to interconnect the long-living magnetic ground states of ^{87}Rb atoms to the well understood superconducting coplanar circuitry. Due to the fixed energy spectrum of these ground state atoms in a magnetic trap, concepts had to be developed to change the resonance frequency *in situ*. Particular attention was paid to having concepts for the tuning which are insensitive to magnetic fields applied perpendicular to the chip surface, necessary for trapping the atoms close to the chip. Various concepts of tunable resonators were developed related to two experimental setups available in Tübingen.

First, for experiments taking place at a temperature of about 4.2 K, two concepts were followed. One of them was using the nonlinear dielectric $SrTiO_3$ as a part of an inductively coupled half-wavelength resonator with a lumped nonlinear capacitor. A full model of the circuit was developed enabling the extraction of the complex dielectric function of $SrTiO_3$ and allowing for the use of such nonlinear capacitors in future devices. The tunability of the devices was between $10-50$ MHz, depending on the design of the capacitor. Moreover, these resonators were tunable while still providing relatively large quality factors. The other concept useful for experiments at temperatures $T/T_c > 0.4$ was changing the temperature of the resonator, modifying the kinetic inductance fraction of the overall inductance and allowing for tuning the resonance frequency on the order of 100 MHz. Both of these two concepts were translated into an integrated atom chip design containing a Z-shaped trapping wire and an inductively coupled half-wavelength resonator. Finally, due to the easier experimental realization, the latter of the two concepts was used to study the resonant and non-resonant interaction of an

ultracold cloud of ^{87}Rb atoms and the radiation field of a strongly driven cavity.

Second, one further concept, allowing to change the resonance frequency at arbitrary temperatures (below the superconducting transition temperature), was developed for lumped element resonators. A stacked two-chip approach was realized, consisting of a bottom chip containing a microwave transmission line with finite width ground planes, and a second chip placed on top of the first chip with the lumped element resonator patterned on the top side. A full model for the circuit was developed. The model resulted in a software enabling a fit procedure, allowing the extraction of the internal and external quality factor as well as the resonance frequency. In addition, the circuit parameters, i.e. all circuit capacitances and inductances, were simulated as a function of the position of the resonator with respect to the transmission line. The combination of the model and the simulations was used for predicting the behavior of the device. Excellent agreement with measurements was found, indicating that the physics of the device is captured by the model properly. Motivated by the agreement, the model was used to optimize the geometry regarding maximum coupling to the magnetic ground state of ^{87}Rb atoms. The optimized geometry was found to bring the coupled system of resonator and atoms to the threshold of strong coupling. Moreover, it was shown that a direct current applied to the center conductor of the transmission line can be used to trap the atomic ensemble above the loop of the lumped element resonator. The properties of the lumped element resonators were shown to be about one order of magnitude more stable than for inductively coupled coplanar waveguide resonators and more than two orders of magnitude more stable than for capacitively coupled coplanar waveguide resonators.

In order to get deep into the strong coupling regime, a lumped element resonator was proposed which enables strong coupling to Rydberg states. The lumped device is based on the stacked two-chip approach. Accordingly, tuning the resonance frequency can also be realized by moving the resonator with respect to the transmission line. The main adjustment is implementing a parallel plate capacitor, which can be realized by electroplating of normal conducting and superconducting electrodes. The coupling to Rydberg states was simulated to be of order $> 10\,\mathrm{MHz}$. Using the long-living magnetic ground states of the ^{87}Rb atoms, however, requires the implementation of an additional mapping technique.

The last part of the thesis considered the transfer and implementation of such a hybrid quantum system, well studied at around 4 K, to the mK-setup. In detail, due to the small cooling power at mK-temperatures, particular care was taken regarding the realization of a purely superconducting supply of direct currents for the cold atom trap. A sample holder, capable of providing both dc and ac-supply for an atom chip, was developed. As a central component of the sample holder, integrated bias-T-chips were developed, combining dc-connection via a T-filter design and ac-connection to the center conductor of its transmission line, as well as dc-blocks. The sample holder was tested regarding both its microwave transmission and its critical current for direct currents. The microwave transmission was found to be reasonably large for the characterization of microwave devices at frequencies above 10 GHz, exemplarily tested using an inductively coupled half-wavelength resonator. The critical current of the T-filter was found to be about a factor of 3 too small for real experiments. The design of the T-filter can easily be modified using meandered inductors instead of spiral inductors, thereby omitting the wires to be patterned in different layers (and in particular preventing these wires to have steps) and presumably allowing them to carry currents up to 500 mA.

The results of this thesis represent one further step of the path towards achieving the long-term goal of entangling quantum states of completely different origin. Based on the present work, more complex architectures for the investigation of hybrid quantum systems of superconductors and ultracold atoms can be built. One possible solution is shown in Fig. 6.1. Two capacitively coupled resonators constitute the main part of the envisioned chip architecture. One of them is the proposed lumped element resonator, the other one is a half-wavelength coplanar waveguide resonator. The architecture is based on the two-chip approach and incorporates a transmission line for excitation and readout of the lumped element resonator. A direct current applied to the center conductor of the transmission line then be used for trapping the atoms between the capacitor plates (cf. Fig. 6.1(a)). Furthermore, the multi-layered device contains a superconducting qubit, designed as a serial gradiometric SQUID (superconducting quantum interference device) with one further serial gradiometric SQUID enabling to tune the qubit frequency (cf. Fig. 6.1(b)). The qubit is coupled to the half-wavelength resonator by either designing the top layer (green) as part of the center conductor of the resonator, or using a flip chip approach, i.e. fabricating the qubit on a separate chip.

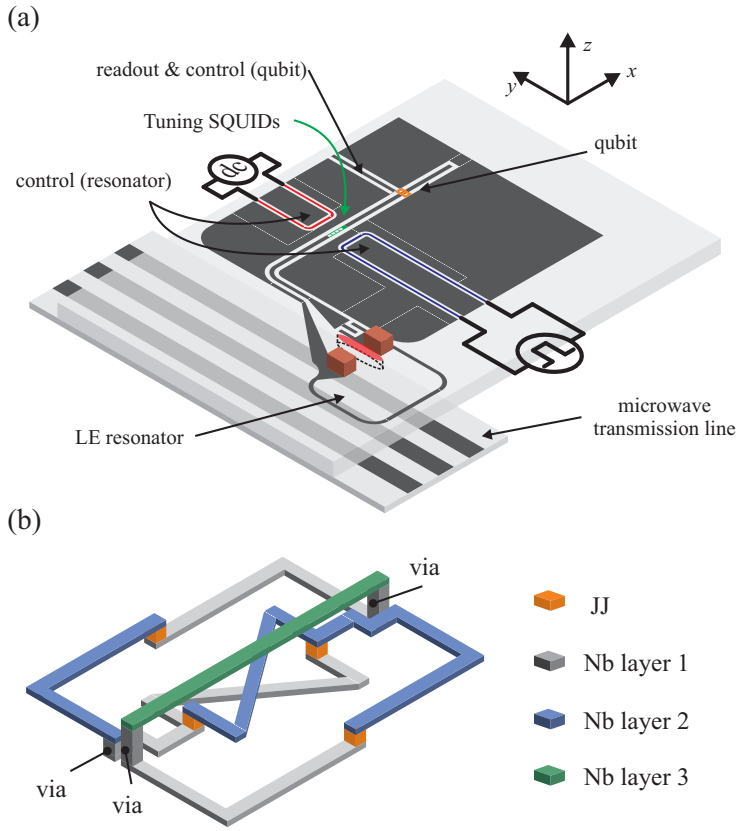

Figure 6.1.: Envisioned architecture for the realization of a hybrid quantum system of superconducting micro-structures and a cloud of ultracold atoms. (a) Overview of the stacked chip architecture, (b) details of a serial gradiometric qubit with a serial gradiometric tuning SQUID (for details see text).

Furthermore, the half-wavelength resonator has to be frequency tunable, provided by an array of tuning SQUIDs. For the exchange of quantum information a protocol similar to the following one can be used for creating entangled states between the superconducting qubit and the cold atom cloud. Assume the excitation to be in the qubit and the half-wavelength resonator

to be off-resonant with both the qubit and the lumped element resonator as the initial state. Then, tuning the half-wavelength resonator into resonance with the qubit for a time corresponding to a $\pi/2$-pulse and afterwards in resonance with the lumped element resonator for a time representing a π-pulse, transfers the quantum information to the lumped element resonator. Finally, a π-pulse between the lumped element resonator and the atom cloud using Rydberg states transmits the information to the cloud, while a mapping to the magnetic ground state saves the quantum information in the cold atom cloud serving as quantum memory.

APPENDICES

A | XRD analysis of a STO thin film on sapphire

Figure A.1 shows the $2\theta - \Omega$ scan of a X-ray diffraction measurement of one $SrTiO_3$ thin film with a thickness of 100 nm deposited on a r-cut sapphire (Al_2O_3) substrate by means of pulsed laser deposition and 15 minutes of annealing at a temperature of about $T = 850\,°C$. The scan shows distinct

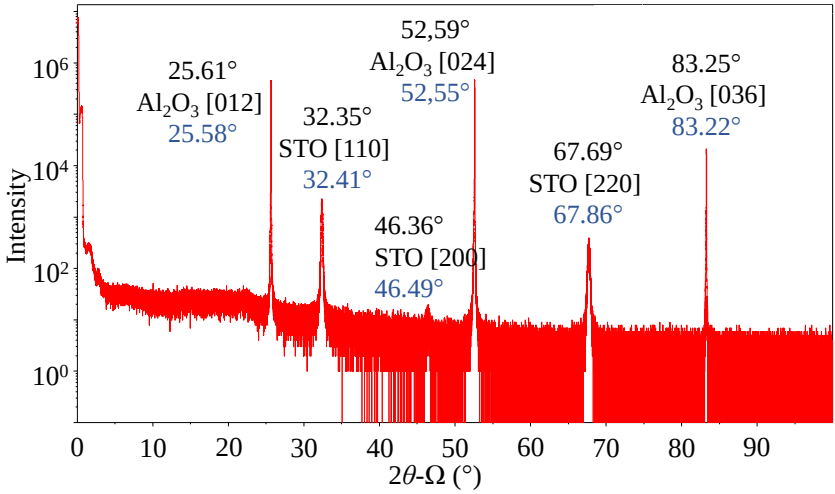

Figure A.1.: XRD data of a STO thin film on sapphire. Labels for each peak denote measured angle, material, Miller indices and literature values for the materials.

peaks. Comparing the angles of the peaks to literature values of both Al_2O_3

and $SrTiO_3$, an identification of these peaks corresponding to these materials is possible. On the one hand, according to the presence of the peaks it seems likely that the $SrTiO_3$ unit cells are partially ordered. On the other hand, some $SrTiO_3$ peaks have a small intensity (cf. the [200] peak at $T = 46.36\,^\circ$). The $SrTiO_3$ films fabricated during the thesis are thus referred to as polycrystalline with preferential order.

B One further tunable resonator with a nonlinear dielectric

In addition to the tunable resonator with a nonlinear dielectric shown in Sec. 3.1, further samples were measured. One further layout of a nonlinear capacitor is shown in Fig. B.1(a). In contrast to the sample analyzed in

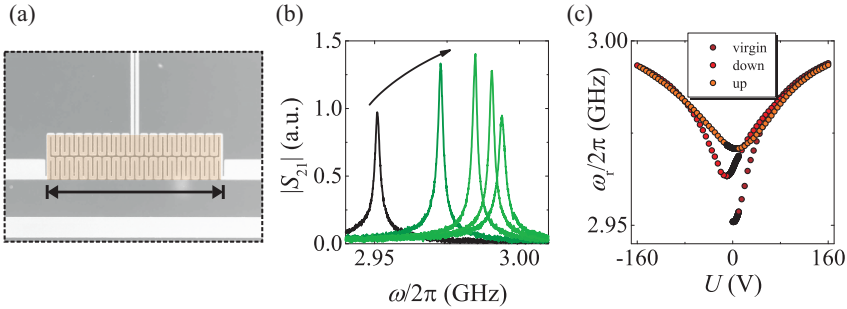

Figure B.1.: Variation of a tunable resonator. (a) Layout of the nonlinear capacitor, (b) transmission amplitude $|S_{21}(\omega)|$ for voltages from $0 - 80\,\mathrm{V}$ in steps of $40\,\mathrm{V}$, (c) hysteresis of the resonance frequency. Arrow in (b) points towards transmission curves for increasing voltage.

detail in Sec. 3.1, the capacitor of this sample has fingers on both sides of the dc bias electrode. The capacitance is thus increased. The sample has a tunability of about 45 MHz (cf. Fig. B.1(b)). The hysteretic behavior of the resonator is shown in Fig. B.1(c).

Bibliography

[1] T. D. Ladd, F. Jelezko, R. Laflamme, Y. Nakamura, C. Monroe, and J. L. O'Brien, "Quantum computers", Nature **464**, 45–53 (2010).

[2] I. Buluta, S. Ashhab, and F. Nori, "Natural and artificial atoms for quantum computation", Rep. Prog. Phys. **74**, 104401 (2011).

[3] M. A. Nielsen and I. L. Chuang, *Quantum comminication and Quantum Information* (Cambridge University Press, 2000).

[4] R. Feynman, *Nature isn't classical, dammit, and if you want to make a simulation of nature, you'd better make it quantum mechanical, and by golly it's a wonderful problem, because it doesn't look so easy.*

[5] V. Giovannetti, S. Lloyd, and L. Maccone, "Quantum-enhanced measurements: beating the standard quantum limit", Science **306**, 1330–1336 (2004).

[6] F. Jelezko, T. Gaebel, I. Popa, A. Gruber, and J. Wrachtrup, "Observation of coherent oscillations in a single electron spin", Phys. Rev. Lett. **92**, 076401 (2004).

[7] R. Hanson, L. P. Kouwenhoven, J. R. Petta, S. Tarucha, and L. M. K. Vandersypen, "Spins in few-electron quantum dots", Rev. Mod. Phys. **79**, 1217–1265 (2007).

[8] J. Clarke and F. K. Wilhelm, "Superconducting quantum bits", Nature **453**, 1031–1042 (2008).

[9] D. P. DiVincenzo, "The physical implementation of quantum computation", Fortschr. Phys. **48**, 771–783 (2000).

[10] C. Guerlin, J. Bernu, S. Deleglise, C. Sayrin, S. Gleyzes, S. Kuhr, M. Brune, J.-M. Raimond, and S. Haroche, "Progressive field-state collapse and quantum non-demolition photon counting", Nature **448**, 889–893 (2007).

[11] D. B. Hume, T. Rosenband, and D. J. Wineland, "High-fidelity adaptive qubit detection through repetitive quantum nondemolition measurements", Phys. Rev. Lett. **99**, 120502 (2007).

[12] A. Wallraff, D. I. Schuster, A. Blais, L. Frunzio, R.-S. Huang, J. Majer, S. Kumar, S. M. Girvin, and R. J. Schoelkopf, "Strong coupling of a single photon to a superconducting qubit using circuit quantum electrodynamics", Nature **431**, 162–167 (2004).

[13] T. Niemczyk, F. Deppe, H. Huebl, E. P. Menzel, F. Hocke, M. J. Schwarz, J. J. Garcia-Ripoll, D. Zueco, T. Hümmer, E. Solano, A. Marx, and R. Gross, "Circuit quantum electrodynamics in the ultrastrong-coupling regime", Nat. Phys. **6**, 772–776 (2010).

[14] A. Blais, R.-S. Huang, A. Wallraff, S. M. Girvin, and R. J. Schoelkopf, "Cavity quantum electrodynamics for superconducting electrical circuits: An architecture for quantum computation", Phys. Rev. A **69**, 062320 (2004).

[15] L. DiCarlo, J. M. Chow, J. M. Gambetta, L. S. Bishop, B. R. Johnson, D. I. Schuster, J. Majer, A. Blais, L. Frunzio, S. M. Girvin, and R. J. Schoelkopf, "Demonstration of two-qubit algorithms with a superconducting quantum processor", Nature **460**, 240–244 (2009).

[16] R. Barends, J. Kelly, A. Megrant, A. Veitia, D. Sank, E. Jeffrey, T. C. White, J. Mutus, A. G. Fowler, B. Campbell, Y. Chen, Z. Chen, B. Chiaro, A. Dunsworth, C. Neill, P. O'Malley, P. Roushan, A. Vainsencher, J. Wenner, A. N. Korotkov, A. N. Cleland, and J. M. Martinis, "Superconducting quantum circuits at the surface code threshold for fault tolerance", Nature **508**, 500–503 (2014).

[17] A. G. Fowler, M. Mariantoni, J. M. Martinis, and A. N. Cleland, "Surface codes: Towards practical large-scale quantum computation", Phys. Rev. A **86**, 032324 (2012).

[18] J. Kelly, R. Barends, A. G. Fowler, A. Megrant, E. Jeffrey, T. C. White, D. Sank, J. Y. Mutus, B. Campbell, Y. Chen, Z. Chen, B. Chiaro, A. Dunsworth, I.-C. Hoi, C. Neill, P. J. J. O'Malley, C. Quintana, P. Roushan, A. Vainsencher, J. Wenner, A. Cleland, and J. M. Martinis, "State preservation by repetitive error detection in a superconducting quantum circuit", Nature **519**, 66–69 (2015).

[19] A. André, D. DeMille, J. M Doyle, M. D. Lukin, S. E. Maxwell, P. Rabl, R. J. Schoelkopf, and P. Zoller, "A coherent all-electrical interface between polar molecules and mesoscopic superconducting resonators", Nat. Phys. **2**, 636–642 (2006).

[20] P. Rabl, D. DeMille, J. M. Doyle, M. D. Lukin, R. J. Schoelkopf, and P. Zoller, "Hybrid quantum processors: molecular ensembles as quantum memory for solid state circuits", Phys. Rev. Lett. **97**, 033003 (2006).

[21] J. Verdú, H. Zoubi, C. Koller, J. Majer, H. Ritsch, and J. Schmiedmayer, "Strong magnetic coupling of an ultracold gas to a superconducting waveguide cavity", Phys. Rev. Lett. **103**, 043603 (2009).

[22] A. Imamoğlu, "Cavity QED based on collective magnetic dipole coupling: spin ensembles as hybrid two-level systems", Phys. Rev. Lett. **102**, 083602 (2009).

[23] D. I. Schuster, A. P. Sears, E. Ginossar, L. DiCarlo, L. Frunzio, J. J. L. Morton, H. Wu, G. A. D. Briggs, B. B. Buckley, D. D. Awschalom, and R. J. Schoelkopf, "High-cooperativity coupling of electron-spin ensembles to superconducting cavities", Phys. Rev. Lett. **105**, 140501 (2010).

[24] Y. Kubo, F. R. Ong, P. Bertet, D. Vion, V. Jacques, D. Zheng, A. Dréau, J.-F. Roch, A. Auffeves, F. Jelezko, J. Wrachtrup, M. F. Barthe, P. Bergonzo, and D. Esteve, "Strong coupling of a spin ensemble to a superconducting resonator", Phys. Rev. Lett. **105**, 140502 (2010).

[25] H. Wu, R. E. George, J. H. Wesenberg, K. Mølmer, D. I. Schuster, R. J. Schoelkopf, K. M. Itoh, A. Ardavan, J. J. L. Morton, and G. A. D. Briggs, "Storage of multiple coherent microwave excitations in an electron spin ensemble", Phys. Rev. Lett. **105**, 140503 (2010).

[26] R. Amsüss, C. Koller, T. Nöbauer, S. Putz, S. Rotter, K. Sandner, S. Schneider, M. Schramböck, G. Steinhauser, H. Ritsch, J. Schmiedmayer, and J. Majer, "Cavity QED with magnetically coupled collective spin states", Phys. Rev. Lett. **107**, 060502 (2011).

[27] Y. Kubo, C. Grezes, A. Dewes, T. Umeda, J. Isoya, H. Sumiya, N. Morishita, H. Abe, S. Onoda, T. Ohshima, V. Jacques, A. Dréau, J.-F. Roch, I. Diniz, A. Auffeves, D. Vion, D. Esteve, and P. Bertet, "Hybrid quantum circuit with a superconducting qubit coupled to a spin ensemble", Phys. Rev. Lett. **107**, 220501 (2011).

[28] S. Probst, H. Rotzinger, S. Wünsch, P. Jung, M. Jerger, M. Siegel, A. V. Ustinov, and P. A. Bushev, "Anisotropic rare-earth spin ensemble strongly coupled to a superconducting resonator", Phys. Rev. Lett. **110**, 157001 (2013).

[29] C. W. Zollitsch, K. Mueller, D. P. Franke, S. T. B. Goennenwein, M. S. Brandt, R. Gross, and H. Huebl, "High cooperativity coupling between a phosphorus donor spin ensemble and a superconducting microwave resonator", Appl. Phys. Lett. **107**, 142105 (2015).

[30] K. Henschel, J. Majer, J. Schmiedmayer, and H. Ritsch, "Cavity QED with an ultracold ensemble on a chip: Prospects for strong magnetic coupling at finite temperatures", Phys. Rev. A **82**, 033810 (2010).

[31] Z.-L. Xiang, S. Ashhab, J. Q. You, and F. Nori, "Hybrid quantum circuits: superconducting circuits interacting with other quantum systems", Rev. Mod. Phys. **85**, 623–653 (2013).

[32] C. Deutsch, F. Ramirez-Martinez, C. Lacroûte, F. Reinhard, T. Schneider, J. N. Fuchs, F. Piéchon, F. Laloë, J. Reichel, and P. Rosenbusch, "Spin self-rephasing and very long coherence times in a trapped atomic ensemble", Phys. Rev. Lett. **105**, 020401 (2010).

[33] D. Petrosyan and M. Fleischhauer, "Quantum information processing with single photons and atomic ensembles in microwave coplanar waveguide resonators", Phys. Rev. Lett. **100**, 170501 (2008).

[34] D. Petrosyan, G. Bensky, G. Kurizki, I. Mazets, J. Majer, and J. Schmiedmayer, "Reversible state transfer between superconducting qubits and atomic ensembles", Phys. Rev. A **79**, 040304 (2009).

[35] J. D. Pritchard, J. A. Isaacs, M. A. Beck, R. McDermott, and M. Saffman, "Hybrid atom-photon quantum gate in a superconducting microwave resonator", Phys. Rev. A **89**, 010301 (2014).

[36] L. Sárkány, J. Fortágh, and D. Petrosyan, "Long-range quantum gate via Rydberg states of atoms in a thermal microwave cavity", Phys. Rev. A **92**, 030303 (2015).

[37] D. Yu, L. C. Kwek, L. Amico, and R. Dumke, "Theoretical description of a micromaser in the ultrastrong-coupling regime", Phys. Rev. A **95**, 053811 (2017).

[38] D. Cano, B. Kasch, H. Hattermann, R. Kleiner, C. Zimmermann, D. Koelle, and J. Fortágh, "Meissner Effect in Superconducting Microtraps", Phys. Rev. Lett. **101**, 183006 (2008).

[39] D. Cano, B. Kasch, H. Hattermann, D. Koelle, R. Kleiner, C. Zimmermann, and J. Fortágh, "Impact of the Meissner effect on magnetic microtraps for neutral atoms near superconducting thin films", Phys. Rev. A **77**, 063408 (2008).

[40] P. Weiss, M. Knufinke, S. Bernon, D. Bothner, L. Sárkány, C. Zimmermann, R. Kleiner, D. Koelle, J. Fortágh, and H. Hattermann, "Sensitivity of ultracold atoms to quantized flux in a superconducting ring", Phys. Rev. Lett. **114**, 113003 (2015).

[41] K. R. Patton and U. R. Fischer, "Hybrid of superconducting quantum interference device and atomic Bose-Einstein condensate: An architecture for quantum information processing", Phys. Rev. A **87**, 052303 (2013).

[42] K. R. Patton and U. R. Fischer, "Ultrafast quantum random access memory utilizing single rydberg atoms in a Bose-Einstein condensate", Phys. Rev. Lett. **111**, 240504 (2013).

[43] K. R. Patton and U. R. Fischer, "Transfer and storage of qubits in the presence of decoherence", Europhys. Lett. **102**, 20001 (2013).

[44] S. Bernon, H. Hattermann, D. Bothner, M. Knufinke, P. Weiss, F. Jessen, D. Cano, M. Kemmler, R. Kleiner, D. Koelle, and J. Fortágh, "Manipulation and coherence of ultra-cold atoms on a superconducting atom chip", Nat. Commun. **4**, 2380 (2013).

[45] H. Hattermann, D. Bothner, L. Y. Ley, B. Ferdinand, D. Wiedmaier, L. Sárkány, R. Kleiner, D. Koelle, and J. Fortágh, "Coupling ultracold atoms to a superconducting coplanar waveguide resonator", Nat. Commun. **8**, 2254 (2017).

[46] F. Jessen, M. Knufinke, S. C. Bell, P. Vergien, H. Hattermann, P. Weiss, M. Rudolph, M. Reinschmidt, K. Meyer, T. Gaber, D. Cano, A. Günther, S. Bernon, D. Koelle, R. Kleiner, and J. Fortágh, "Trapping of ultracold atoms in a ^{3}He/^{4}He dilution refrigerator", Appl. Phys. B **116**, 665–671 (2014).

[47] M. Knufinke, "Aufbau und Entwicklung von Experimenten an Supraleiter-Atom-Hybridsystemen", PhD thesis (Eberhard Karls Universität Tübingen, 2013).

[48] J. Fortágh and C. Zimmermann, "Magnetic microtraps for ultracold atoms", Rev. Mod. Phys. **79**, 235–289 (2007).

[49] D. Bothner, "Micropatterned superconducting film circuitry for operation in hybrid quantum devices", PhD thesis (Eberhard Karls Universität Tübingen, 2013).

[50] D. Bothner, T. Gaber, M. Kemmler, D. Koelle, R. Kleiner, S. Wünsch, and M. Siegel, "Magnetic hysteresis effects in superconducting coplanar microwave resonators", Phys. Rev. B **86**, 014517 (2012).

[51] D. Bothner, T. Gaber, M. Kemmler, D. Koelle, and R. Kleiner, "Improving the performance of superconducting microwave resonators in magnetic fields", Appl. Phys. Lett. **98**, 102504 (2011).

[52] D. Bothner, D. Wiedmaier, B. Ferdinand, R. Kleiner, and D. Koelle, "Improving superconducting resonators in magnetic fields by reduced field-focussing and engineered flux screening", Phys. Rev. Applied **8**, 034025 (2017).

[53] D. Bothner, M. Knufinke, H. Hattermann, R. Wölbing, B. Ferdinand, P. Weiss, S. Bernon, J. Fortágh, D. Koelle, and R. Kleiner, "Inductively coupled superconducting half wavelength resonators as persistent current traps for ultracold atoms", New J. Phys. **15**, 093024 (2013).

[54] D. M. Pozar, *Microwave engineering* (John Wiley & Sons, Inc., 1998).

[55] C. P. Wen, "Coplanar waveguide: a surface strip transmission line suitable for nonreciprocal gyromagnetic device applications", IEEE Trans. Microw. Theory **17**, 1087–1090 (1969).

[56] R. N. Simons, *Coplanar waveguide circuits, components, and systems* (Wiley-Interscience, 2001).

[57] K. Gupta, R. Garg, I. Bahl, and P. Bhartia, *Microstrip lines and slotlines, second edition* (Artech House, 1996).

[58] L. Thévenin, "Extension de la loi d'ohm aux circuits électromoteurs complexes [extension of ohm's law to complex electromotive circuits]", Annales Télégraphiques **10**, 222–224 (1883).

[59] L. Thévenin, "Sur un nouveau théoreme d'électricité dynamique [on a new theorem of dynamic electricity]", CR des Séances de l'Académie des Sciences **97**, 159–161 (1883).

[60] D. Wiedmaier, "Entwicklung supraleitender Mikrowellenresonatoren zur Anwendung in hybriden Quantensystemen", MA thesis (Eberhard Karls Universität Tübingen, 2014).

[61] H. K. Onnes, "The resistance of pure mercury at helium temperatures", Commun. Phys. Lab. Univ. Leiden **12**, 120 (1911).

[62] W. Meissner and R. Ochsenfeld, "Ein neuer Effekt bei Eintritt der Supraleitfähigkeit", Naturwissenschaften **21**, 787–788 (1933).

[63] F. London and H. London, "The electromagnetic equations of the supraconductor", Proceedings of the Royal Society of London **149**, 71–88 (1935).

[64] L. V. Shubnikov, V. I. Khotkevich, D. Shepelev Yu, and N. Riabinin Yu, "Magnetic properties of superconducting metals and alloys", Zh. Eksp. Teor. Fiz **7**, 221–237 (1937).

[65] N. Zavaritskii, "Superconducting properties of thallium and tin films condensed at low temperatures", Doklady Akad. Nauk. SSSR **86**, 501–504 (1952).

[66] A. A. Abrikosov, "On the magnetic properties of superconductors of the second group", Sov. Phys.-JETP **5**, 1174–1182 (1957).

[67] V. L. Ginzburg and L. D. Landau, "On the theory of superconductivity", Zh. Eksp. Teor. Fiz **20**, 1064 (1950).

[68] M. M. Khapaev, M. Y. Kupriyanov, E. Goldobin, and M. Siegel, "Current distribution simulation for superconducting multi-layered structures", Supercond. Sci. Technol. **16**, 24–27 (2002).

[69] R. Gross and A. Marx, *Festkörperphysik* (Walter de Gruyter GmbH & Co KG, 2014).

[70] R. Meservey and P. M. Tedrow, "Measurements of the kinetic inductance of superconducting linear structures", J. Appl. Phys. **40**, 2028–2034 (1969).

[71] P. K. Day, H. G. LeDuc, B. A. Mazin, A. Vayonakis, and J. Zmuidzinas, "A broadband superconducting detector suitable for use in large arrays", Nature **425**, 817–821 (2003).

[72] J. Zmuidzinas, "Superconducting microresonators: physics and applications", Annu. Rev. Condens. Matter Phys. **3**, 169–214 (2012).

[73] H. Unoki and T. Sakudo, "Electron spin resonance of Fe_3^+ in $SrTiO_3$ with special reference to the 110 K phase transition", J. Phys. Soc. Jpn **23**, 546–552 (1967).

[74] G. Shirane and Y. Yamada, "Lattice-dynamical study of the 110 K phase transition in $SrTiO_3$", Phys. Rev. **177**, 858–863 (1969).

[75] J. Feder and E. Pytte, "Theory of a structural phase transition in perovskite-type crystals. II. Interaction with elastic strain", Phys. Rev. B **1**, 4803–4810 (1970).

[76] J. Sidoruk, J. Leist, H. Gibhardt, M. Meven, K. Hradil, and G. Eckold, "Quantitative determination of domain distribution in $SrTiO_3$ - competing effects of applied electric field and mechanical stress", J. Phys. Condens. Matter **22**, 235903 (2010).

[77] J. Hemberger, M. Nicklas, R. Viana, P. Lunkenheimer, A. Loidl, and R. Böhmer, "Quantum paraelectric and induced ferroelectric states in $SrTiO_3$", Journal of Physics: Condensed Matter **8**, 4673–4690 (1996).

[78] E. Hegenbarth, "Die Feldstärkeabhängigkeit der Dielektrizitätskonstanten von $SrTiO_3$-Einkristallen im Temperaturbereich von 15 bis 80° K", Phys. Status Solidi **6**, 333–337 (1964).

[79] R. C. Neville, B. Hoeneisen, and C. A. Mead, "Permittivity of strontium titanate", J. Appl. Phys. **43**, 2124–2131 (1972).

[80] K. A. Müller and H. Burkard, "$SrTiO_3$: an intrinsic quantum paraelectric below 4 K", Phys. Rev. B **19**, 3593–3602 (1979).

[81] J. Hemberger, P. Lunkenheimer, R. Viana, R. Böhmer, and A. Loidl, "Electric-field-dependent dielectric constant and nonlinear susceptibility in $SrTiO_3$", Phys. Rev. B **52**, 13159–13162 (1995).

[82] W. Kleemann, J. Dec, and B. Westwański, "Susceptibility scaling behavior of quantum paraelectric $SrTiO_3$:Ca", Phys. Rev. B **58**, 8985–8990 (1998).

[83] A. F. Devonshire, "XCVI. Theory of barium titanate: Part I", The London, Edinburgh, and Dublin Philosophical Magazine and Journal of Science **40**, 1040–1063 (1949).

[84] J. C. Slater, "The Lorentz correction in barium titanate", Phys. Rev. **78**, 748–761 (1950).

[85] A. F. Devonshire, "Theory of ferroelectrics", Adv. Phys. **3**, 85–130 (1954).

[86] J. H. Barrett, "Dielectric constant in perovskite type crystals", Phys. Rev. **86**, 118–120 (1952).

[87] C. Ang and Z. Yu, "Dc electric-field dependence of the dielectric constant in polar dielectrics: Multipolarization mechanism model", Phys. Rev. B **69**, 174109 (2004).

[88] W. Cochran, "Crystal stability and the theory of ferroelectricity", Adv. Phys. **9**, 387–423 (1960).

[89] R. A. Cowley, "On the theory of ferroelectricity and anharmonic effects in crystals", Philosophical Magazine **11**, 673–706 (1965).

[90] W. G. Stirling, "Neutron inelastic scattering study of the lattice dynamics of strontium titanate: harmonic models", J. Phys. C **5**, 2711–2730 (1972).

[91] R. Migoni, H. Bilz, and D. Bäuerle, "Origin of raman scattering and ferroelectricity in oxidic perovskites", Phys. Rev. Lett. **37**, 1155–1158 (1976).

[92] H. Bilz, A. Bussmann, G. Benedek, H. Buttner, and D. Strauch, "Microscopic model of ferroelectric soft modes", Ferroelectrics **25**, 339–342 (1980).

[93] A. Bussmann, H. Bilz, R. Roenspiess, and K. Schwarz, "Oxygen polarizability in ferroelectric phase transitions", Ferroelectrics **25**, 343–346 (1980).

[94] H. Bilz, G. Benedek, and A. Bussmann-Holder, "Theory of ferroelectricity: The polarizability model", Phys. Rev. B **35**, 4840–4849 (1987).

[95] G. Benedek, A. Bussmann-Holder, and H. Bilz, "Nonlinear travelling waves in ferroelectrics", Phys. Rev. B **36**, 630–638 (1987).

[96] A. Bussmann-Holder, H. Bilz, and G. Benedek, "Applications of the polarizability model to various displacive-type ferroelectric systems", Phys. Rev. B **39**, 9214–9223 (1989).

[97] A. Bussmann-Holder, "The polarizability model for ferroelectricity in perovskite oxides", J. Phys. Condens. Matter. **24**, 273202 (2012).

[98] M. E. Lines and A. M. Glass, *Principles and applications of ferroelectrics and related materials* (Oxford university press, 1977).

[99] A. K. Tagantsev, "Effect of a weak electric field on the dielectric losses in centrosymmetric ferroelectrics of the displacement type", Zh. Eksp. Teor. Fiz **83**, 948–955 (1974).

[100] V. L. Gurevich and A. K. Tagantsev, "Intrinsic dielectric loss in crystals", Adv. Phys. **40**, 719–767 (1991).

[101] S. S. Gevorgian, D. I. Kaparkov, and O. G. Vendik, "Electrically controlled HTSC/ferroelectric coplanar waveguide", IEE P.-Microw. Anten. P. **141**, 501–503 (1994).

[102] O. G. Vendik and S. P. Zubko, "Modeling the dielectric response of incipient ferroelectrics", J. Appl. Phys. **82**, 4475–4483 (1997).

[103] O. G. Vendik, L. T. Ter-Martirosyan, and S. P. Zubko, "Microwave losses in incipient ferroelectrics as functions of the temperature and the biasing field", J. Appl. Phys. **84**, 993–998 (1998).

[104] M. J. Lancaster, J. Powell, and A. Porch, "Thin-film ferroelectric microwave devices", Supercond. Sci. Technol. **11**, 1323–1334 (1998).

[105] D. Damjanovic, "Ferroelectric, dielectric and piezoelectric properties of ferroelectric thin films and ceramics", Rep. Prog. Phys **61**, 1267–1324 (1998).

[106] A. Tagantsev, "Dc-electric-field-induced microwave loss in ferroelectrics and intrinsic limitation for the quality factor of a tunable component", Appl. Phys. Lett. **76**, 1182–1184 (2000).

[107] O. G. Vendik and S. P. Zubko, "Ferroelectric phase transition and maximum dielectric permittivity of displacement type ferroelectrics ($Ba_xSr_{1-x}TiO_3$)", J. Appl. Phys. **88**, 5343–5350 (2000).

[108] O. Vendik, S. Zubko, and M. Nikol'ski, "Microwave loss-factor of $Ba_xSr_{1-x}TiO_3$ as a function of temperature, biasing field, barium concentration, and frequency", J. Appl. Phys. **92**, 7448–7452 (2002).

[109] A. K. Tagantsev, V. O. Sherman, K. F. Astafiev, J. Venkatesh, and N. Setter, "Ferroelectric materials for microwave tunable applications", J. Electroceramics **11**, 5–66 (2003).

[110] H.-C. Li, W. Si, A. D West, and X. Xi, "Near single crystal-level dielectric loss and nonlinearity in pulsed laser deposited $SrTiO_3$ thin films", Appl. Phys. Lett. **73**, 190–192 (1998).

[111] K. Bouzehouane, P. Woodall, B. Marcilhac, A. N. Khodan, D. Crété, E. Jacquet, J. C. Mage, and J. P. Contour, "Enhanced dielectric properties of $SrTiO_3$ epitaxial thin film for tunable microwave devices", Appl. Phys. Lett. **80**, 109–111 (2002).

[112] D. Davidovikj, N. Manca, H. S. J. van der Zant, A. D. Caviglia, and G. A. Steele, "Quantum paraelectricity probed by superconducting resonators", Phys. Rev. B **95**, 214513 (2017).

[113] S. P. Zubko and A. N. Vasil'ev, "A model for the dependence of the dielectric loss factor of a ferroelectric on the microwave signal amplitude", Phys. Solid State **51**, 1545–1547 (2009).

[114] D. E. Grupp and A. M. Goldman, "Giant Piezoelectric Effect in Strontium Titanate at Cryogenic Temperatures", Science **276**, 392–394 (1997).

[115] B. Ferdinand, "Entwicklung von koplanaren Resonatoren aus Nb-Filmen zur Kopplung mit ultrakalten atomaren Gasen", Diploma thesis, (Eberhard Karls Universität Tübingen, 2013).

[116] J. Wenner, M. Neeley, R. C. Bialczak, M. Lenander, E. Lucero, A. D. O'Connell, D. Sank, H. Wang, M. Weides, A. N. Cleland, and J. M. Martinis, "Wirebond crosstalk and cavity modes in large chip mounts for superconducting qubits", Supercond. Sci. Technol. **24**, 065001 (2011).

[117] B. W. Langley, S. M. Anlage, R. F. W. Pease, and M. R. Beasley, "Magnetic penetration depth measurements of superconducting thin films by a microstrip resonator technique", Rev. Sci. Instrum. **62**, 1801–1812 (1991).

[118] W. Rauch, E. Gornik, G. Sölkner, A. A. Valenzuela, F. Fox, and H. Behner, "Microwave properties of $YBa_2Cu_3O_{7-x}$ thin films studied with coplanar transmission line resonators", J. Appl. Phys. **73**, 1866–1872 (1993).

[119] K. Watanabe, K. Yoshida, T. Aoki, and S. Kohjiro, "Kinetic inductance of superconducting coplanar waveguides", Jpn. J. Appl. Phys. **33**, 5708–5712 (1994).

[120] J. R Clem, "Inductances and attenuation constant for a thin-film superconducting coplanar waveguide resonator", J. Appl. Phys. **113**, 013910 (2013).

[121] J. M. Hornibrook, E. E. Mitchell, C. J. Lewis, and D. J. Reilly, "Parasitic losses in Nb superconducting resonators", Physics Procedia **36**, 187–192 (2012).

[122] N. Samkharadze, A. Bruno, P. Scarlino, G. Zheng, D. P. DiVincenzo, L. DiCarlo, and L. M. K. Vandersypen, "High-kinetic-inductance superconducting nanowire resonators for circuit QED in a magnetic field", Phys. Rev. Applied **5**, 044004 (2016).

[123] A. Bienfait, J. J. Pla, Y. Kubo, X. Zhou, M. Stern, C. C. Lo, C. D. Weis, T. Schenkel, D. Vion, D. Esteve, J. J. M. Morton, and P. Bertet, "Controlling spin relaxation with a cavity", Nature **531**, 74–77 (2016).

[124] B. Sarabi, P. Huang, and N. M. Zimmerman, "Prospective two orders of magnitude enhancement in direct magnetic coupling of a single-atom spin to a circuit resonator", arXiv:1702.02210 (2017).

[125] A. Stockklauser, P. Scarlino, J. V. Koski, S. Gasparinetti, C. K. Andersen, C. Reichl, W. Wegscheider, T. Ihn, K. Ensslin, and A. Wallraff, "Strong coupling cavity QED with gate-defined double quantum dots enabled by a high impedance resonator", Phys. Rev. X **7**, 011030 (2017).

[126] S. J. Bosman, M. F. Gely, V. Singh, D. Bothner, A. Castellanos-Gomez, and G. A. Steele, "Approaching ultra-strong coupling in Transmon circuit-QED using a high-impedance resonator", Phys. Rev. B **95**, 224515 (2017).

[127] F. Glang, "Lumped-Element-Resonatoren aus supraleitenden Nb-Dünnfilmen in äußeren Magnetfeldern", Bachelor thesis (Eberhard Karls Universität Tübingen, 2017).

[128] A. Palacios-Laloy, F. Nguyen, F. Mallet, P. Bertet, D. Vion, and D. Esteve, "Tunable resonators for quantum circuits", J. Low Temp. Phys. **151**, 1034–1042 (2008).

[129] M. Sandberg, C. M. Wilson, F. Persson, T. Bauch, G. Johansson, V. Shumeiko, T. Duty, and P. Delsing, "Tuning the field in a microwave resonator faster than the photon lifetime", Appl. Phys. Lett. **92**, 203501 (2008).

[130] Z. L. Wang, Y. P. Zhong, L. J. He, H. Wang, J. M. Martinis, A. N. Cleland, and Q. W. Xie, "Quantum state characterization of a fast tunable superconducting resonator", Appl. Phys. Lett. **102**, 163503 (2013).

[131] C. Deng, M. Otto, and A. Lupascu, "An analysis method for transmission measurements of superconducting resonators with applications to quantum-regime dielectric-loss measurements", J. Appl. Phys. **114**, 054504 (2013).

[132] J. Wenner, Y. Yin, Y. Chen, R. Barends, B. Chiaro, E. Jeffrey, J. Kelly, A. Megrant, J. Y. Mutus, C. Neill, P. J. J. O'Malley, P. Roushan, D. Sank, A. Vainsencher, T. C. White, A. N. Korotkov, A. N. Cleland, and J. M. Martinis, "Catching time-reversed microwave coherent state photons with 99.4% absorption efficiency", Phys. Rev. Lett. **112**, 210501 (2014).

[133] C. Koller, "Towards the experimental realization of Hybrid Quantum Systems", PhD thesis (TU-Wien, 2012).

[134] K. Geerlings, S. Shankar, E. Edwards, L. Frunzio, R. J. Schoelkopf, and M. H. Devoret, "Improving the quality factor of microwave compact resonators by optimizing their geometrical parameters", Appl. Phys. Lett. **100**, 192601 (2012).

[135] A. Megrant, C. Neill, R. Barends, B. Chiaro, Y. Chen, L. Feigl, J. Kelly, E. Lucero, M. Mariantoni, P. J. J. O'Malley, C. Quintana, P. Roushan, A. Vainsencher, J. Wenner, A. N. Cleland, and J. M. Martinis, "Planar superconducting resonators with internal quality factors above one million", Appl. Phys. Lett. **100**, 113510 (2012).

[136] D. A. Steck, "Rubidium 87 d line data", available online at http://steck.us/alkalidata (revision 2.1.4,23 December 2010).

[137] J. E. Healey, T. Lindström, M. S. Colclough, C. M. Muirhead, and A. Y. Tzalenchuk, "Magnetic field tuning of coplanar waveguide resonators", Appl. Phys. Lett. **93**, 043513 (2008).

[138] M. Saffman, T. G. Walker, and K. Mølmer, "Quantum information with rydberg atoms", Rev. Mod. Phys. **82**, 2313–2363 (2010).

[139] M. A. Beck, J. A. Isaacs, D. Booth, J. D. Pritchard, M. Saffman, and R. McDermott, "Optimized coplanar waveguide resonators for a superconductor-atom interface", Appl. Phys. Lett. **109**, 092602 (2016).

[140] W. J. Skocpol, M. R. Beasley, and M. Tinkham, "Self-heating hotspots in superconducting thin-film microbridges", Journal of Applied Physics **45**, 4054–4066 (1974).

[141] C. Klatt, "Supraleitende Nb-Mikrowellen-Resonatoren", MA thesis (Eberhard Karls Universität Tübingen, 2015).

List of Figures